UNIVERSITÀ DEGLI STUDI DI TRIESTE

XVI CICLO DEL
DOTTORATO DI RICERCA IN
FISICA

Atomic scale investigations of model catalysts for oxidation reactions

DOTTORANDA

DOTT. CRISTINA AFRICH 173

CS

COORDINATORE DEL COLLEGIO DEI DOCENTI

CHIAR.MO PROF. GAETANO SENATORE,
UNIVERSITÀ DEGLI STUDI DI TRIESTE

DOTTORATO DI RICERCA
DI FISICA
UNIVERSITÀ DI TRIESTE
Il Coordinatore

TUTORE/RELATORE

CHIAR.MO PROF. GIOVANNI COMELLI,
UNIVERSITÀ DEGLI STUDI DI TRIESTE

CORRELATORE

DR. FRIEDRICH ESCH,
LABORATORIO TASC-INFM

Contents

Chapter 5: An example of Supported Metal Catalyst: Nucleation and Growth of Au Nanoclusters on $TiO_2(110)$

Chapter 6: The Fast STM project: 1000 Times Faster

Introduction

The aim of this PhD thesis work is to study mechanistic details of catalytic processes by exploitation of the capabilities of Scanning Tunneling Microscopy (STM).
This technique, in fact, is a unique tool for imaging surfaces on various length scales, down to the atomic level, and offers the possibility of studying both structural features and dynamical processes.

The term "catalysis" describes the acceleration of chemical reactions due to the presence of a "catalyst", a material which is not consumed during the reaction. If this material is a surface and if the reactants and reaction products are in gas or in liquid phase, one speaks of "heterogeneous catalysis". This is our field of interest.
Heterogeneous catalysis plays a role in many practical applications. A major application is the prevention of pollution: car exhausts, power plants and industrial installations introduce noxious gases in the atmosphere, which can be removed by means of catalysts. But catalysts are also employed, for example, for producing fuels, from gasoline for traditional motors up to hydrogen in fuel cells. They are used in petrochemical as well as in food industry, in the latter case, for example, for the production of margarine. Protective coatings are fabricated against corrosion and environmental damages (for example for marbles). Catalysts are then applied against soil contamination and for manufacturing fertilisers. As a final example, they are employed also for disinfecting, e.g. in operating rooms in hospitals.
A detailed understanding of the underlying mechanisms in simple catalytic processes can help to discuss the behaviour and to improve the quality of real catalysts.
To this purpose simplified model catalysts, instead of real catalysts, are studied. Real catalysts, in fact, are very complicated systems, mainly powders, often composed of metal particles supported or encapsulated by oxide overlayers or suspended in colloidal solutions. In surface science studies of model catalysts, UHV technology is often used in order to control the chemical environment, overcoming contamination problems, and several real processes, which occur at high temperature, are faced by studying the detailed mechanism of their intermediate steps at lower temperatures.

In this thesis three different examples of model catalysts for oxidation reactions have been considered.
The three systems and the order in which they are presented have been selected as a sequence from very simplified models to more realistic cases. It will be shown how the information gained by STM is stunningly detailed.

The first example is the unreconstructed (110) surface of rhodium. The simplest way to face catalytic processes on transition metals is, in fact, the study of oriented surfaces of a single crystal.
Rhodium is one of the most important metals in catalysis, especially as a component of car mufflers, due to its high propensity for oxygen dissociation and adsorption and hence for the promotion of oxidation reactions [1]. Its interaction with gas phase atoms and molecules, therefore, not only has a fundamental interest but is also directly linked to practical applications.

The catalytic oxidation of hydrogen on Rh(110) will be studied in detail in this work and its fine mechanism elucidated.

The second process is the same oxidation reaction but on a high coverage, compressed oxygen structure on Rh(110), which can be considered as a link between adsorbate systems and oxide phases and thus represents a first step towards more complicated (and thus more real) catalysts. This structure involves strain and segmentation of the first metal layer and is therefore a perfect model system for the study of their influence on the reactivity of a metal surface. A very important question, in fact, raised in the last years about the possibility of tailoring the reactivity of a metal surface by means of strain, which results in a shift in the centre of the metal *d* band [2].

Oxides are often seen as "the next step" in surface science, because they are used as a support for metal particles in a variety of applications.
Metal catalysts supported on an oxide are already real catalysts. Important examples are the Ni/Al_2O_3 (and also Pt or Rh/Al_2O_3) system, which is employed in steam-reforming reactions of hydrocarbons, and the Fe/CaO/Al_2O_3/K_2O system, which is used to synthesise ammonia starting from N_2/H_2 mixture. Methanol is synthesised from CO/H_2 on Cu/ZnO/Al_2O_3; Pt, Pd or Rh supported on CeO_2-ZrO_2/Al_2O_3 catalyse oxidation reactions of CO and of hydrocarbons and reduction reactions of NO_x from car exhaust in three way catalysts.
In this PhD work, as an example of a supported metal catalyst used in oxidation reactions, the nucleation and growth of gold clusters on the (110) oriented rutile TiO_2 surface will be presented. This study will give a clear-cut answer to the question of where gold binds. Moreover it will be shown how the temperature can influence the behaviour of metal particles and thus the composition and the performance of a catalyst.

At the end of the thesis, a short chapter is devoted to the description of an ongoing project for the development of a Fast STM module, which allows improving the time resolution of the instrument by three orders of magnitude.
With this development it will be possible to investigate dynamical processes in a wider temperature range, which means that even processes which are not active at low temperature will become accessible, thus making a further step towards the study of real processes.

Most of the work has been done in Trieste, at the Laboratorio TASC-INFM. Only the Au/TiO_2 system has been studied in Århus, Denmark, within the research group of Professor Flemming Besenbacher.

Chapter 1

Introduction to Scanning Tunneling Microscopy

1.1 Introduction

This thesis is based on experiments with Scanning Tunneling Microscopy (STM).
The STM, developed by Binning and Röhrer about twenty years ago, belongs to the class of scanning probes, in which the signal of a local probe is recorded while moving the tip laterally.
In STM the local probe consists in a sharp metal tip which is scanned along the sample: the tunneling current between tip and sample is measured as a function of the position. This procedure delivers images with a lateral resolution up to the range of ångströms; surfaces can thus be imaged with atomic resolution. Actually an image obtained in this way is not exactly a topography of the surface but a convolution with the electronic states. However roughness and morphology of the surface can be observed in an unprecedented way.

The unique advantage of an STM is the ability of obtaining images both on the atomic and the microscopic scale and the possibility of operating both in UHV and at high pressure and in liquids.
In this thesis imaging was always performed in UHV ambient; during scanning, though, pure gases were introduced in the system and thus reactions could be monitored on the atomic scale.

In the following, the basic principles on which the technique is based are briefly reviewed and particular attention is paid to the interpretation of STM images.

1.2 Basic principles

When a metal tip is approached to a conductive surface, before bringing the two parts in contact, a narrow vacuum potential barrier is created. When applying an external bias voltage, a current can flow across this barrier, due to a purely quantistic effect. This current is called "tunneling current" and is due to the extension of the wave functions of the two "electrodes" into the vacuum and to their mutual overlap.
The tunneling current is dramatically dependent on the tip-surface distance (it varies by one order of magnitude if the distance is changed by 1 Å); it senses therefore all small variations in height on the surface.

Images can be acquired in two different ways: in the so-called "Constant Height" mode or in the so-called "Constant Current" mode. In the former case the tip is kept at fixed vertical position and variations in the tunneling current are measured. This allows higher scanning frequencies but the tip is not protected from crashes into surface bumps. In the "Constant

Current" mode (the mode used for all measurements in this work) a feed-back circuit is introduced (see Figure 1.1) which regulates the tip height in order to keep constant the tunneling current while scanning.

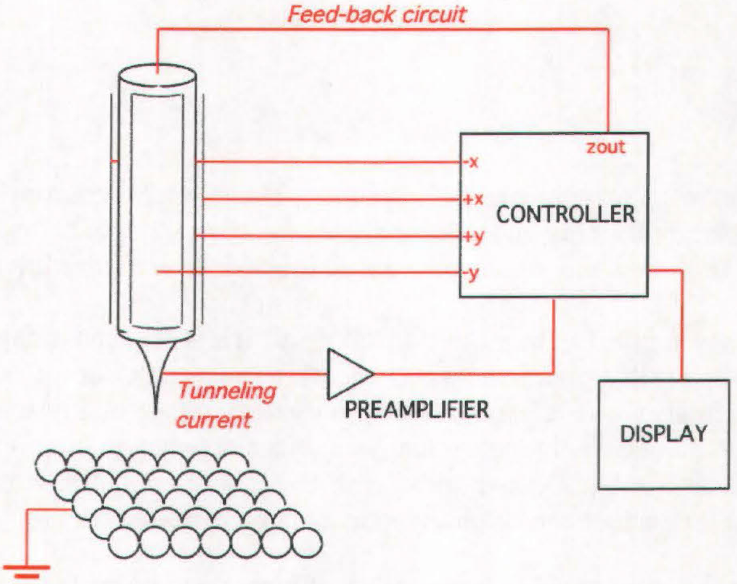

Figure 1.1: *Schematic representation of an acquisition system for an STM operating in Constant Current mode.*

This means that while scanning along a line over the sample (as in Figure 1.2), a profile of the surface is measured. By repeating this procedure line by line over an entire area of the sample and by converting the vertical movements into greyscale levels, an "image" of the surface is produced.

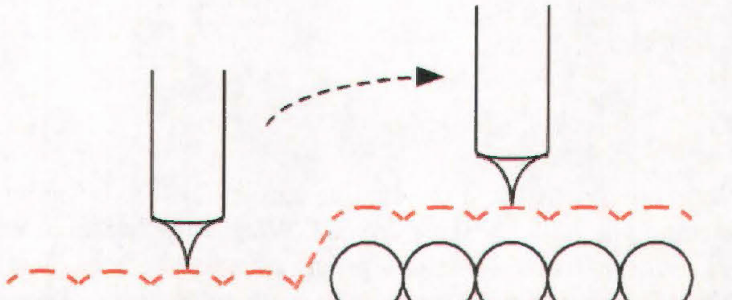

Figure 1.2: *A line scan across the sample in Constant Current mode.*

The origin of the tunneling current can be understood within a very simplified model [3].

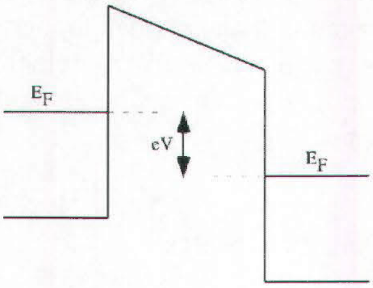

Figure 1.3: *Schematic potential barrier between electrodes for vacuum tunneling when a voltage V is applied.*

Figure 1.3 shows the potential energy diagram when a fixed voltage is applied between two electrodes (in our case the tip and the sample) separated by a vacuum barrier, schematically approximated with a rectangular shape. Within the quantum-mechanical formalism, the wave functions of the electrodes expand also in the classically forbidden region, where they assume a decreasing exponential profile. In fact the wave function of an electron within a rectangular barrier has the form:

$$\Psi(z)=\Psi(0)e^{-kz} \tag{1.1}$$

k is defined by the expression:

$$k^2=2m(V_B-E)/\hbar^2 \tag{1.2}$$

where m is the electron mass, V_B the potential barrier height, E the electron energy and $\hbar$ the reduced Plank constant.

The transmission probability, which corresponds to the tunneling current, is given by the square of the wave function, thus:

$$I \propto e^{-2kz} \tag{1.3}$$

This means that if the two electrodes are placed at a distance z an electron with energy E can "tunnel" from the negative to the positive biased electrode, giving rise to the current I calculated above. The same holds for all electrons with energy within E_F and E_F-eV with more energetic electrons facing a lower barrier and thus having a higher tunneling probability, and the total, measurable current is the integral of all contributions.

Relation (1.3) explains why the tunneling current is so sensitive to the tip-sample distance. Atomic scale images require, as a consequence, a precise control of the tip position and an extraordinarily high signal-to-noise ratio. The former problem is solved by using a scanning tube made of a piezoelectric material, which can be accurately deformed by applying a voltage. The control of the tip height on the scale of less than a tenth of an Ångstrom requires a proper vibration isolation system.

1.3 How to interpret an image

Interpretation of STM images is not always straightforward. First of all, as already stated, an STM image brings more information than simply a topography of the surface. In addition, there are many factors that can influence the measurement, starting from the actual tip configuration. Even harder is the interpretation when adsorbates are imaged. These three points are discussed in the following.

1.3.1 Topography and Density of States

Relation (1.3) is obviously only an extreme approximation of the real tunneling current. The general expression for the tuneling current is [4]:

$$I = \frac{4\pi e}{\hbar}\int_{-\infty}^{+\infty}\left[f\left(E_F - eV + \varepsilon\right) - f\left(E_F + \varepsilon\right)\right] \times \rho_S\left(E_F - eV + \varepsilon\right)\rho_T\left(E_F + \varepsilon\right)|M|^2 d\varepsilon \tag{1.4}$$

where $f(E)$ is the Fermi distribution function, ρ_S and ρ_T are the densities of states (DOS) of the sample and the tip respectively and M is the tunneling matrix element due to the interaction between the sample and the tip.

When approximating the Fermi function to its zero-temperature expression:

$$I = \frac{4\pi e}{\hbar}\int_{0}^{eV} \rho_S\left(E_F - eV + \varepsilon\right)\rho_T\left(E_F + \varepsilon\right)|M|^2 d\varepsilon \tag{1.5}$$

In order to calculate the matrix element, both the wave functions of the tip and of the sample should be known but the tip wave function depends on the actual atomic structure of the tip, which is usually unknown.

Within the simplest approximation, due to Tersoff and Hamann [5], which is based on the "transfer hamiltonian" formalism introduced by Bardeen [6], the tip is assumed to be locally spherical and described by an *s*-wave function. In this case, (1.5) can be reduced to:

$$I \propto eV\rho_S(z,E_F) \tag{1.6}$$

within the limit of small external biases, where $\rho_S(z,E_F)$ is the local density of states (LDOS) at the Fermi level in z and z is the tip-sample distance.

As a consequence, an STM image is not exactly a topography of the surface but rather a convolution of topographic and electronic information. Attention has thus to be paid to the interpretation of all features seen by STM. Topography is due to the total charge density but STM is mainly sensitive to the density of states at the Fermi level. This effect can be almost neglected if a clean metal surface is imaged but can become predominant when working with semiconductors or adsorbate covered surfaces.

Figure 1.4 schematically shows what happens when a positive or a negative voltage is applied to the sample: in the former case electrons tunnel from the tip to the sample, thus mapping its empty states, while in the latter case the current flows in the opposite direction, which means that occupied states are revealed. Therefore, images of the same area of the surface, recorded with opposite bias, can be completely different.

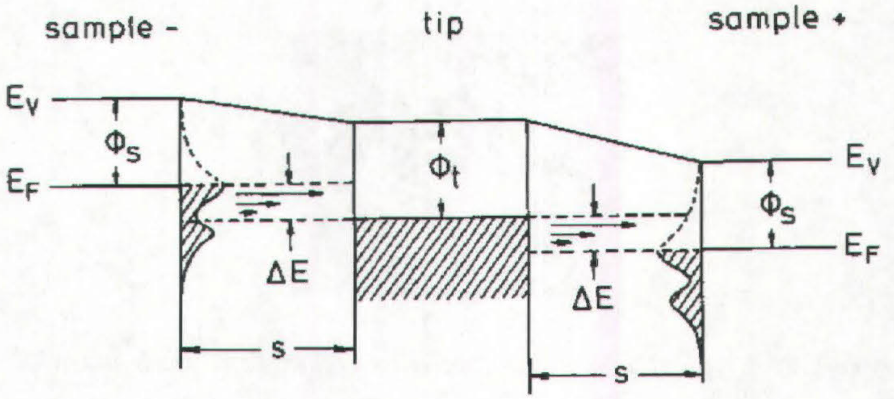

Figure 1.4: *Tunneling from the tip to empty sample states (for positive bias) and from occupied sample states to the tip (for negative bias). States lying higher in energy have a higher tunneling probability.*

1.3.2 The Tip

Another parameter having a fundamental influence on the appearance of an STM image is the tip.

This reflects first of all in the lateral resolution [3]. An ideal STM tip should end with a single atom. As sketched in Figure 1.5, in case of a sharp tip only electron states located in a narrow area behind it participate to the tunneling. Conversely, if the tip is bland the tunneling current derives from a much wider area. However, the exponential dependence of the tunneling current on the tip-sample distance indicate that a good STM tip does not have to be sharp on the atomic scale to give atomic resolution. This makes working with a real STM tip possible.

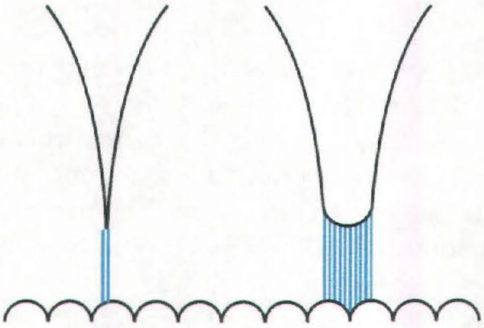

Figure 1.5: *Tunneling with a sharp and a bland tip.*

Nevertheless, in order to achieve atomic resolution, sharp STM tips have to be prepared.
In our system tips are made starting from a 0.38 mm wide tungsten wire, which is electrochemically cut in a NaOH solution. If the wire is placed in the middle of a thin layer of the basic solution, suspended on a gold ring, and a voltage (≥+4 V) is applied between the wire and the ring, W is oxidised and thus dissolved, until the wire is cut. This procedure results in sharp tips like the one in Figure 1.6, capable of atomic resolution.

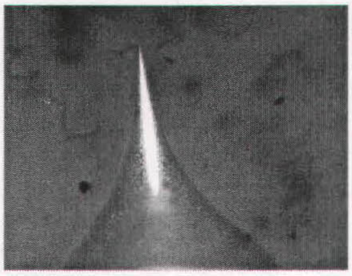

Figure 1.6: *A typical STM tip obtained by etching of a 0.38 mm wide W wire.*

Even a sharp tip does not guarantee good STM images. Tips, in fact, are deformed and somehow "consumed" during scanning, leading to images with unpredictable aspects.
A typical example of a modified tip is a double tip. In this case a single point of the image is the result of the superposition of the signals coming from two distinct points of the surface and thus the picture is unreal.
Tips can also be modified in their "chemical identity". This means that foreign atoms can attach and give origin to the current. As a consequence STM images can be completely different. These kinds of tip modifications are not accounted for within the Tersoff-Hamann approximation. The tunneling current is more appropriately represented as a process that includes interactions between the tip and the sample. According to Ruan *et al.* [7], different tip atoms may form stronger or weaker tip-surface atom chemical bonds. The formation of a chemical bond between the tip and the sample may increase or decrease the density of states at the Fermi level, since antibonding states, resulting from tip-surface atom interactions, are either shifted up or pushed away form E_F. Therefore, the STM signal is altered.

1.3.3 Imaging of Adsorbates

Interpretation of STM images is even less straightforward when adorbates are imaged.
Often the apparent height of an adsorbate does not even qualitatively correspond to the geometric arrangement. The situation resembles that of semiconductor surfaces, where STM images can be understood only by considering their electronic structure. Unlike the DOS of metal surfaces, the adsorbate-induced DOS may exhibit a pronounced spatial and energetic structure. Adsorbates can modify the LDOS at the Fermi level by electronic states derived from adsorbate orbitals. Even if these are centred well below or above the tunneling energy window, the density of states in the tunneling energy interval may still be affected by the tail of adsorbate resonances. In addition, the metal electronic structure can be changed by

polarisation effects or by the removal of surface states. As a consequence, generally STM contours of adsorbates do not simply reflect the position of their ion cores.

Lang [8] showed that, based on the Tersoff and Hamann approximation, qualitative predictions of adsorbates on metal surfaces can be made. He modelled the tip as a Na atom on a jellium surface (model free-electron substrate) and different atoms (Na, S and He) adsorbed on the other surface (modelled as jellium as well) were investigated. The calculated density of states for Na show an enhancement at E_F caused by the 3s Na resonance just above E_F (see Figure 1.7, left) and the resulting contour of constant current presents a large protrusion at the position of the sodium atom (Figure 1.7, right). Conversely, the 3p resonance of S is considerably below E_F, thus the enhancement is less and the protrusion above the atom is smaller. In addition the S atom sits closer to the surface. The Helium filled valence shell is far below E_F and does not contribute to the tunneling but it polarises the metal surface just below the atom, with a decrease in the Fermi state density and thus a reduction in the current. For this reason a He atom appears as a depression.

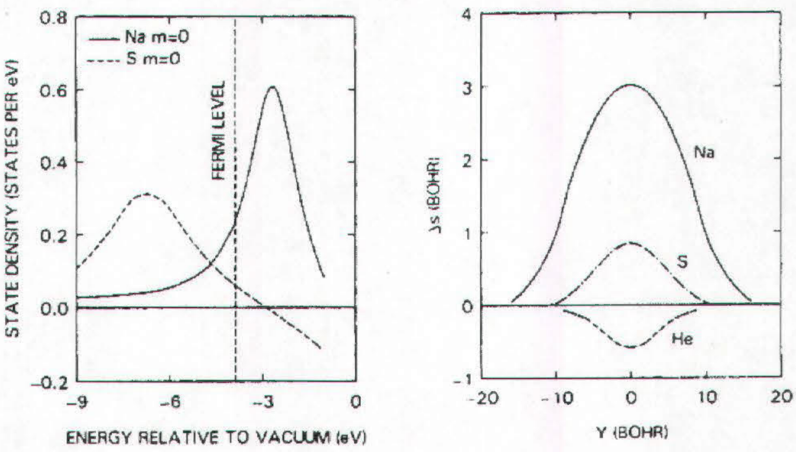

Figure 1.7: *Calculated density of states of Na and S (left) and calculated contours of constant tunneling current for Na, S and He (right) [8].*

Within a more realistic approach, Tilinin and coworkers [9] proved that depressions are deeper when the adsorbate is more electronegative.

In particular, for an oxygen atom [9,10], there is a considerable charge transfer from the metal to the 2p O orbitals. These states, however, are far below the Fermi level and thus do not contribute to the tunnel. Doyen *et al.* calculated that charge is transferred also to the 3s O levels and this leads to an increase in the LDOS at the Fermi level at large distances from the surface. Nevertheless, the main effect of oxygen adsorption that influences the tunneling is the polarisation of the metal surface, with the formation of a depletion area just below the atom. As a consequence, in STM images oxygen is revealed as a depression, even though it may be imaged as a protrusion at large distances (>6 Å). Oxygen can also be imaged as a protrusion at short distances when the chemical identity of the tip is changed (see Section 1.3.2).

Fortunately interpretation of STM images is often less complicated than expected. Many of the problems just exposed can be overcome when working on a system where fingerprints of reference studies are already known. This allows, for instance, to compare similar features in the images and thus to assign them to a particular structure. Moreover, if the structure is known, an image can be "read" even when the contrast is unusual due to tip effects. Help can come also from other experimental techniques. Spectroscopic studies, for example, can give pieces of information about the nature of the species present on the surfaces, thus filling the lack of chemical sensitivity, one of the main disadvantages of STM. Finally, in the recent years calculation capabilities have improved and simulations of STM images are being more and more used.

Chapter 2

The Experimental Setup

2.1 Introduction

All experiments have been performed in UHV systems. UHV systems have low base pressures (in our case 5×10^{-11} mbar) in order to avoid contamination of the surface over a long time period: at 1×10^{-10} mbar, a contaminant with a sticking coefficient of 1 and mass 28 needs ~10000 sec to cover a Rh(110) surface with a coverage of 1 ML. This is a prerequisite for reliable studies, especially for a technique which is very sensitive to single contaminants, and which does not allow a straightforward attribution of single features to specific chemical species.

Except for the $TiO_2(110)$ experiments, all measurements have been performed in the UHV system at Trieste, which is described in details below. This system houses a Variable Temperature STM made by Omicron (VT-STM), capable of measuring at temperatures between 130 K and 600 K.
The $TiO_2(110)$ measurements have been performed in Århus with a variable temperature STM built by the Besenbacher group, capable of measuring between 110 K and 400 K. Chamber and STM are described in ref. [11] and will be briefly presented in Chapter 5.

2.2 The UHV System

The UHV system consists of a main chamber for sample preparation, to which a small chamber is attached, where the STM is housed (see Figure 2.1). The system is pumped by a magnetic turbomolecular pump, an ion getter pump, a Ti-sublimation pump and a getter pump.
The vibrational decoupling of the turbomolecular pump and its prepumping stage is such that the pumps do not affect the STM resolution.

The preparation chamber is equipped with a manipulator (see Section 2.4.1 for description), in which the sample can be cooled down to 90 K by means of liquid nitrogen and heated up to 1300 K by means of a PBN (pyrolytic boron nitride) heater, inserted into the sample holder.
The following instruments are available:

- sputter gun for sample cleaning with Ar^+ ions
- mass spectrometer for control of gas cleanliness and sample characterisation by TDS (Thermal Desorption Spectroscopy). This technique consists in heating the surface in a controlled way while the desorbing products are monitored by the mass spectrometer. Thus pieces of information about desorption parameters and about the nature and the amount of adsorbates initially present on the surface can be inferred.

- LEED/AES.

  LEED (Low Energy Electron Diffraction) is a standard technique used for obtaining structural information about surfaces and is applied both to check the crystallographic quality of the sample and to obtain information about the adsorbate induced structures. Since a diffraction pattern corresponds essentially to the surface reciprocal lattice, the reverse transformation yields the periodicity in real space.

  AES (Auger Electron Spectroscopy) is a widely used spectroscopic technique, applied to check the cleanliness of a freshly prepared surface and for analysis of surface chemical composition.
- gas doser (see Section 2.4.2 for description)
- evaporator for dosing, for example alkaline metals, by heating a filament of the desired material.
- Fast Entry Lock
- hot filament ion gauge

The Fast Entry Lock and the gas doser are pumped separately (both of them toghether or one at the time) by a separate turbomolecular pump with its prepumping stage. These pumps have to be switched off before starting STM measurements.

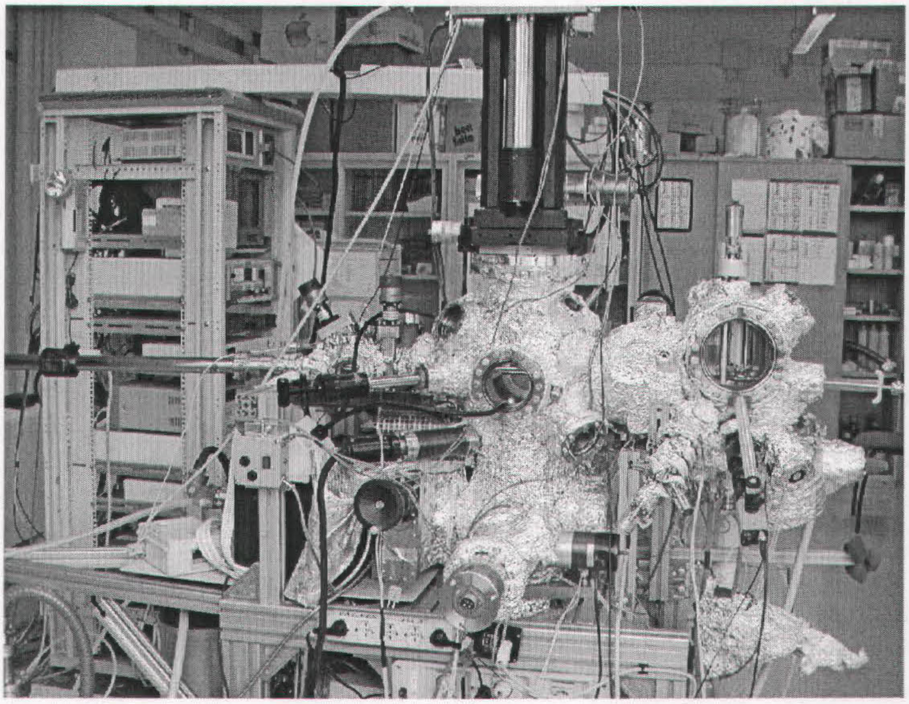

Figure 2.1: *The experimental system with preparation chamber in the centre and STM chamber to the right.*

2.3 The STM

The Omicron VT-STM (Figure 2.2) can be cooled down to 130 K by filling a liquid nitrogen bath cryostat, which is then pumped by a diaphragm pump in order to freeze the liquid nitrogen. A copper braid connects the cryostat to a cooling block that can be placed in direct contact with the back of the sample holder.

Figure 2.2: *The Omicron VT-STM.*

The sample can be heated in the STM up to 600 K by a PBN (pyrolytic boron nitride) heating element inside the sample holder. Since the electrical connection between STM sample stage and feed-through on the chamber is given by thin Kapton isolated wires (in order to avoid vibrational coupling), the heating current is limited to 1.8 A. The maximum temperature depends on the PBN resistance, in our case 600 K could be reached.

All intermediate temperatures are accessible by applying an appropriate heating current, with or without filling the cryostat.

Since this regulation requires an accurate temperature reading, which is not available for the commercial Omicron VT-STM, a major part of the development of the instrumentation has been the insertion of a thermocouple, as described in Section 2.4.3.

Vibrational isolation is made by means of a spring suspension system, which suspends a heavy base platform of the STM. The base platform suspension is damped by an eddy current system: the platform is surrounded by copper plates, which are centred between permanent magnets, fixed on the chamber.

The sample is mounted in the STM sample stage with the surface pointing downwards and the tip is approached to the sample from the bottom up. The coarse approach, up to some tens of microns, is made using a CCD-camera. The fine approach is then performed automatically.

Conversely to most STMs, in this instrument the sample is at ground potential and the bias is applied to the tip.

2.3.1 Tip Treatments

Tips are daily sputtered for 2÷5 minutes with Ar^+ ions ($p_{Ar}=1\times10^{-6}$ mbar). The system is not equipped for tip heating but usually sputtering is enough to restore tips which resolve atomically. Additional treatments are performed during scanning, mainly bias pulses and tip shaking. Sometimes very fast scanning on large surface areas is useful.

2.4 Instrumentation Improvements

During my doctoral thesis, several improvements to the experimental setup have been developed.

2.4.1 The New Manipulator

First of all, a new manipulator head has been built (Figure 2.3). It consists of a copper-aluminium alloy (GLIDCOP) which is thermally coupled but electrically isolated from the manipulator axis by a sapphire plate. The manipulator tube can be filled with liquid nitrogen.

In the manipulator head two sample stages are integrated.
A heating stage is composed of a molybdenum cage, thermally decoupled from the remaining part of the manipulator. In this way thermal dispersion is minimised and the heat produced by the PBN heater remains concentrated at the sample holder. The same stage allows also for accommodation of tipholders for tip sputtering.
The cooling stage is directly carved into the GLIDCOP material in order to have a maximum contact between the back of the sampleholder and the manipulator head. This ensures a good thermal contact.
On both stages a lateral contact connects the PBN heater and two thermocouple contacts (type K) allow readout of the sample temperature (see Section 2.4.3).
A third stage below the manipulator head hosts an electrode for field emission treatments of the tip (not used in this work).

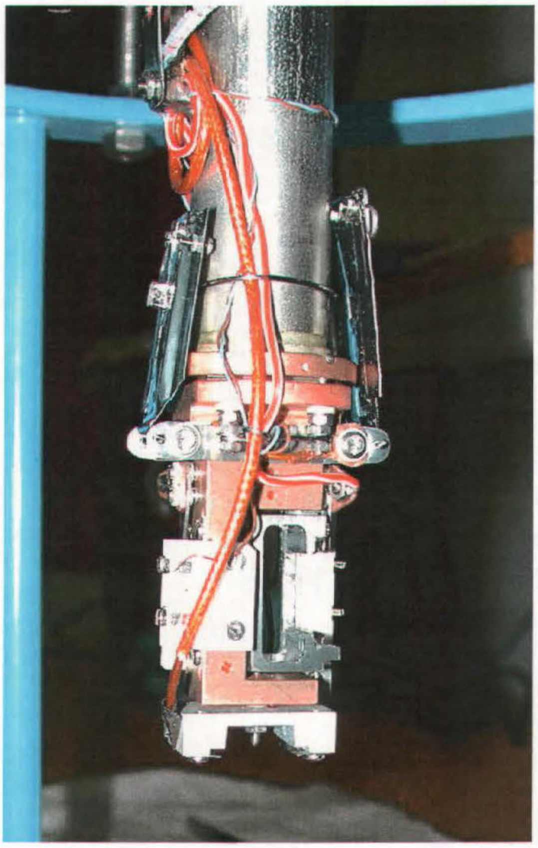

Figure 2.3: *The head of the manipulator. On the right part, the molybdenum cage of the heating sample stage, inserted into the GLIDCOP block of the manipulator.*

2.4.2 The Doser

One of the major problems when working with reactive gases, like H_2O or NH_3, is the effect of dosing on the background pressure. These gases have a high sticking coefficient and background dosing may increase drastically the background pressure after dosing, due to gradual desorption from the chamber walls.

In order to reduce the effect of dosing on the background pressure, the dosing can be focused by means of a gas doser, placed directly in front of the sample. The partial pressure of the reactive gas in front of the sample can therefore be increased locally, thus reducing the exposition time and avoiding a prolonged exposure of the rest of the chamber to the reactive gas.

Operating with the gas doser, the sample could be saturated with H_2O with an increase in the background pressure of less than 5×10^{-10} mbar. Intermediate exposures are difficult to control since the local increase of partial pressure should be known.

The doser is composed of a tube, connected to the gas-line by a valve, which can be inserted into the main chamber. At the end of the tube there is a microchannel plate that can be placed immediately in front of the sample, at a distance of less than 5 mm. The valve directly connecting the gas-line to the chamber is closed and the gas-line is filled with a high pressure of the desired gas (usually ~2×10^{-5} mbar). At this point the doser valve is open and the gas flows through the channel plate straight to the surface, which means a much efficient and thus faster exposure with only a slight increase in the background pressure. When the exposure is terminated the doser valve is closed and the gas-line is separately evacuated and then baked.

2.4.3 The Temperature Control

The sample holder and the STM have been modified to enable to read the temperature directly on the surface, even in the STM. The standard Omicron system, in fact, involves only a silicon diode for readout of the temperature of the clamping block attached to the base plate of the sample holder when working at low temperature. A calibration of the applied power is needed for measurements at high temperatures. In both cases the uncertainty is high: the silicon diode is placed far apart from the surface; the power calibration does not take into account the heat dispersion towards the sample stage.

Our idea was to use a transferable thermocouple in direct contact with the sample.
The ceramic plate of the sample holder has been modified as shown in Figure 2.4 by introducing two "contact loops". Thermocouple wires (chromel-alumel) connect the contact loops to the lateral side of the sample, where they are spotwelded (or tied in case of non-conductive samples).
These contact loops touch contact springs in the STM sample stage.

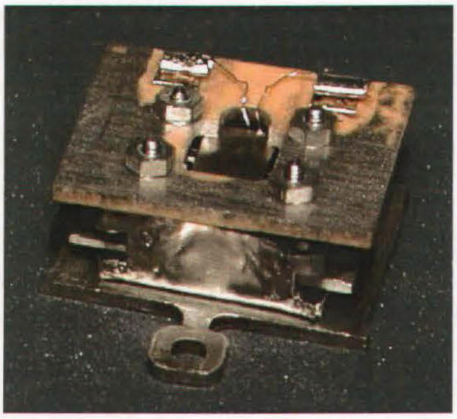

Figure 2.4: *The modified sample holder with the thermocouple contacting the sample.*

Particular care had to be taken when modifying the STM sample stage in order to avoid alteration of the vibrational damping. A Macor block is introduced underneath the sample stage (see Figure 2.5). Two laminas (one made of chromel and one of alumel) are fixed to the block and act as spring contacts for the contact loops when the sample is inserted. From the laminas two thermocouple wires transfer the signal to a feed-through. The signal is then read by an Eurotherm controller that controls the heating current power supply. A temperature control down to a tenth of a degree can be reached.

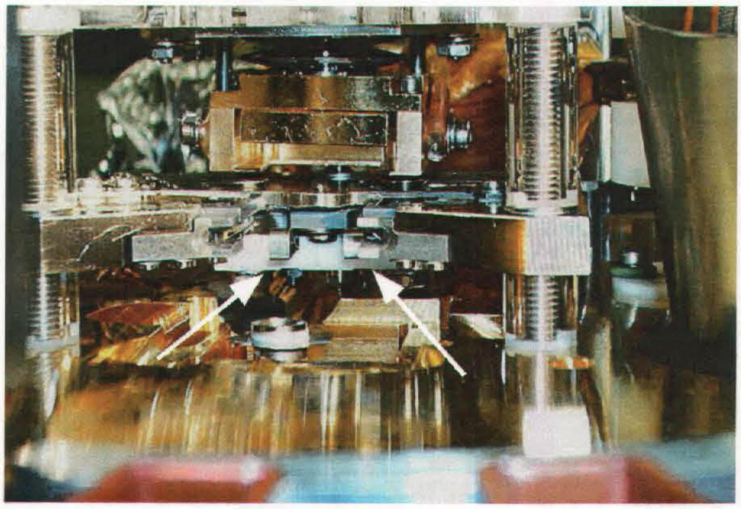

Figure 2.5: *Thermocouple contacts inside the STM (see arrows).*

This solution turned out to be extremely efficient because it did not require relevant modifications of the instrument neither alters its performances.

Chapter 3

Reactivity of an Unreconstructed Surface: (2×1)p2mg-O/Rh(110)

3.1 Introduction

The simplest model catalyst studied in this thesis is the unreconstructed (110) surface of rhodium.

This transition metal has been widely investigated in the last ten years and its interaction with gases such as oxygen, nitrogen monoxide and carbon monoxide is known. Also the reactivity of rhodium has been studied with many techniques. Nevertheless, up to now there are only a few examples of catalytic reactions on Rh(110) that have been examined in details on the atomic scale. This is the case of the catalytic oxidation of carbon monoxide on the (1×4) reconstructed surface [12,13] and the catalytic oxidation of hydrogen on the (1×2) reconstructed surface [14].

The aim of this part of my PhD work is to analyse the mechanism of the catalytic oxidation of hydrogen to form water, starting from the (1×1) unreconstructed Rh(110) surface previously saturated by oxygen.

Historically, the catalytic reaction between oxygen and hydrogen is the first catalytic reaction ever studied.

Döbereiner discovered at the beginning of the XIX century that platinum catalyses the reaction between oxygen and hydrogen [15]. Similar observations prompted Berzelius to coin the term "catalysis" to describe this kind of phenomena [16].

After about two hundred years, the mechanism on the atomic scale still offers unknown details on various surfaces.

The chapter is structured as follows:

First, an introduction about oxygen induced structures on the Rh(110) surface and examples of catalytic oxidation of hydrogen on metal surfaces are presented. STM results of the reaction of the (2×1)p2mg-O/Rh(110) structure are discussed in Section 3.4. In Section 3.5 the formation of an OH layer as intermediate product of the reaction is characterised by TDS and STM. In Section 3.6 these results are then confronted with the STM data on the reaction. Finally, Section 3.8 summarises the reaction mechanism.

3.2 Oxygen on Rh(110)

At temperatures above 100 K dissociative adsorption of molecular oxygen occurs on Rh(110) and atomic oxygen forms a variety of ordered structures [1]. If the temperature is high enough to allow the diffusion of Rh atoms on the surface (~400 K), these structures involve a reconstruction of the substrate [17]. In particular, as the O coverage is increased, the surface undergoes (1×*n*) reconstructions (*n*=2÷5), where one rhodium row out of *n* is missing and all the remaining rows are decorated by O in threefold sites in a zig-zag fashion in the following sequence:

O coverage	0.5 ML	→	0.67 ML	→	0.75 ML	→	0.8 ML
substrate reconstruction	(1×2)	→	(1×3)	→	(1×4)	→	(1×5)
resulting structure	(2×2)p2mg	→	c(2×6)	→	c(2×8)	→	c(2×10)

Figure 3.1 presents an STM image and the model of the (2×2)p2mg structure. In the image bright rows are metal close-packed rows. Oxygen atoms are imaged as depressions (which is the usual contrast for this adsorbate - see Section 1.3.3) and are responsible for the zig-zag appearance of the rows. As the image clearly shows, the phase is generally preserved between adjacent rows [18,19].

Figure 3.2 illustrates the c(2×2*n*) structures, which are obtained by dosing more oxygen on the (2×2)p2mg at T≥650 K. In these structures zig-zag oxygen atoms are in phase within the small terraces between consecutive missing rows but in antiphase between adjacent terraces [20].

Completely different is the situation if further oxygen is dosed on the (2×2)p2mg structure at slightly lower temperatures (400 K÷600 K). In this case a metastable, oxide-like structure is formed with a (10×2) symmetry [21]. This surface will be the subject of Chapter 4.

As already stated, all these structures form only when dosing is performed at elevated temperature or an annealing of the surface follows the low temperature exposure. This fact indicates that their formation is an activated process.

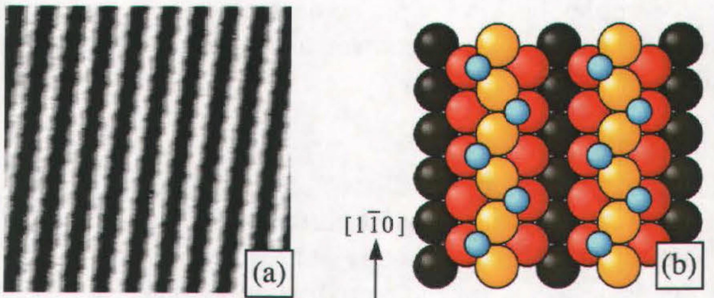

Figure 3.1: *(2×2)p2mg-O/Rh(110). (a) STM image. Size: 70×70* $Å^2$. *(I=0.95 nA,* V_B*=+0.36 V). (b) Model of the structure: yellow circles are first layer rhodium atoms while small blue circles are oxygen atoms.*

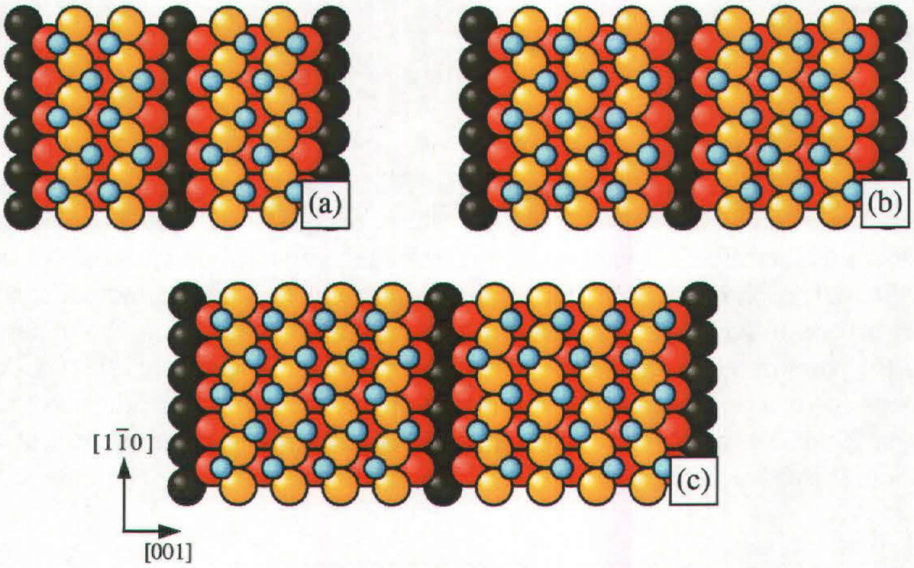

Figure 3.2: *Models of the c(2×2n)-O/Rh(110) structures. (a) c(2×6). (b) c(2×8). (c) c(2×10).*

Conversely, oxygen adsorption at low temperatures ($T \leq RT$) does not involve any substrate reconstruction. At a coverage of 1 ML a well ordered (2×1)p2mg is produced. In this structure O atoms sit in threefold sites, again in a zig-zag fashion, coordinated by two surface atoms and one second layer Rh atom [22,23,24]. In Figure 3.3 a schematic model of the structure is shown.

In all cases, therefore, threefold sites appear to be the most stable sites for oxygen adsorption on the Rh(110) surface.

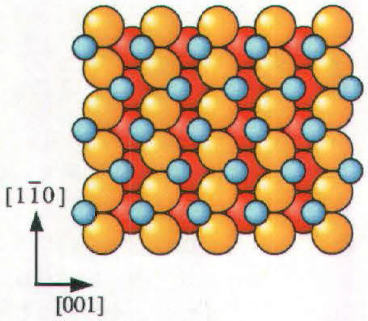

Figure 3.3: *Schematic model of the (2×1)p2mg structure. Yellow circles are first layer rhodium atoms while small blue circles are oxygen atoms in threefold sites.*

Nevertheless, vibrational [25] and photoemission [26] studies ruled out the occupancy of threefold sites on the unreconstructed substrate below 0.35 ML.

Hla *et al.* [27] found that the formation of the (2×1)p2mg structure is indeed preceded, at lower coverages, by the presence of pairs of oxygen atoms oriented along the [001] direction, which aggregate in chains along $[1\bar{1}0]$, leading to a local order in a (2×3) or a c(2×6) structure. From STM images as the one shown in Figure 3.4, the authors measured an atomic distance in the pairs varying with the coverage from 3.3 Å (at the lowest coverage) to 2.5 Å (at the highest one), always shorter than the lattice constant (3.8 Å). They propose a model where O atoms sit in adjacent asymmetric short bridge sites, sliding, with increasing coverage, towards the threefold sites, which is indeed the adsorption site for a full monolayer coverage. Photoelectron diffraction studies, however, indicated that the actual adsorption site is the short bridge site at all investigated low coverages [28] and thus the apparent shorter distance in the pairs in STM images has to be attributed to an electronic effect. Conversely to what happens for oxygen atoms in the majority of cases (also in all other oxygen induced structures on Rh(110)), oxygen atoms in the pairs are usually imaged as protrusions whose height is about 0.2÷0.3 Å.

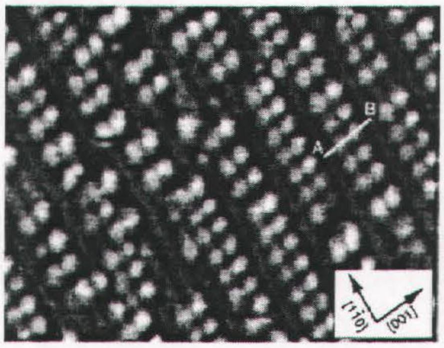

Figure 3.4: *STM image of oxygen atom pairs after adsorption of 0.26 ML at 170 K. Size: 110×80 Å^2 [27].*

3.3 Catalytic Oxydation of Hydrogen on Metal Surfaces

The catalytic oxidation of hydrogen on metal surfaces has been widely studied. A few examples will be presented in the following, trying to give an idea of O + H interaction and reaction, used for comparison with the reaction on the Rh(110) surface, both in this and in the following chapters. Particular attention is paid to the reaction on rhodium surfaces.

On an oxygen covered surface which is exposed to gaseous hydrogen, coadsorption of O and H atoms can take place without the occurrence of a reaction. This is the case, for example, of W(110) [29]. On this surface there is a strong mutual H-O influence, even though without any displacement, but no evidence for OH or H_2O formation was found.
A displacement of oxygen atoms due to hydrogen adsorption was instead reported in a recent STM study on Pd(111) [30]. On this surface the initial (2×2)-O structure is compressed first into chain-like structures, near 120 K, and then into a (√3×√3), above 150 K. The former

structure is composed by rows of oxygen atom pairs at nearest neighbor distance, as shown in Figure 3.5. Both modifications start at the edges of (2×2) islands and the total number of O atoms remains constant, which means that no water is produced. The (√3×√3) is stable up to 210 K, when these compressed oxygen islands expand back to a (2×2) ordered phase without loss of oxygen. This is related to a decrease of hydrogen coverage, due to dissolution into the bulk. Above 220 K hydrogen segregates back from the bulk to the surface and a reaction with oxygen indeed takes place: OH groups form and are immediately converted to water that desorbs. This process is too fast to be followed by STM and thus only a shrinking and then the disappearance of oxygen islands are seen in the images.

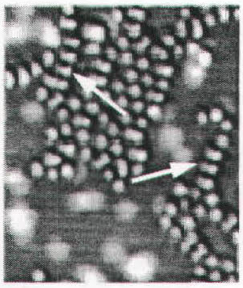

Figure 3.5: *Rows of oxygen atom pairs formed by compression of the (2×2)-O structure due to hydrogen adsorption on Pd(110) [30].*

If atomic hydrogen, instead of H_2 molecules, is dosed on an oxygen covered metal surface, a direct ER (Eley-Rideal) reaction between gaseous hydrogen and adsorbed oxygen occurs. This happens, for example on the Ru(001)-p(1×2)-O surface [31]. A similar behavior was found on Cu(100), where exposure of the O covered surface to atomic hydrogen leads to water production via three elementary reaction steps [32]. Below 180 K two subsequent hydrogenation steps dominate:

$$H_{gas} + O_{ads} \rightarrow OH_{ads}$$
$$H_{gas} + OH_{ads} \rightarrow H_2O_{ads}\ ,\ H_2O_{gas}$$

with the second reaction as the rate determining step. Above 180 K a recombination reaction

$$OH_{ads} + H_{ads} \rightarrow H_2O_{gas}$$

contributes to the water rate. Adsorbed oxygen is completely consumed in the reaction.

The catalytic oxidation of hydrogen on Pt(111) below water desorption temperature is an example of an autocatalytic reaction, as determined by STM and HREELS studies [33, 34]. The reaction is started by direct OH formation from atomic adsorbates:

$H_{ads} + O_{ads} \rightarrow OH_{ads}$ (Step I)

and proceeds by cyclic repetition of

$OH_{ads} + H_{ads} \rightarrow H_2O_{ads}$ (Step II) and

$2H_2O_{ads} + O_{ads} \rightarrow 3OH_{ads} + H_{ads}$ (Step III)

These reactions continue as long as there is a continuos supply of hydrogen and as long as there are O adatoms available.

One cycle of the autocatalytic process converts, thus, two initial OH groups into three OH groups. The process is terminated when locally all O atoms are consumed and the remaining OH is transformed into H_2O through Step II. Step I is very slow but, since trace amounts of water will always be present, it is likely that actually Step III primarily initiates the reaction.

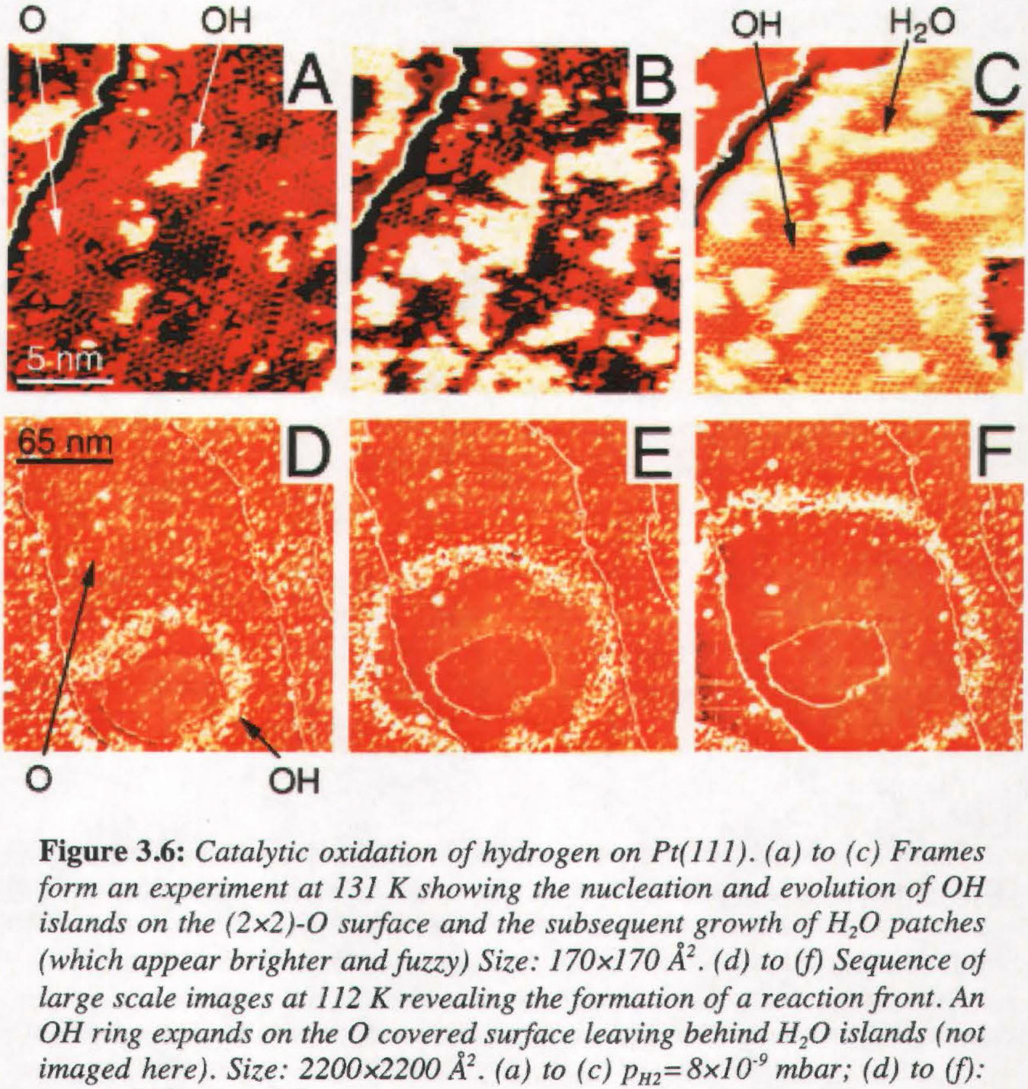

Figure 3.6: *Catalytic oxidation of hydrogen on Pt(111). (a) to (c) Frames form an experiment at 131 K showing the nucleation and evolution of OH islands on the (2×2)-O surface and the subsequent growth of H_2O patches (which appear brighter and fuzzy) Size: 170×170 Å². (d) to (f) Sequence of large scale images at 112 K revealing the formation of a reaction front. An OH ring expands on the O covered surface leaving behind H_2O islands (not imaged here). Size: 2200×2200 Å². (a) to (c) $p_{H2}=8\times10^{-9}$ mbar; (d) to (f): $p_{H2}=2\times10^{-8}$ mbar [34].*

Large scale images (see the lower part of Figure 3.6) show that the reaction proceeds by a wave front. From an initial H_2O cluster an OH ring develops and expands on the surface, always with a constant width. Outside the ring the surface is still covered by oxygen in the (2×2) structure, while inside H_2O islands form. H_2O molecules are easily shifted away by the tunneling tip and thus often are not resolved in STM images (as in the lower part of Figure 3.6).

The following scenario can be inferred for the reaction. Water molecules produced behind the front diffuse to the O covered area travelling across the OH ring in a fast process, probably proton hopping. Here new OH groups are created, thereby driving the O/OH interface outwards. Then OH reacts with H to give H_2O, causing the OH concentration to decrease and the H_2O concentration to increase. The OH/H_2O interface thus follows the outward motion of the O/OH interface. As a result, a circular reaction zone that contains the OH moves through the O covered area, thereby transforming the O into H_2O. This mechanism was qualitatively reproduced by simulations based on a simple RD (Reaction-Diffusion) model [35].

Hence, locally first OH islands develop on the (2×2)-O area, forming a structure where strong attractive interactions due to hydrogen bonds are present. Then H_2O islands, which appear as bright fuzzy patches in STM images, grow. The sequence is presented in the upper part of Figure 3.6.

The autocatalytic mechanism is no longer operative if there is not sufficient H_2O remaining on the surface. For this reason above the water desorption temperature (170 K) H_2O can be formed only by consecutive H addition reactions (Step I and Step II) and both STM and HREELS showed that accordingly no significant reaction takes place at 200 K [33]. Therefore this is an example of a reaction that takes place only at low temperature, conversely to most catalytic reactions.

Finally a few examples of catalytic oxidation of hydrogen on rhodium surfaces.

On Rh(100), O + H layers have been studied by combined TPD, XPS and LEED measurements [36]. It has been found that the OH and H_2O formation is facilitated in dense coadsorbed layers with oxygen coverage in the 0.3÷0.4 ML range. O induced weakening of the H adsorption bond and forcing of H and O to occupy adjacent sites are supposed to be the main factors contributing to favoured OH production. The formation of OH groups in these dense layers involves structural rearrangement of the coadsorbates and gives rise to a new ordered OH + O structure, where OH disproportionation is the dominant mechanism of H_2O formation. Gregoratti *et al.* propose that the main role of coadsorbed O is to induce OH ordering in a configuration that favours the H_2O formation.

The water formation reaction on Rh(110) starting from the (2×2)p2mg-O structure at temperatures in the 380÷405 K range was characterised in a previous study by our group [14].

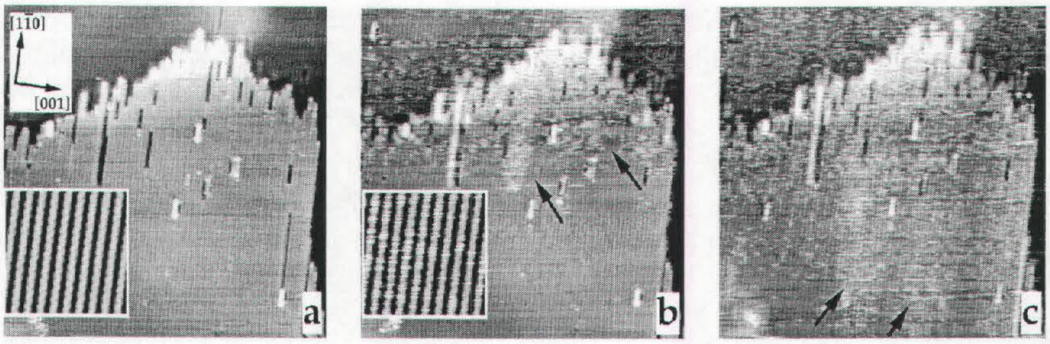

Figure 3.7: *Reaction fronts due to water formation reaction on the (2×2)p2mg-O/Rh(110) at 380 K. (a) Initial surface. (b) Beginning of the reaction with appearance of bright dashes (see insert) in finger-like reaction fronts. (c) Propagation of the reaction front.* $p_{H2}=2\times10^{-8}$ *mbar. Time between images: 44 sec. Size: 610×610* $Å^2$*; inserts: 70×70* $Å^2$*. (I=1.02 nA,* $V_B=+0.39$ *V) [14].*

Conversely to the initial surface presented in the present work, the (2x2)p2mg involves a reconstruction of the substrate (see Section 3.2) which is stabilised by oxygen. Therefore oxygen removal, at temperatures allowing diffusion of rhodium atoms, implies also a deconstruction of the surface. The reaction nucleates at steps and propagates via a reaction front in an anisotropic way, elongated in the $[1\bar{1}0]$ direction. As shown in Figure 3.7, the presence of the reaction is evidenced by the appearance of dashes that can be traced back to the diffusion of oxygen atoms, which sets in as soon as vacancies are created on the metal (1×2) rows. Neither reaction products nor intermediate species could be resolved.

3.4 Cataytic Oxidation of Hydrogen on Rh(110)

The catalytic oxidation of hydrogen on the (2×1)p2mg-O surface has been studied by taking series of STM images during hydrogen exposure, with $p_{H2}=5\times10^{-9}$ mbar on the surface (corrected for the screening factor of 5 of the tip as estimated in [37]).

Several temperatures were checked and it turned out that 260 K is a good compromise between a reaction on a resolvable time scale and an acceptable induction period (of the order of a few tens of minutes).

3.4.1 Preparation of the (2×1)p2mg Structure

In all previous studies, the (2×1)p2mg structure is prepared by simply dosing oxygen on the clean Rh(110) surface at temperatures $T\leq300$ K [1,17,22-24,26]. We found that, on the atomic scale, adsorption at different temperatures within this range leads to slightly different surfaces.

Adsorption at room temperature (300 K) results in a well ordered (2×1)p2mg. The oxygen structure, however, coexists with a local reconstruction, where metal atoms jump on the topmost layer, leaving one-layer deep holes on the surface, and align in chains, elongated in the $[1\bar{1}0]$ direction. Figure 3.8 clearly shows the $[1\bar{1}0]$ rows of the surface, decorated by the zig-zag due to O atoms, often interrupted by holes and chains of ejected atoms. The latter ones are not zig-zagged, which means that there is not oxygen bound to them, and have an apparent height of 1.1÷1.4 Å, in agreement with the usual step height.

If the structure is formed by dosing at 243 K and annealing to 275 K, the density of ejected atoms and holes decreases but other defects appear (see Figure 3.9). *Chain-like* features, which often form closed curves, divide the surface in many small domains, with zig-zag in antiphase between adjacent domains (the presence of chains of expelled rhodium atoms and holes, conversely, is not related to a change in the zig-zag phase). The nature of these *chain-like* features is up to now unknown.

As Figure 3.10 proves, dosing at 200 K and subsequently annealing to 260 K results in a lack in substrate reconstruction but the surface is still divided in phase domains, separated by *chain-like* features.

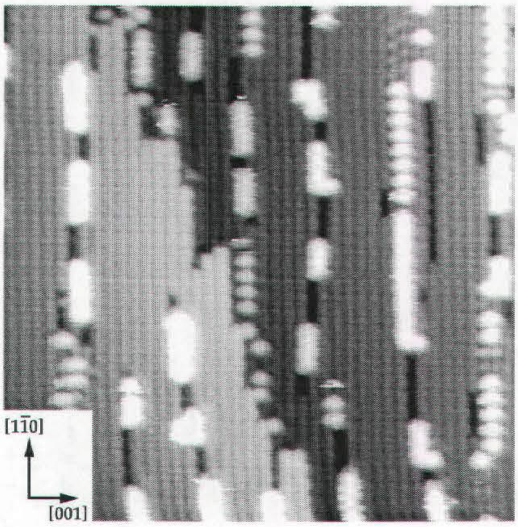

Figure 3.8: *(2×1)p2mg structure obtained by dosing 6 L* O_2 *at 300 K. Size: 200×200* $Å^2$ *(I=1.00 nA,* V_B*=+0.15 V).*

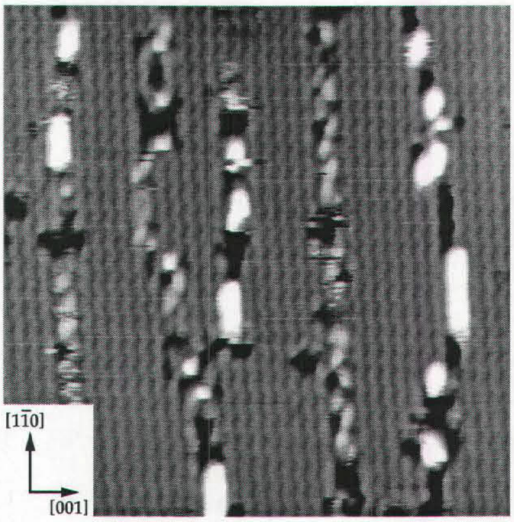

Figure 3.9: *(2×1)p2mg structure obtained by dosing 6 L* O_2 *at 243 K and annealing to 275 K. Size: 200×200* $Å^2$ *(I=0.46 nA,* V_B*=+0.16 V).*

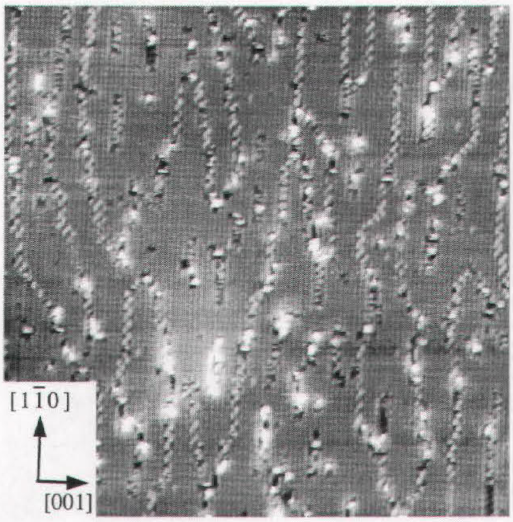

Figure 3.10: *(2×1)p2mg structure obtained by dosing 6 L O_2 at 200 K and annealing to 260 K. Size: 480×480 Å^2 ($I=0.57$ nA, $V_B=+0.19$ V).*

In order to find a better recipe to prepare a defect-free structure, oxygen was dosed at 146 K and then the surface was step-annealed in STM. Images acquired immediately after dosing, are confused (Figure 3.11(a)) and reflect a non-perfectly ordered structure and the presence of contaminants. Resolution improves only after annealing to 200 K, when the (2×1)p2mg structure can be recognized, even though the surface is still partly covered by unknown species. If annealing to 240 K or above, the *chain-like* features appear (Figure 3.11(b)). The local reconstruction sets in only after annealing to at least 320 K (Figure 3.11(c)).

In conclusion the step-annealing experiment was not successful and gave only the information that oxygen adsorption at low temperature makes the substrate more stable towards reconstruction. In fact in this case the surface is still unreconstructed at room temperature, while, as above stated, the substrate reconstructs if the exposure is performed directly at 300 K.

After all these trials, it was not possible to find a recipe for the preparation of a perfect (2×1)p2mg. The best structure to start with (the one with least defects) turned out to be the surface in Figure 3.10, i.e. adsorption at 200 K and annealing to 260 K.

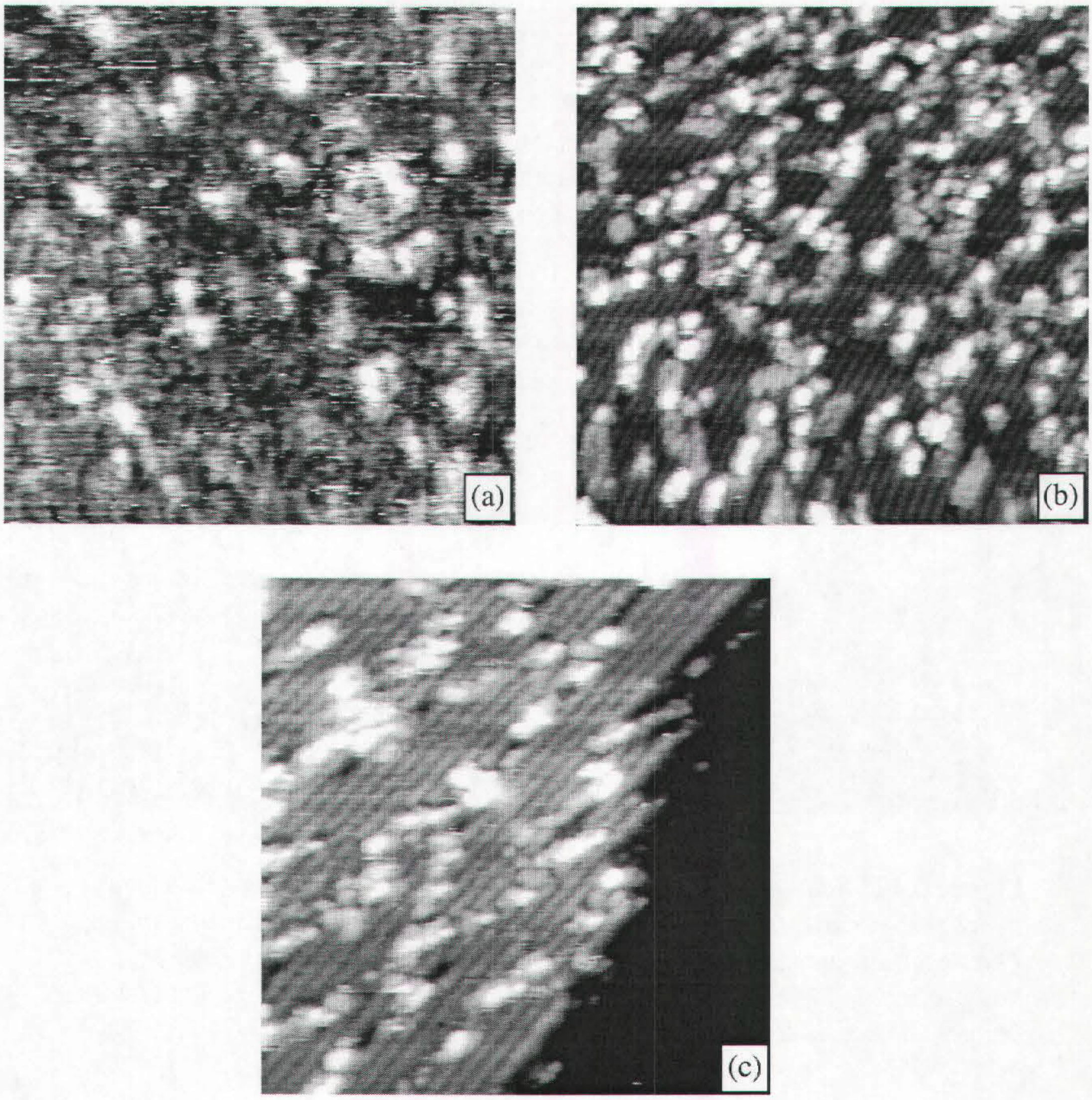

Figure 3.11: *(2×1)p2mg structure obtained by dosing oxygen at 146 K (a) and subsequently annealing to different temperatures: (b) 240 K; (c) 290 K. Size: (a) and (b) 200×200 Å^2; (c) 145×145 Å^2 ((a): I=2.00 nA, V_B=+0.38 V; (b) and (c): I=0.75 nA, V_B=+0.46 V).*

3.4.2 Nucleation of the Reaction

When the surface is exposed to molecular hydrogen at 260 K, after an induction period of about 100÷200 sec the reaction starts. The existence of an induction period indicates a difficult nucleation. This can be related either to molecular hydrogen dissociation and OH formation (which can be forbidden on flat terraces but facilitated at defects) or to the interaction between OH groups to form water.

Once the reaction sets in, it propagates on the whole surface as a wave front (see Figure 3.12). The presence of an ongoing reaction is evidenced by the formation of *paired features*, which gradually cover the whole surface.

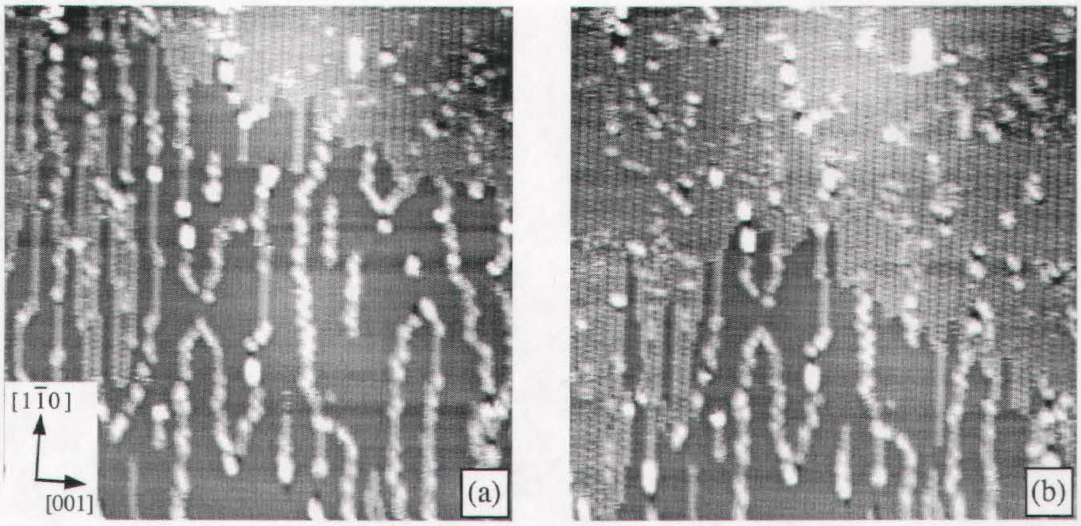

Figure 3.12: *Reaction front. (a) After exposing the (2×1)p2mg-O surface to hydrogen, a wave front appears from the upper right corner of the image. The reaction nucleates also from some chain-like defects. (b) The reaction has propagated over more then half of the investigated area. Time between images: 35 sec. Size: 500×500* $Å^2$*.* $(I=1.58\ nA,\ V_B=+0.14\ V,\ T=260\ K)$.

As shown in Figure 3.12, the reaction can also nucleate at *chain-like* defects all over the surface. Here the propagation can be studied in details: *paired features* form, aligned in chains along the close-packed $[1\bar{1}0]$ direction, with a couple-couple distance of two lattice constants. They grow in an anisotropic way, the faster propagation being the $[1\bar{1}0]$ direction; in the [001] direction the growth develops more slowly via a doubling process, as shown in Figure 3.13. *Paired features* are mainly shifted by one $[1\bar{1}0]$ lattice constant between adjacent rows but initially they are sometimes aligned along the [001] direction. In this case, in one or two images they slide in the $[1\bar{1}0]$ direction so that a well-ordered c(2×4) structure covers the whole surface.

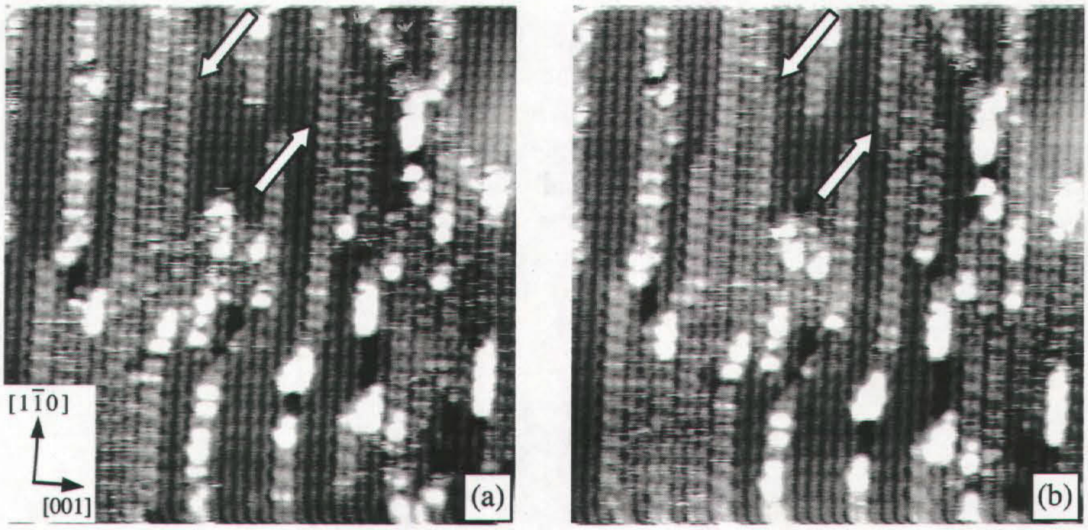

Figure 3.13: *Growth of paired features starting from chain-like defects. The rows of paired features indicated by the arrows in (a) are split in (b). The splitted rows form again paired features with adjacent (2×1)p2mg areas. Size: 200×200 Å² (I=1.02 nA, V_B=+0.13 V, T=260 K).*

3.4.3 The c(2×4) Structure

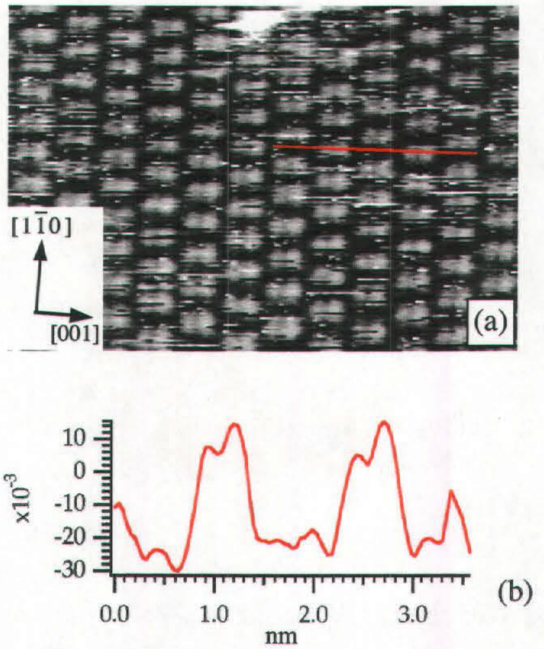

Figure 3.14: *The c(2×4). (a) Image of the structure. Size: 115×75 Å² (I=1.02 nA, V_B=+0.13 V, T=260 K). (b) Profile along the red line in (a).*

Figure 3.14(a) presents an image of the c(2×4) structure. The presence of paired features on the Rh(110) surface reminds the study in ref. [27], already described in Section 3.2, where low coverage oxygen atoms were found to arrange in pairs, even though in that case they were ordered in a (2×3) or a c(2×6) structure. The interpretation that the *paired features* in our images are oxygen as well is tempting. Their height is 0.3÷0.4 Å with an internal distance of about 2.77 Å, as shown in Figure 3.14(b), and these values are in agreement with ref. [27]. Moreover we dosed 0.6 L of O_2 at 100 K on the clean Rh(110) surface and annealed to 270 K and the structure produced in this way displays a clear c(2×4) LEED pattern. In Figure 3.15 an STM image of this structure can be found. It is doubtless the same structure that forms during the water formation reaction.

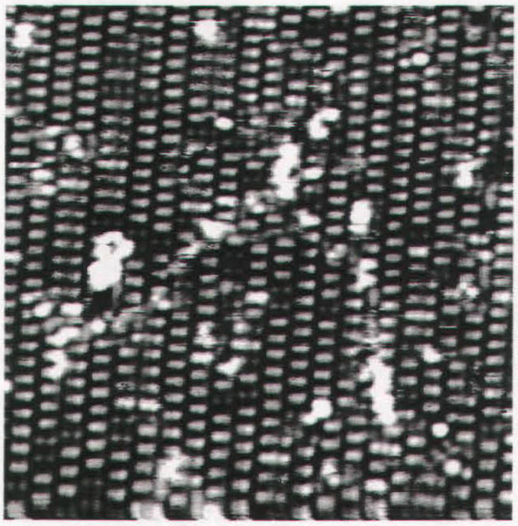

Figure 3.15: *c(2×4) structure obtained by dosing 0.6 L of O_2 below 120 K and annealing to 270 K. Size: 200×200 $Å^2$ (I=1.00 nA, V_B=+0.42 V).*

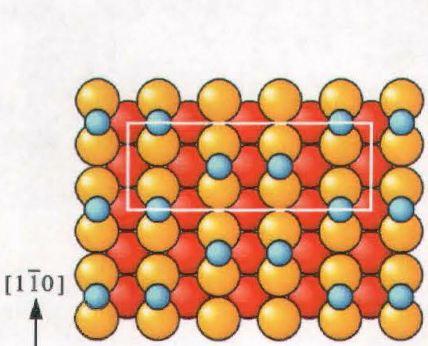

Figure 3.16: *Model of the c(2×4) structure. Yellow circles are first layer rhodium atoms while small blue circles are oxygen atoms in short-bridge sites.*

The c(2×4) structure, thus, is now identified. It is composed of oxygen atoms in short bridge sites as in the model in Figure 3.16, with an overall coverage of 0.5 ML. This means that up to this stage of the reaction, only half of the initially present oxygen atoms have been removed while the remaining atoms rearranged in the new structure.

3.4.4 The c(2×2) Structure

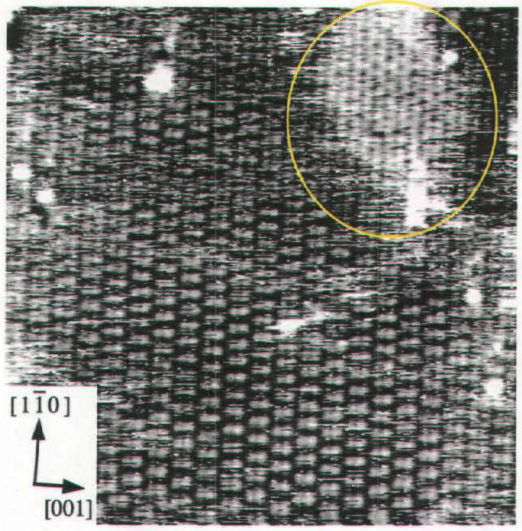

Figure 3.17: *Brighter structure formation on the c(2×4) in the highlighted area. Size: 200×200 Å^2 (I=1.02 nA, V_B=+0.13 V).*

In the upper right area of Figure 3.17 a brighter part is highlighted. Brighter areas like this one nucleate after completion of the c(2×4) structure and expand up to about half of the surface while the c(2×4) *paired features* first become disordered and then disappear. Finally the extension of brighter areas is gradually reduced, leaving a clean substrate.

We characterised the new structure (see Figure 3.18) and it turned out to have a c(2×2) symmetry, with a hexagonal arrangement of "double peak" features. The internal distance between the peaks is on average about 2.77 Å and a corrugation (between [001] adjacent features) of 0.25÷0.32 Å is measured. The units are 0.3 Å higher then *paired features* in the c(2×4) arrangement.

From the image in Figure 3.18 the registry can be inferred. In Figure 3.19(a) red lines are drawn at the position of substrate [1$\bar{1}$0] rows, based on the c(2×4) position and the model proposed in Section 3.4.3 for this structure. By referring the peak position to these lines it can be said that peaks are almost aligned with close-packed metal rows, apparently slightly tilted alternatively towards the left and the right. In Figure 3.19(b) also [001] rhodium rows are sketched. As the arrows indicate, "double peak" features sit in between the rows.

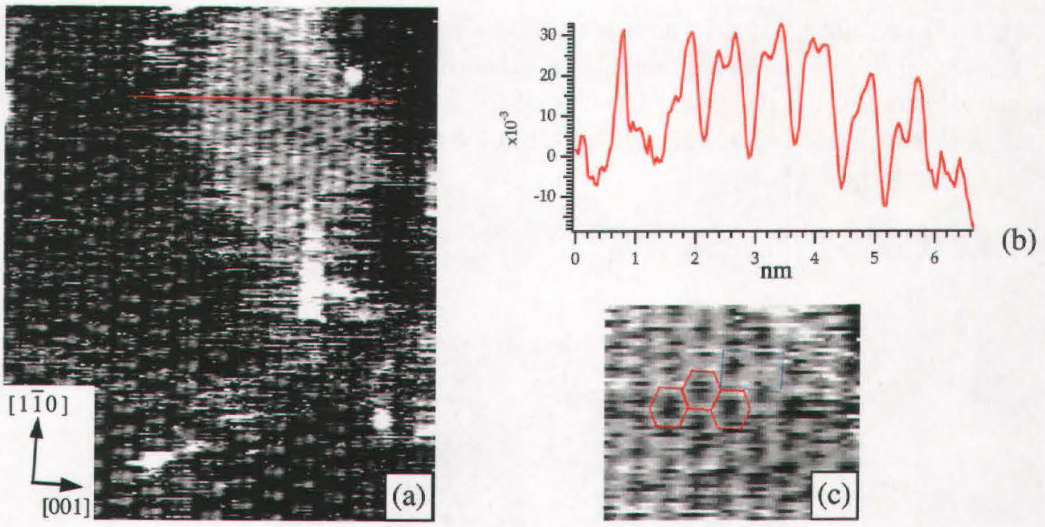

Figure 3.18: *Details of the c(2×2) structure. (a) Zoom on the structure. Size: 105×120 Å^2 (b) Profile along the red line in (a) evidencing the "double peak" character of the features. (c) Hexagonal arrangement (highlighted by red lines): a unit cell is also indicated (blue dotted lines).*

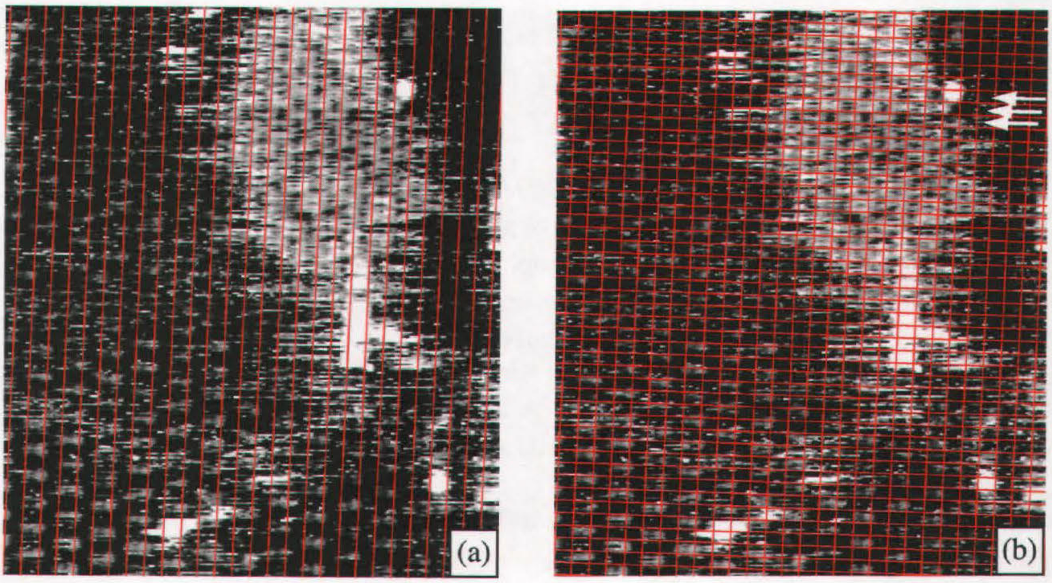

Figure 3.19: *Registry of the c(2×2) structure. (a) [1$\bar{1}$0] rows of the substrate are drawn. (b) Also [001] metal rows are indicated. Size: 105×120 Å^2.*

With the help of above exposed conclusions, a model of the structure can be proposed (Figure 3.20). We suggest that pairs are due to units in threefold sites in antiphase between adjacent [1$\bar{1}$0] rows, leading to a coverage of 1 ML.

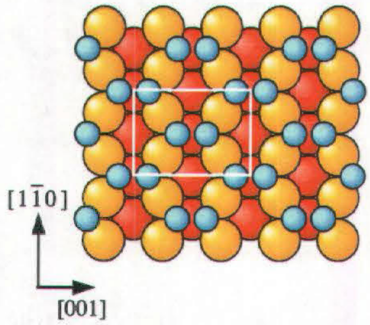

Figure 3.20: *Suggested model for the c(2×2) structure. Yellow circles are first layer metal atoms while small blue circles are the unidentified units composing the structure.*

A few different hypotheses can be made about the chemical identity of the units in the c(2×2) structure.

Oxygen and hydrogen are certainly present on the surface and reaction products (both intermediate and final) might be as well. Hydrogen is known to form four ordered structures on the unreconstructed Rh(110) surface, namely (1×3)-H, (1×2)-H, (1×3)-2H and (1×2)-2H [38], but a c(2×2) has never been reported.

A second hypothesis is that the c(2×2) is a compressed oxygen structure but such a symmetry has never been found previously. 1 ML of oxygen usually gives the (2×1)p2mg structure, where O atoms indeed adsorb in threefold sites in a zig-zag fashion but the zig-zag is in phase between adjacent [1$\bar{1}$0] rows as always happens on the Rh(110) surface when unreconstructed areas are present, i.e. also on the small terraces between missing rows in case of adsorption at higher temperatures. Thus we can not imagine why the antiphase should now be stabilised. Moreover, there are not convincing reasons why all oxygen atoms present in the c(2×4) (0.5 ML on the whole surface leads to 1 ML on a maximum area of about half of the surface, thus the total number of O atoms is more or less conserved) should be pushed towards c(2×2) areas. In fact, a compression of an oxygen overlayer due to hydrogen coadsorption was indeed found, for example, also on Pd(111) [30], but only when OH formation is not possible, while on our surface half of the initial O atoms have already been transformed to water, which indicates that OH can be easily produced.

The c(2×2) units might also be water molecules but TDS measurements, which will be presented in Section 3.5.2, exclude the presence of this species on the clean rhodium surface at the investigated temperature.

Even if coadsorption structures can not be ruled out a priori, the most probable hypothesis is that the c(2×2) is made of OH. In order to confirm this possibility, we prepared an OH layer by dosing water on the O pre-dosed surface. This experiment will be the subject of the next Section.

A definitive chemical identification will come from DFT calculations and STM images simulations, which are currently under way in the group of Werner Hofer.

3.5 Water on Oxygen pre-dosed Rh(110)

This section discusses the formation of OH as a possible intermediate product in the H_2 + (2×1)p2mg-O reaction.
After an introduction on previous results about OH formation on various metal surfaces, TDS and STM results obtained on Rh(110) in this work will be presented.

3.5.1 Water on Oxygen pre-dosed Metal Surfaces

The presence of oxygen on transition metal surfaces strongly influences water adsorption. An extensive review about water adsorption and water-oxygen interaction on solid surfaces can be found in ref. [39].
The interaction between O and H_2O can be limited to the fact that oxygen prevents the formation of a hydrogen bond network between the H_2O molecules, thus destroying a long range ordering and a preferred orientation which H_2O would assume on the clean surface. This is the case, for example, for Ru(0001) [39]. On Re(0001) the interaction is stronger and oxygen is able even to prevent water dissociation, which instead occurs on the clean surface[40].

More commonly water adsorption on an oxygen pre-dosed surface in the temperature range 130÷200 K results in an OH overlayer, via the hydrogen abstraction reaction [39]:

$$O_{ads} + H_2O_{ads} \rightarrow 2OH_{ads}$$

This happens, for example, on Ag, Cu, Ni, Pt, Pd.
In all cases where molecular dissociation takes place, it is very sensitive to the actual oxygen coverage, as illustrated in Figure 3.21 for Cu(110) [41]. This graph indicates that the dissociation of water via hydrogen abstraction is favored only at relatively low O coverages (maximum OH production for $0.13 \leq \Theta_O \leq 0.25$ ML), whereas at oxygen saturation coverages the surface becomes unreactive.

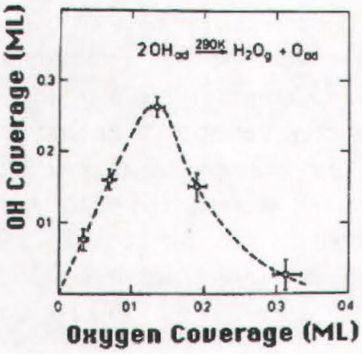

Figure 3.21: *Dependence of the hydroxyl coverage on the initial oxygen coverage on Cu(110) [41].*

The dependence of reactivity on oxygen coverage is supposed to be due to a geometrical site-blocking effect, because significant coverage-induced changes in the electronic properties of the adsorbed oxygen atoms are unlikely. Moreover, if oxygen tends to form islands at high coverages, this reduces further the surface reactivity, because the reaction occurs only at the edges of the islands.

Thermal desorption studies of H_2O on a variety of surfaces reveal common features, i.e. the H_2O - surface bond seems to be rather unspecific. When water adsorption is molecular, it desorbs completely below ~250 K in most cases. However, when water is adsorbed on oxygen pre-dosed surfaces of metals, such as Ag, Cu, Ni or Pd, where OH is formed, the TDS spectra exhibit a series of water peaks, with the highest peak temperature ranging typically from ~240 to 360 K.

It can be generalised [39] that whenever a TDS peak is seen at ~250 K or above, it is due to recombination of adsorbed OH. Molecular water is usually not retained under UHV conditions at 300 K or above.

Formation and desorption of H_2O from adsorbed OH can follow more than one reaction pathway. It might undergo the reversible disproportionation reaction:

$$2OH_{ads} \leftrightarrows H_2O_{gas} + O_{ads}$$

or it might follow the dissociation and recombination route:

$$OH_{ads} \rightarrow O_{ads} + H_{ads}$$

and then

$$H_{ads} + OH_{ads} \rightarrow H_2O_{gas}$$

or

$$2H_{ads} + O_{ads} \rightarrow H_2O_{gas}$$

Evidence for disproportionation of OH on many surfaces is based on the observation that desorption of H_2 occurs at temperatures below the desorption temperature of H_2O. This means that the reaction which produces water cannot be the recombination of adsorbed oxygen and adsorbed hydrogen, since no hydrogen remains on the surface at the time of water evolution. Further proof for disproportionation, for example on Pd(100) [42], comes from isotope exchange experiments.

In other cases, both pathways can be accessed. In TDS spectra of water from OH on Rh(100) [39], for example, disprportionation is believed to be the source of water desorption at 275 K, whereas sequential addition of hydrogen to oxygen is the source of H_2O desorption at 325 K.

Concerning the structures formed by OH produced by hydrogen abstraction, ref. [39] indicates that all identified LEED patterns represent perfect adlayers, with an OH coverage of 0.5 ML. This holds, for example, for the (1×2) and (2×1) structures on the fcc(100) and fcc(110) surfaces and the c(2×2) structure on Ag(100). TDS data often indicate a total OH coverage somewhat lower then 0.5 ML (0.2 to 0.3 ML). This is explained by the formation, often in presence of excess oxygen, of OH islands, and not saturated layers, with a local coverage of 0.5 ML, due to a net attractive interaction between neighbouring hydroxyls.

The above exposed general trend, both for oxygen coverage sensitivity of the hydrogen abstraction reaction and for OH structure and coverage, is however contradicted by more recent studies on Ag(110) [43,44]. On this surface OH formation is reported to follow water adsorption on well ordered (*n*×1)-O phases ($2 \le n \le 6$, *n* even), leading to ordered (1×*m*) structures ($m = n/2$) [43]. Thus even a (2×1)-O surface (coverage of 0.5 ML, higher than the limit coverage for OH formation proposed in ref. [39]) can give OH after water adsorption. Moreover, a (1×1)-OH phase is formed all over the surface, with an OH coverage of 1 ML (again much higher than previously reported coverages). No information is available about adsorption geometry; nevertheless a missing row substrate reconstruction is ruled out. In helium diffraction patterns, the (1×1)-OH phase (Θ_O=1 ML) is found to evolve through a sharp transition at T≈240 K, back into the initial (2×1)-O phase (Θ_O=0.5 ML). In ref. [44] OH formation starting from the (3×1)-O surface is investigated. In this case a phase mosaic structure results with domains of (1×2) and (1×1) symmetries. (1×1) patches undergo a recombination reaction in a very narrow range of temperatures around ~247 K. In Fig. 3.22 the TDS spectrum obtained from the pure (1×1)-OH phase is reproduced: it is characterized by a single, narrow desorption peak at ~252 K, indicating recombination from a single OH state.

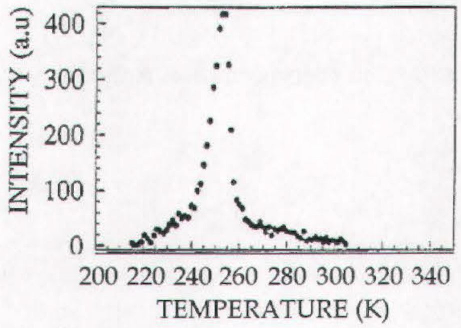

Figure 3.22: *Thermal desorption spectroscopy measurements at mass 18 obtained from recombination of the (1×1)-OH phase on Ag(110) [44].*

On rhodium, the O + H_2O interaction depends on the crystallographic surface. On Rh(111) only the bonding arrangement of adsorbed water is modified by the presence of oxygen, up to a full O monolayer which results in the formation of interfacial ice [45]. On Rh(100), conversely, hydrogen abstraction takes place [39].

3.5.2 H_2O+O on Rh(110): Thermal Desorption Spectroscopy

There is no reference on OH preparation on the Rh(110) surface.

Based on general results for water-oxygen coadsorption on metal surfaces, we dosed water up to saturation at 170 K on 0.35 L of oxygen (adsorbed at 200 K) on Rh(110), in order to produce an OH layer. Water has been dosed with a doser (described in Section 2.4.2) instead of background dosing, to maintain a low pressure in the chamber during experiments.

The oxygen exposure was chosen in order to obtain a low O coverage, where the OH formation should be at its maximum (see previous paragraph).

In Figure 3.23 TDS spectra for mass 18 both from a purely water covered surface and from the H_2O + O system are reported. The former spectrum exhibits two peaks: a main one at 215 K and a second one at ~250 K, which might be due to water formation from partially dissociated water molecules. Conversely, the H_2O + O surface presents a sharp TDS peak at 262 K and a small one at ~200 K. This picture is similar to other TDS spectra from OH covered surfaces (see previous section). In fact the main water desorption peak is shifted to higher temperatures and is as narrow as the one from the (1×1)-OH on Ag(110) [44], indicating that indeed an OH layer has been formed. The narrow shape may be seen as an evidence for the occurrence of a disproportionation reaction during desorption: the reaction takes place easily between adjacent species. The peak at lower temperatures in the TDS spectrum of the OH covered surface might be assigned to molecular water adsorbed onto oxygen free areas.

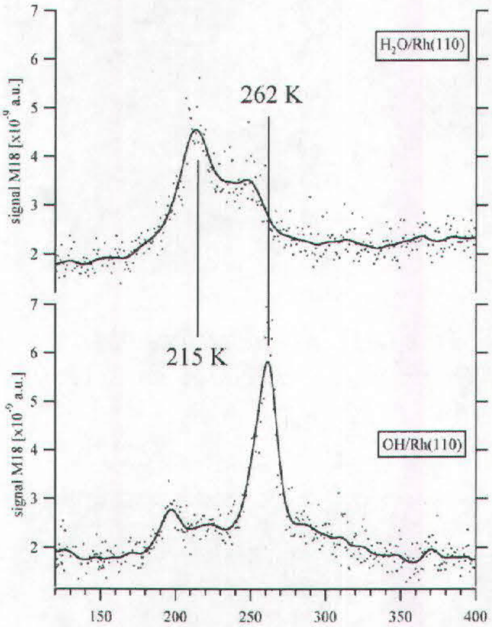

Figure 3.23: *TDS spectra from water covered Rh(110) and H_2O+O covered Rh(110).*

Also mass 2, 16, 28 and 32 were monitored (up to 700 K) together with mass 18 during the experiments. No feature was found for any of the above listed masses when heating the OH covered surface. The dissociation of molecularly adsorbed water seems therefore to be blocked on this O covered surface. Conversely, for the H_2O/Rh(110) system a hydrogen desorption peak is present at 285 K. The presence of hydrogen on this surface can be traced back to complete dehydrogenation of a small amount of water molecules. The H_2 desorption peak is only ~20 K above the H_2O desorption peak which results from the OH disproportionation on the OH layer. This indicates that around 260 K the O-H bond is weak and can be easily broken, leading to the complete dissociation of water if free adsorption sites are available.

3.5.3 H_2O+O on Rh(110): Scanning Tunneling Microscopy

We studied the H_2O+O/Rh(110) system by STM, preparing the surface as before (water up to saturation at 170 K on 0.35 L of O adsorbed at 200 K). STM images have been taken at low temperature immediately after formation and at 223 K and 273 K.

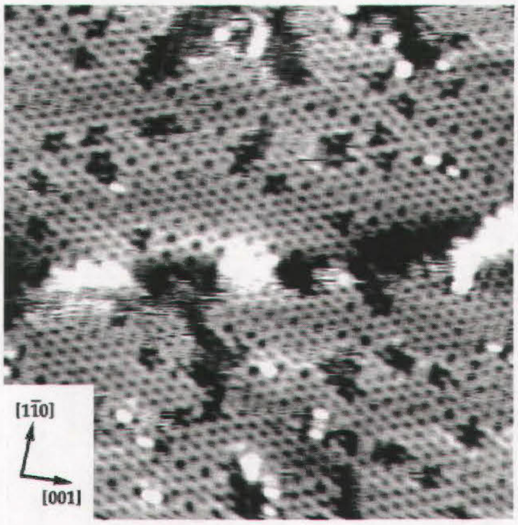

Figure 3.24: *Image of the OH covered surface obtained by dosing water at 170 K on 0.35 L of O_2 pre-dosed at 200 K on Rh(110). Size: 200×200 Å^2 (I=0.59 nA, V_B=+0.46 V, T=225 K).*

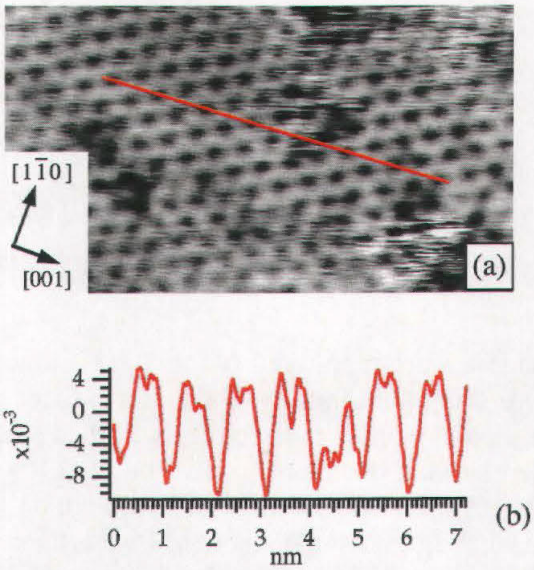

Figure 3.25: *Close-up on the c(2×2)-OH structure. (a) Size: 100×54 Å^2 (I=1.00 nA, V_B=+0.28 V, T=225 K). (b) Height profile along the line in (a), proving the "double peak" character of the units.*

The common structural feature, present at all temperatures, is shown in Figure 3.24. The structure has an hexagonal arrangement and distances which indicate a c(2×2) symmetry. The close up in Figure 3.25 shows that the units in hexagons are *double peak* features with an average internal distance of ~2.77 Å. If we interpret each protrusion as a single OH group, a coverage of 1 ML is inferred. Such a high coverage corresponds to the one found on the Ag(110) surface [43] and might be stabilised by the formation of hydrogen bonds. A hexagonal arrangement is not surprising for systems where hydrogen bonding plays an important role, see for example ref. [46] for OH on Pt(111) surface. and ref [47] for H_2O on Pd(111).

Immediately after dosing, measurements were performed at 130 K. Images are often quite fuzzy, which is a fingerprint for the presence of moving features. Nevertheless it was possible to achieve atomic resolution in images like the one in Figure 3.26. The corrugation of the structure ranges between ~0.25 and 0.35 Å.
Several domain boundaries can be seen (see arrow in Figure 3.26). They divide areas where the structure seems to be shifted from the ideal adsorption sites with random phase. There is no defined shift between different domains. Domain boundaries are generally made of a few defects, aligned along [001]. Their position changes in subsequent images, which clearly indicates that OH is mobile even at this temperature. Small depressions are also present. The structure covers the whole surface up to the steps and only rarely unknown species decorate step edges.

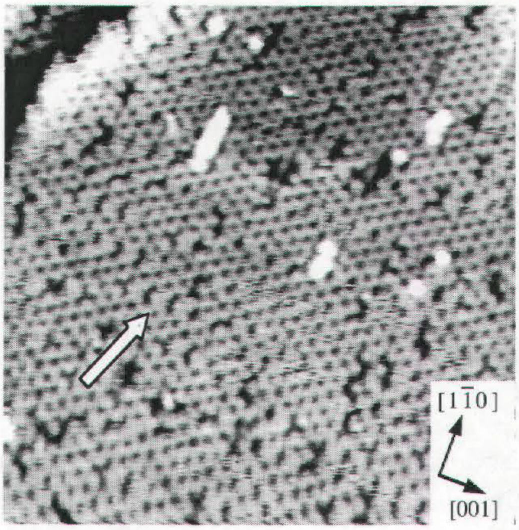

Figure 3.26: *Image of the surface at 130 K immediately after preparation. The arrow points to domain boundaries. Size: 200×200 Å^2 (I=0.29 nA, V_B=-0.15 V).*

After heating the structure to 223 K, just above the first, small, desorption peak in the TDS water spectrum, resolution in STM images improved but the corrugation is now decreased (0,1÷0.2 Å on average). This may be due to the removal of water molecules previously randomly distributed in between the OH structure or, more probably, diffusing under the tip. As indicated by arrows in Figure 3.27, domain boundaries are still present. They are now aligned along [001] as well but look different: they appear as depressions which divide areas where the structure is shifted by one lattice constant in [001], thus with same adsorption site in different domains. This homogeneity may also be viewed as another explanation for the lower corrugation with respect to the corrugation before the annealing, which is an average over different adsorption sites.

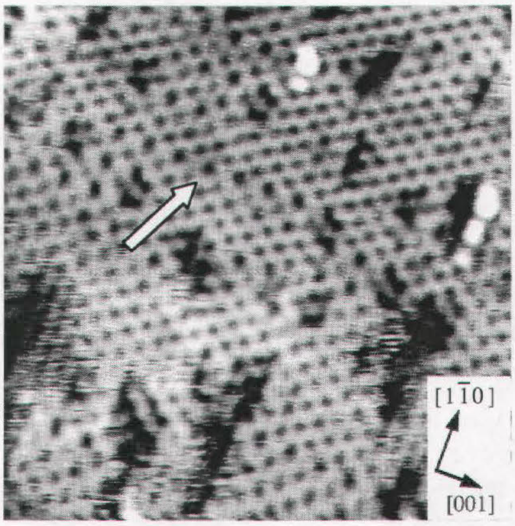

Figure 3.27: *The OH layer after annealing to 223 K. The arrow points to a domain boundary. Size: 150×150 Å^2 (I=1.00 nA, V_B=+0.12 V).*

OH free patches, 0.4 Å lower than the hexagons, are now also present (see for example lower left part of Figure 3.27 or upper part of Figure 3.24). Here the close packed [1$\bar{1}$0] rows are visible. These small patches might be covered by hydrogen, originating from the background or from water dissociation. Hydrogen desorbs at higher temperatures (~280 K) [38] and is not easily imaged by STM. A fuzzy aspect inside the OH free patches and at their borders is in agreement with this speculation.

For the completeness of this description, the presence of further defects (not seen in figures) on the surface has to be reported. Defects are randomly present, mainly single holes and triangular areas where the protrusions are lower, which have not been identified. Step edges sometimes display a brighter appearance with a local (1×1) symmetry. Actually areas close to steps often show darker stains, due to the presence of unknown species.

In conclusion the main effect of this first annealing is a rearrangement leading to a more homogeneous surface and an improvement of the image quality, probably due to desorption of diffusing water.

Finally a further increase in the temperature, this time up to 273 K, thus above the main desorption peak in the TDS spectrum, results in formation of a clean surface. This finding is surprising at first sight, because oxygen is expected to remain on the surface after disproportionation. Nevertheless reaction of this small amount of adsorbed O atoms with background hydrogen or carbon monoxide, during the time passing between temperature stabilisation and reestablishment of STM imaging conditions (~20 min), can explain experimental results. Already the first image taken of the clean surface reveals the presence of CO molecules.

3.6 Back to the Catalytic Oxidation of Hydrogen

Based on the above experiment, we can now try to identify the second intermediate structure produced during the water formation reaction as OH.

Comparison with the OH covered surface indicates that the STM images of the two structures are very similar. First of all a hexagonal arrangement is present in both cases and a measurement of the distances gives a c(2×2) symmetry, in agreement with the model proposed in Section 3.4.3.

Moreover both structures are composed of "double peak" features with an internal distance of ≈2.77 Å on average.

The corrugation inferred from reaction images is perfectly in agreement with the corrugation of the OH layer immediately after dosing, when a small amount of water is still present. The momentary presence of water molecules on the surface or under the tip is highly probable also in the reaction measurements.

We can hence identify the second intermediate structure in the water formation process as due to OH groups.

It is possible at this point to depict a reasonable scenario for the second part of the reaction.

It involves the nucleation of OH areas mainly in proximity of surface defects, which act as nucleation centres. Oxygen atoms diffuse from the c(2×4) structure towards hydroxyl regions and react with atomic hydrogen at their borders. The latter statement is inferred based on the observation that OH islands are surrounded by a region where diffusing species, whose height corresponds to oxygen in the c(2×4), are resolved. Moreover in these areas *paired features* are sometimes clearly imaged at random positions.

Thus OH islands grow until all oxygen is consumed.

The reaction temperature corresponds exactly to the water desorption peak in the OH overlayer TDS measurement. Therefore there is an equilibrium between growth, due to oxygen supply, and loss, due to water desorption. It has to be considered that every desorbing water molecule produced by disproportionation leaves back one O atom which can again react with hydrogen. While enough O atoms are on the surface, the rate of OH formation is higher than the desorption rate and staedy-state islands form. Conversely, after all oxygen has been converted to OH, only desorption takes place. It seems that water forms, or at least desorbs, from the borders of the islands, leading to the decrease in their size. This interpretation explains also the fuzzy appearance of island edges, which is characteristic of diffusing water molecules. Moreover this "noise" in the images increases after oxygen has been consumed (i.e. when the water production rate exceeds the OH formation rate), but is no more present when the reaction terminates.

At the end a clean surface is produced, with randomly distributed defects (one layer deep holes and single metal atoms jumped above the top-most layer), which were already present on the initial surface. It has to be noted that at the investigated temperature hydrogen can still be bound to the surface (see ref. [38]), so a certain amount of adsorbed H atoms is probably present on the final surface, even though they are not resolved by STM.

3.7 Comparison with Global Reactivity Measurements

The water formation reaction starting from the (2×1)p2mg-O surface was investigated by global reactivity measurements in a previous study [48]. At t=0 hydrogen was introduced with pressure of 9×10^{-8} mbar and water production was monitored by a mass spectrometer placed in front of the sample during hydrogen exposure at various temperatures.
The experiment was performed at temperatures from 275 K to 375 K at steps of 25 K, i.e. higher temperatures than in our case but from a qualitative point of view the behaviour seems to be the same at all investigated temperatures. Moreover the lowest T considered in that study (275 K) is close enough to the one used in our STM study. As a consequence, a comparison between the two works can merge macroscopic and microscopic information about the reaction.

First of all, as shown in Figure 3.28(a), an induction period was found in global reactivity measurements. STM results show unambiguously that this induction can be traced back to the nucleation of the reaction at active sites. Figure 3.28(b) shows the reactivity as a function of the remaining O coverage (obtained by integrating the water production rate and subtracting this value from the initial coverage). There is an increase in the production rate up to 0.5 ML. Then the rate decreases. The initial increase can be related to the propagation of the reaction front, which gradually transforms the dense (2×1)p2mg in the c(2×4) structure, thus opening free space for further hydrogen adsorption and dissociation. The maximum production for 0.5 ML of remaining oxygen corresponds to the moment when the whole surface is covered by the c(2×4).
In the global reactivity experiments also a surface with an initial O coverage of 0.5 ML was investigated. From the preparation conditions described in ref. [48], we infer a starting structure of c(2×4) symmetry. For this structure no induction time was found. This is consistent with the idea that hydrogen can adsorb and dissociate everywhere on this less dense structure and that the reaction can therefore start immediately all over the surface without the need for nucleation centres.
The subsequent decrease in the water production rate corresponds to the formation and the subsequent decay of stable OH islands.
A final observation concerns the symmetric aspect of the curves in Figure 3.28(a): time needed for the removal of a first half of oxygen corresponds to the time needed for completion of the reaction. This is in agreement with STM observations that the number of images required for the formation of a c(2×4) layer in the image series (~22 images with 35 sec/image) is almost equal to the time required for producing a clean surface (~23 images).

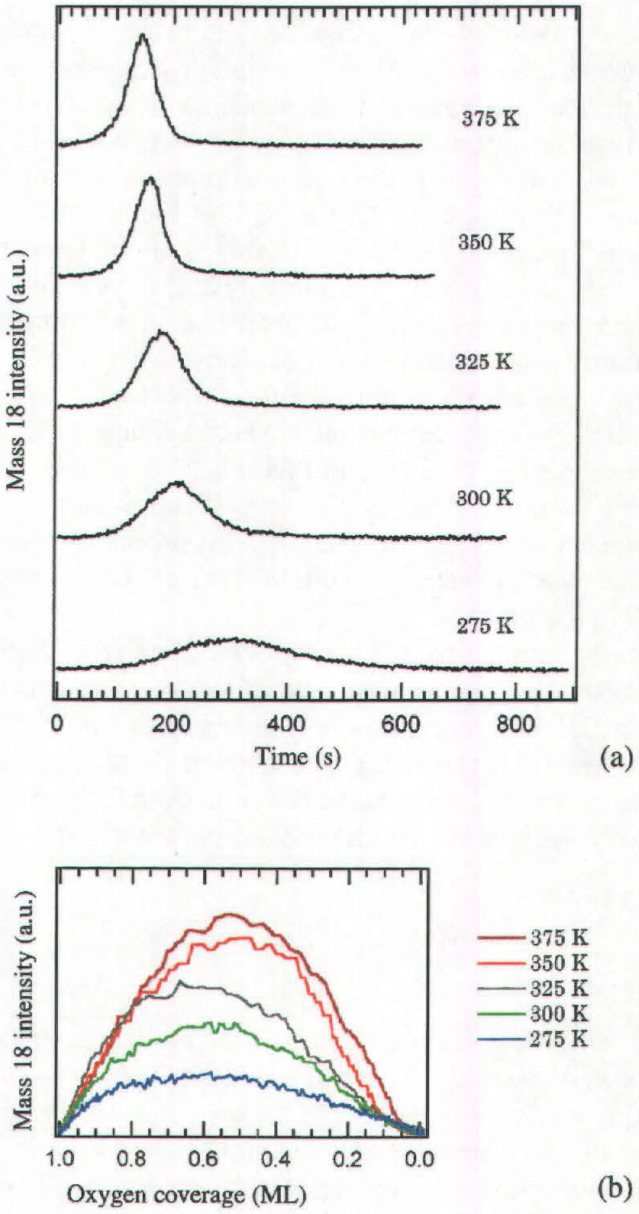

Figure 3.28: *Water formation on the (2×1)p2mg-O/Rh(110) surface at different temperatures: global reactivity measurements. H_2 valve opened at t=0 with pressure of 9×10^{-8} mbar (a) Water production as a function of time. (b) Reactivity as a function of remaining oxygen coverage [48].*

3.8 Conclusions

The unreconstructed Rh(110) surface is the simplest model catalyst studied in this thesis work. Catalytic oxidation of hydrogen has been investigated by taking series of STM images during hydrogen exposure at 260 K.

The initial surface is covered with 1 ML of oxygen in the (2×1)p2mg structure, which is characterised by O atoms adsorbed in threefold sites in a zig-zag fashion. It has not been possible to prepare a perfect structure due to the tendency of the substrate to reconstruct upon annealing. The best result is the surface in Figure 3.29(a). When the sample is exposed to molecular hydrogen from the gas phase, after a short induction time a reaction front propagates (see Figure 3.29(b and c)), removing half of the initial O coverage. The reaction nucleates also at *chain-like* defects randomly distributed on the terraces. The nature of these *chain-like* defects was not understood. When locally half oxygen atoms are reacted off, the others immediately form *paired features* which order in a c(2×4) structure. The c(2×4), which is composed of O atoms in short bridge sites, expands on the whole surface, leading to an overall oxygen coverage of 0.5 ML (Figure 3.29(d)).
When the surface is already almost completely covered by the c(2×4), brighter areas nucleate in proximity of surface defects (see arrows in Figure 3.29(d)). These areas were identified as OH islands. The identification was inferred by comparison with a surface where water was dosed over a low coverage of oxygen on Rh(110). This procedure results in the formation of an OH overlayer, which was characterised both by Thermal Desorption Spectroscopy and by Scanning Tunneling Microscopy.
OH islands grow at the expense of the c(2×4) structure (see Figure 3.29(e)). Hydroxyl islands are surrounded by disordered areas, where diffusion of paired oxygen from the c(2×4) towards the borders of OH areas occurs. Here O atoms react with hydrogen. The OH islands reach a maximum extension corresponding to about half of the surface (Figure 3.29(f)). Afterwards the islands contract, due to water desorption from their borders (Figure 3.29(g)).
Finally a clean (or partly hydrogen covered) rhodium surface is restored (Figure 3.29(h)).

Figure 3.29: *Overview of the complete catalytic oxidation of hydrogen at 260 K* ($p_{H_2}=5\times10^{-9}$ *mbar*). *(a) Starting surface: (2×1)p2mg-O/Rh(110). The arrow points to a chain-like defect. (b) A wave front appears from the upper right corner of the image but the reaction nucleates also at chain-like defects. (c) The reaction front propagates, incorporating the small nuclei at chain-like defects in (b). (d) The c(2×4)-O structure covers the whole surface. Arrows point to OH islands. (e) The c(2×2) islands grow at the expense of the c(2×4). (f) A maximum extension for the c(2×2) is achieved. (g) OH island size decreases. (h) A clean rhodium surface is restored.*
Time between (a) and (b): 10 min 30 sec; between (b) and (c): 35 sec; between (c) and (d): 105 sec; between (d) and (e): 70 sec; between (e) and (f): 70 sec; between (f) and (g): 105 sec; between (g) and (h): 10 min 30 sec. Size: 500×500 *Å²*. ($I=1.58$ *nA*, $V_B=+0.14$ *V*).

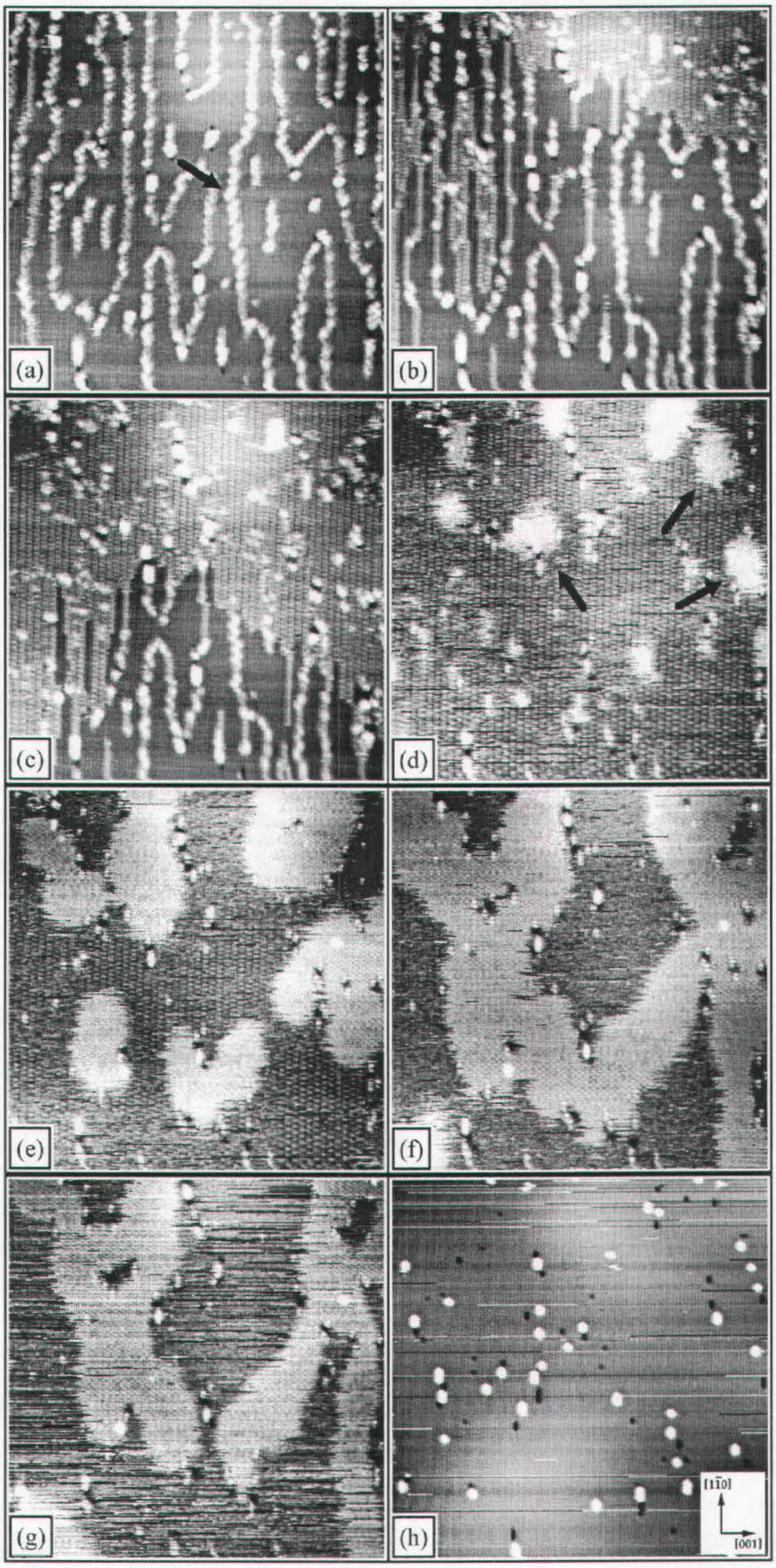
(a)
(b)
(c)
(d)
(e)
(f)
(g)
(h)
[1$\bar{1}$0]
[001]

Chapter 4

Reactivity of a Strained, Segmented Surface: (10×2) -O/Rh(110)

4.1 Introduction

High coverage, compressed oxygen structures, which often form on transition metal surfaces, can be regarded as the link between adsorbate systems and oxide phases. The study of their reactivity is therefore important for the understanding of the catalytic activity of oxidic surfaces. The interest can be traced back to the fundamental role played by oxides in catalysis even in those cases where the catalytic properties were previously attributed to the metal surface [49].

On Rh(110) a new oxide-like metastable structure with (10×2) periodicity has recently been characterised by x-ray photoelectron spectroscopy (XPS) and scanning tunnelling microscopy [21]. In this structure, which grows on the (1×2) reconstructed substrate, the high oxygen coverage induces strain along the close packed metal rows, so that some rhodium atoms are ejected. Therefore the surface is segmented.

The characteristics of the (10×2)-O structure are thus ideal for exploring the effects of nanostructures in form of segmentations on reactivity. At the same time it is a suitable system for studying the influence of strain, which has been proved, both from the theoretical and the experimental point of view [50,51], to have a strong influence on the reactivity of a surface.

Hence this oxide-like, strained, segmented reconstruction of the surface makes the (10×2)-O covered Rh(110) a first step towards more complicated (and thus more real) catalysts.

4.2 Strained Surfaces

On single-crystal metal surfaces, strain is mainly realised by evaporation of one metal onto another [52], where strain arises due to differences in the lattice constants. On such a surface, though, electronic effects due to the presence of different elements cannot be ruled out when analysing surface reactivity.

Nevertheless Gsell *et al.* found a different method for producing strain [51]. They obtained strained surface areas on Ru(0001) by means of subsurface gas bubbles induced by Ar^+ ion sputtering followed by annealing at moderate temperatures (~1000 K). With this procedure the sputter damage in the first surface layer is completely healed out but subsurface cavities are formed, filled with argon atoms which have aggregated by bulk diffusion. On the surface an expanded lattice results on top of the cavities, surrounded by a ring where the lattice is compressed relative to the flat surface (see Figure 4.1(a)).

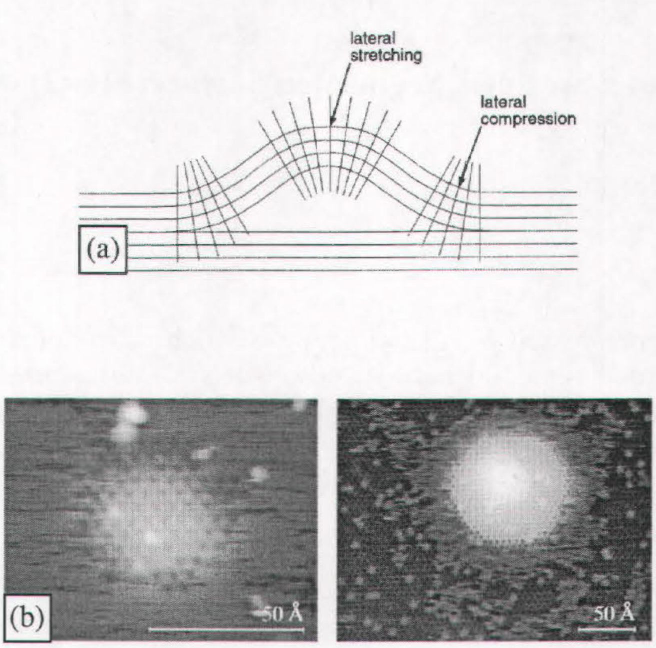

Figure 4.1: *Oxygen adsorption on the strained Ru(0001) surface. (a) Schematic cross-sectional view of an Ar subsurface bubble. The topmost layer is stretched above the bubble and compressed at the edges of the protrusion. (b) STM images of oxygen adsorption. A (2×2) structure has already formed on the stretched area for an overall coverage of 0.02 ML (image on the left) and has expanded to the whole surface except the rim where the lattice is compressed for an overall coverage of 0.2 ML (image on the right) [51].*

On this substrate adsorption is strongly influenced by strain. As shown in Figure 4.1(b), for an overall low coverage of oxygen, adsorbed atoms mainly sit on top of the bubble, where the surface is stretched, leading to the formation of a local (2×2) structure while other areas of the surface are clean. When the coverage is increased up to ~0.2 ML almost all the surface is covered by oxygen in the (2×2) structure, with the exception of a depletion zone corresponding to the rim where the substrate is compressed. The same trend, formation first on top of the bubble, then on flat terraces and finally also on the rim, holds for higher coverage structures, i.e. (2x1)-O, (2×2)-3O and (1×1)-O. Hence it can be concluded that stretched areas are preferred for oxygen adsorption, while compressed areas are the least favourable. A similar behaviour was found for CO at coverages above 0.33 ML [53].
These experimental observations have been explained by DFT calculations [50]. In Figure 4.2(a and b) binding energies are plotted as a function of the relative change in surface lattice constant of Ru(0001). Both atomic oxygen and CO are indeed more tightly bound on the expanded substrate and less tightly on the compressed surface. Moreover, in the same work also the CO dissociation barrier was investigated and again strain was found to have a strong influence (Figure 4.2(c)): it is easier to dissociate CO on the stretched surface.

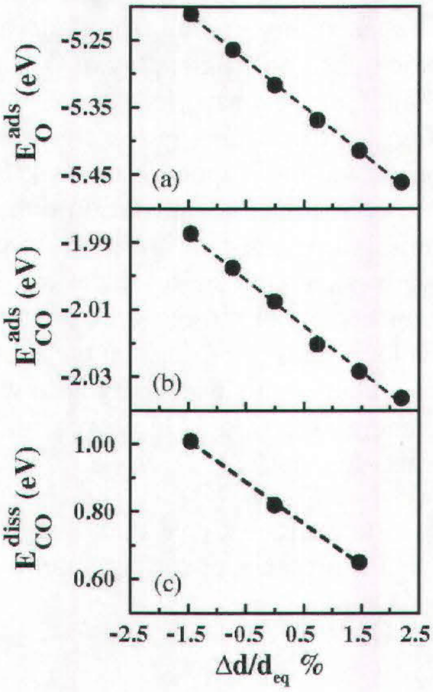

Figure 4.2: *Effect of relative change in surface lattice constant of a Ru(0001) surface on the (a) binding energy of atomic oxygen, (b) binding energy of molecular CO and (c) CO dissociation barrier, referenced to a zero of the clean surface plus a gas phase CO molecule [50].*

All these effects can be interpreted in terms of a shift in the centre of the metal *d* band with strain. When a surface undergoes compressive or tensile strain, the overlap of metal *d* states at neighbouring sites will either increase or decrease and so will the *d* bandwidths. No charging or decharging of the *d* states of late transition metal sites follow from a change in *d* bandwidth. Rather, the *d* bands move in energy to maintain a constant filling. Compressive or tensile strain therefore leads to downshifts or upshifts of the *d* band centres, respectively [50,2].

The strain effect is not limited to oxygen and CO on ruthenium. Also in calculations of the activation energy for N_2 dissociation on hexagonally close-packed iron surfaces with different lattice constants, for example, it was found that large lattice constants with high-lying *d* states are the most reactive [2].

Another example is the activation energy for dehydrogenation of ethylene and of ethyl on different palladium overlayers [52]. Palladium on gold is more reactive than pure palladium because the gold lattice constant is larger than the palladium lattice constant, leading to tensile strain on the Pd overlayer. The opposite occurs on ruthenium, where Pd overlayers suffer a compressive strain. Finally the palladium/rhenium system is a case where the change in reactivity does not depend on the lattice constant but on the interaction between the electrons in the palladium overlayer and the rhenium atoms underneath. Even for Pd/Re, though, the shift in the energy of the *d* metal band follows the trend that a downshift in the position of the *d* band correlates with an increase in activation energy.

On Cu(111), expansive strain parallel to the surface plane has been proved, from the theoretical point of view, to enhance the binding of atomic and molecular oxygen on the surface as well as to decrease the transition state energy of O_2 dissociation and again the trend is traced back to a shift in the centre of the *d* band [54].
Nevertheless, this generalisation for the change in reactivity with surface strain is no more valid for hydrogen adsorption on various copper surfaces [55]. Depending on the surface orientation and the adsorption site, hydrogen atomic adsorption energies increase, decrease or remain constant when the lateral lattice constant is varied. In particular on Cu(100), atomic hydrogen adsorption becomes weaker and the dissociation barrier is higher upon lattice expansion. An analysis of the underlying electronic structure reveals that the *d* band model is no longer appropriate when the local density of states at the substrate is strongly perturbed by the presence of the adsorbate, which occurs especially at low-coordinated adsorption sites. Atomic hydrogen adsorption energies on Cu(111) do not follow the previously discussed trend, conversely observed for oxygen on Cu(111), as well.

Regardless the actual explanation, all the above studies show that the reactivity of a metal surface is strongly influenced by the presence of surface strain.

4.3 (10×2)-O on Rh(110)

A stronger binding energy is predicted also for oxygen adsorbed on an expanded Rh(110) surface on the basis of DFT calculations [56] (see Figure 4.3). Such a structure exists and will be studied in detail in this chapter. The structure is the (10×2)-O, where oxygen induces the strain of the rhodium atoms to which it is bound [21].

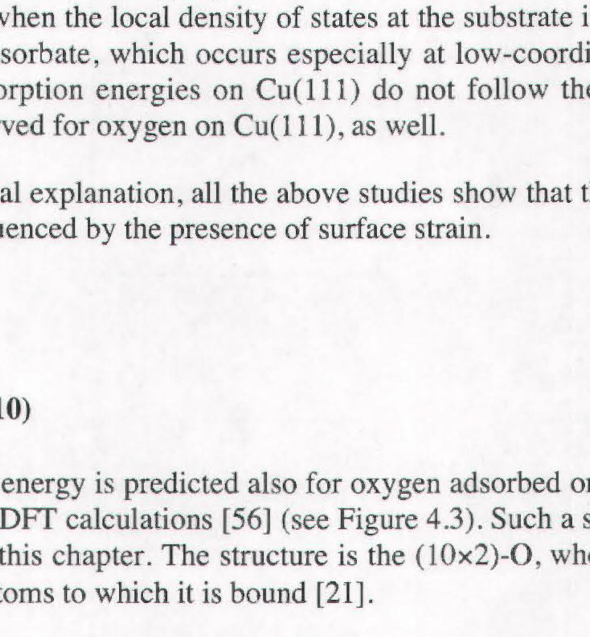

Figure 4.3: *Oxygen binding energy on Rh(110) as a function of surface strain [56].*

4.3.1 Description of the Structure

The (10×2) grows on a (1×2) reconstructed substrate when further oxygen is dosed on the (2×2)p2mg structure, which has been described in Section 3.2.
The structure is metastable and is formed when dosing at temperatures between 400 K and 600 K or when dosing at low temperature and subsequently annealing the surface.
In Figure 4.4(a) an STM image of the (10×2)-O surface is shown. It is characterised by a quite regular segmentation of the close-packed $[1\bar{1}0]$ metal rows, with segment ends almost aligned in the [001] direction, and by the presence of small, unreconstructed areas. In Figure 4.4(b) a zoom on the segments is presented. Each segment is composed of, on average, eight protrusions, with an internal distance 1/9 larger than the lattice constant, i.e. 3.0 Å instead of 2.7 Å (see Figure 4.4(c)). According to the model in Figure 4.5, each protrusion represents a single rhodium atom and therefore the internal distance between adjacent protrusions is a measure of surface strain. Oxygen atoms are bound symmetrically on both sides of the segments in threefold sites which, due to the strain, become more and more distorted towards the ends of the segments.

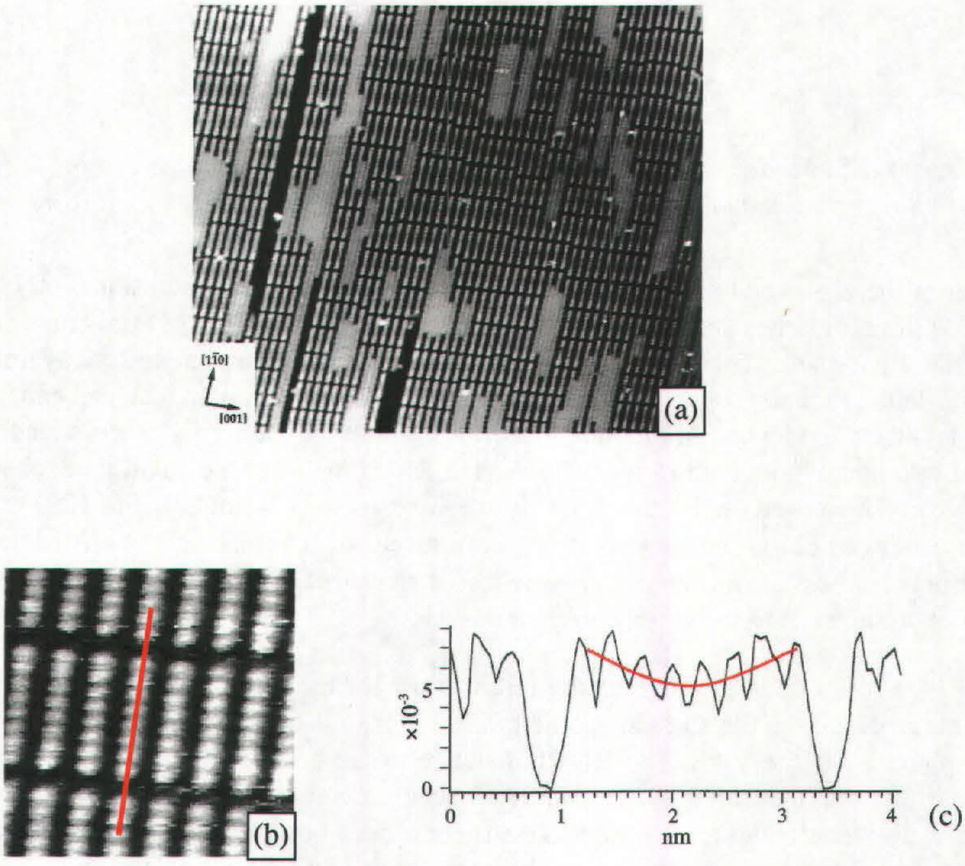

Figure 4.4: *(10×2)-O/Rh(110). (a) STM image of the surface. Size: 400×300 Å^2. (I=1.00 nA, V_B=+0.60 V) (b) Zoom on the segments. Size: 53×53 Å^2. (c) Height profile along the line in (b).*

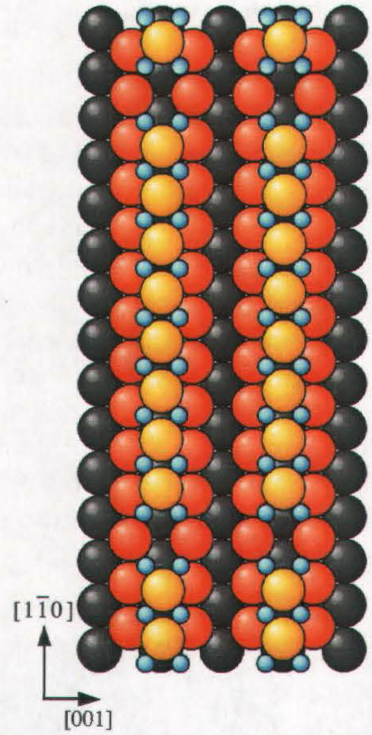

Figure 4.5: *Model of the (10x2)-O/Rh(110). Yellow circles are strained, first layer rhodium atoms. Small blue circles are oxygen atoms.*

Starting from the zig-zag O arrangement in the (2×2)p2mg structure, additional oxygen can bind to free threefold sites on the unstrained substrate. The high local O coverage induces stress in the close-packed metal rows, so that rhodium atoms are moved away form the hollow site and gradually raised towards long bridge sites. A raising at the ends of the segments is indeed evidenced in the height profile in Figure 4.4(c). This process leads to the ejection of two metal atoms out of ten. The ejected Rh atoms form the small unreconstructed islands already observed in Figure 4.4(a), where oxygen is bound in the (2×1)p2mg-O structure. The (10×2)-O surface is thus composed of coexisting reconstructed and unreconstructed areas, an intrinsic consequence of the preparation of a surface where the formation of strain leads to the expulsion of atoms.

The (10×2) could be interpreted as the initial stage for the formation of a RhO_2 layer on the metal surface. In fact, the surface geometry is similar to the one obtained by cutting along the (010) plane a RhO_2 crystal. The Rh-Rh distance in the bulk-truncated oxide (3.09 Å) is very close to the one measured in the (10×2) and each metal atom is doubly coordinated to oxygen as well. Nevertheless, the oxide-like structure does not grow three-dimensionally on the surface and is easily converted into the more stable c(2×8) when the temperature is increased above 700 K.

The (10×2)-O/Rh(110) surface has been previously characterised also by X-Ray Photoelectron Spectroscopy (XPS) [21]. Two O1*s* peaks were detected: a main one at 529.75 eV and a second one at 530.25 eV. The latter energy corresponds to the usual peak position for oxygen atoms in the zig-zag *fcc*-threefold sites along the $[1\bar{1}0]$ close-packed rhodium rows and can thus be traced back to the unreconstructed areas of the surface, which are covered by the (2×1)p2mg structure. For this type of oxygen, a coverage of 0.1 ML was inferred. The peak at lower binding energy, conversely, has to be attributed to oxygen atoms in the segmented areas and gives a coverage of 0.7 ML, which is slightly lower than what predicted by the model (0.9 ML), if oxygen is placed also in distorted threefold sites at the ends of the segments. Nevertheless those four O atoms were found to optimise the total chemisorption energy [56] and their presence will be crucial in the following. The disagreement between the measured coverage and the one inferred from the model is probably related to experimental uncertainty (diffraction effects).

4.3.2 Preparation of the Structure

The rhodium crystal has been prepared by sputtering with Ar^+ ions (3 min, 1 keV) and annealing to 1200 K. The annealing temperature was chosen to be high enough to dissolve subsurface argon bubbles (see Section 4.2), which are easily produced at lower temperatures also in the rhodium sample. Then the surface has been further treated by cycles of oxidation and reduction at 770 K: for the first two cycles, 3 L of oxygen followed by 5.4 L of hydrogen were dosed, then the sample was exposed to 1 L of O_2 and 1.4 L of H_2 for three times.

The following step is the formation of the (2×2)p2mg-O. The preparation was already optimised in ref. [14] and consists of dosing 1 L of oxygen at 770 K and subsequently flashing the sample to 960 K. Starting from this surface several procedures for production of the (10×2) were checked by LEED and the more defined pattern (see Figure 4.6) turned out to be the one obtained after dosing 29 L of oxygen at 200 K and flashing to 530 K.

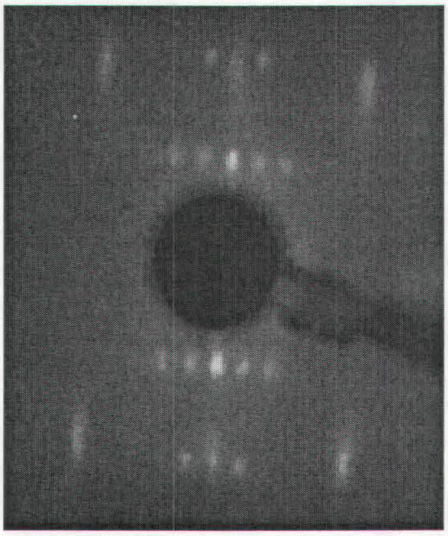

Figure 4.6: *LEED pattern of the best (10×2)-O structure. (E=61 eV, T=242 K).*

4.4 Catalytic Oxidation of Hydrogen: a Two-step Reaction

In this thesis work the reactivity of the (10×2)-O/Rh(110) surface towards hydrogen has been investigated by STM. DFT calculations have been performed by Wei-Xue Li and Biørk Hammer, from Aarhus University in Denmark, in close collaboration with our group.
Series of STM images of the surface were acquired during the catalytic oxidation of hydrogen in the temperature range 230÷300 K. Molecular hydrogen was let in with a pressure on the surface of 1×10^{-8} mbar (corrected for the tip screening factor of 5, as estimated in [37]). STM movies were recorded with acquisition times ranging between 18 (in case of small scale images) and 162 (for large scale images) seconds per image, with typical scanning parameters of +0.25÷0.9 V and 0.4÷1 nA.

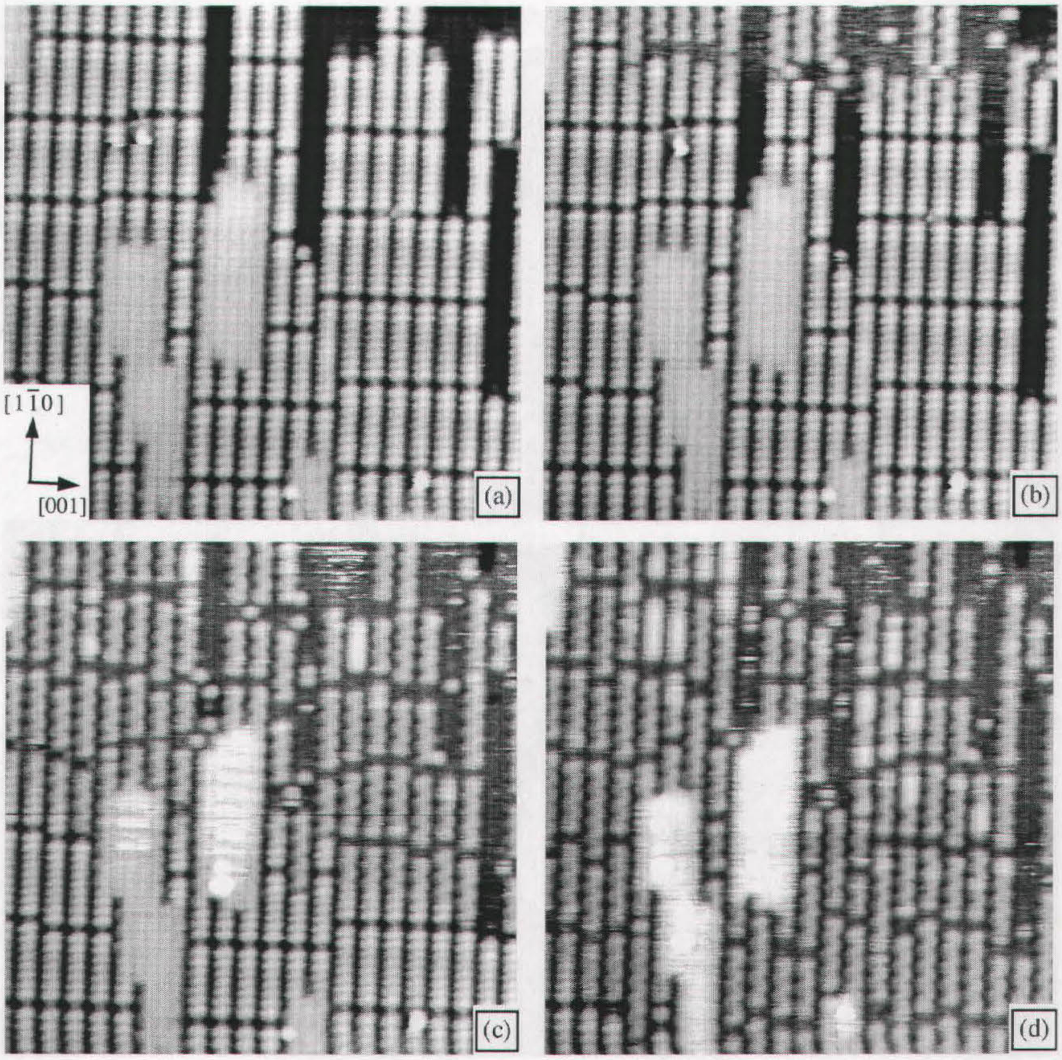

Figure 4.7: *First reaction step. (a) Initial surface. (b) After exposing the (10×2)-O surface to hydrogen, a wave front appears from the top-right area of the image. (c) The reaction has propagated to more then half of the investigated area. (d) The whole imaged area has been involved in the reaction. Remaining O atoms in zig-zag threefold sites are clearly visible. Size: 200 × 200 Å^2. Time between subsequent images: 35 sec. (I=0.86 nA, V_B=+0.53 V, RT).*

4.4.1 The First Reaction Step

Figure 4.7 presents a sequence of images extracted from an STM movie recorded at room temperature. After achieving atomic resolution and stabilising the tip, we selected the surface area in Figure 4.7(a) and started hydrogen exposure. After a short induction period, a reaction front propagates over the surface (Figure 4.7(b-d)), crossing the whole imaged area in 3 images (with 35 s/image). The reaction front alters the order of the segment structure: their length is irregularly varied and, as a result, the ends of the segments are no more aligned (see Figure 4.7(d)). Moreover, the segment separations are enlarged. This is a direct indication that the strain has been removed. Indeed, the measured Rh-Rh distance along the segments in the $[1\bar{1}0]$ direction is now multiple of the lattice constant. In Figure 4.8 a line profile across a segment separation on an unreacted area is compared to a line profile across the separation between two segments which have already reacted.

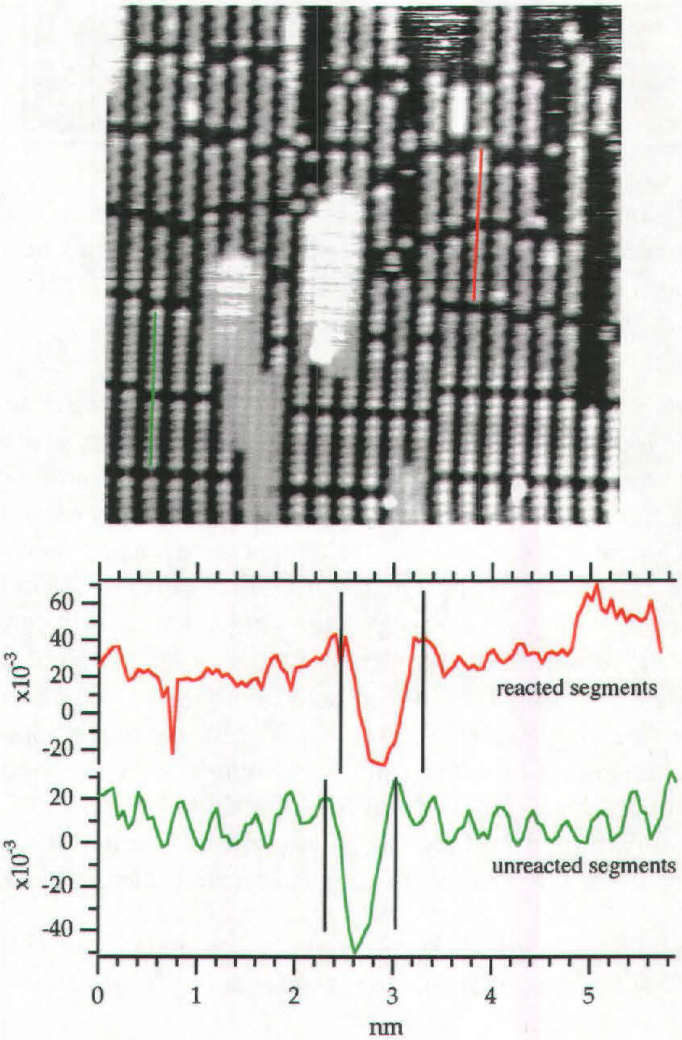

Figure 4.8: *Strain removal during the first reaction step. Height profiles along the lines indicated in the STM image. The green profile shows the distance between adjacent strained (10×2) segments ahead the reaction front. The red line crosses the separation between two (2×2)p2mg segments behind the front.*

As the sequence in Figure 4.7 shows, the reacted segments appear zig-zagged in the STM images. This is a fingerprint of the presence of oxygen atoms in threefold sites in a zig-zag configuration, as in the (2×2)p2mg-O structure (see Section 3.2). This means that in this first reaction step only half of the oxygen initially adsorbed on the surface has been removed, while a second half is still present.

Sequences of STM images allow us to deduce even the fine details of the reaction mechanism. As it can be clearly seen in Figure 4.9, the reaction proceeds along each segment, removing, sequentially, one oxygen for each couple, starting from one end of the segment towards the other.

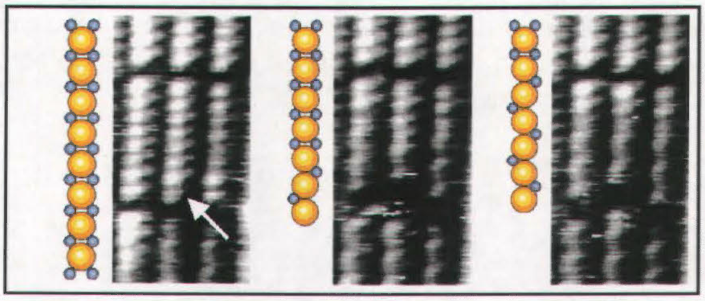

Figure 4.9: *Details of the first reaction step. The reaction propagates (from the bottom up) along a single segment (marked by the arrow) subsequently removing one oxygen atom per couple. Size: 30×60 Å^2. Time between images: 35 sec. (I=0.86 nA, V_B=+0.25 V).*

As already observed, the passage of the reaction front removes the surface strain. This proves that the strain is indeed due to the high local oxygen coverage, as previously supposed [21]. Strain release involves movement of the Rh atoms, which not always return to their equilibrium position but often jump to neighbouring sites, generating the observed misalignment of the segments. In the investigated temperature range, this is the only observed movement of the substrate atoms. This transient mobility must therefore be related to the combination of reaction energy, elastic energy - the strained segments can be considered as extended springs that relax upon removal of the additional oxygen - and of thermal energy. At RT, transient mobility of Rh atoms is observed both along the $[1\bar{1}0]$ close packed direction and the [001] direction (see single atoms in Figure 4.8); furthermore, Rh atoms can also jump above the unreconstructed areas of the substrate. If the temperature is lowered, the movement is gradually frozen and at 253 K most of the Rh atoms simply return to their equilibrium position, thus on the unstrained surface the alignment between the segments is almost retained. The difference in the order of the unstrained surface is clearly visible in Figure 4.10.

As will be described in the following sections, the reaction nucleates at terminations of the segmented structure where oxygen is removed always starting from one end of the segments, never in the middle from the side.

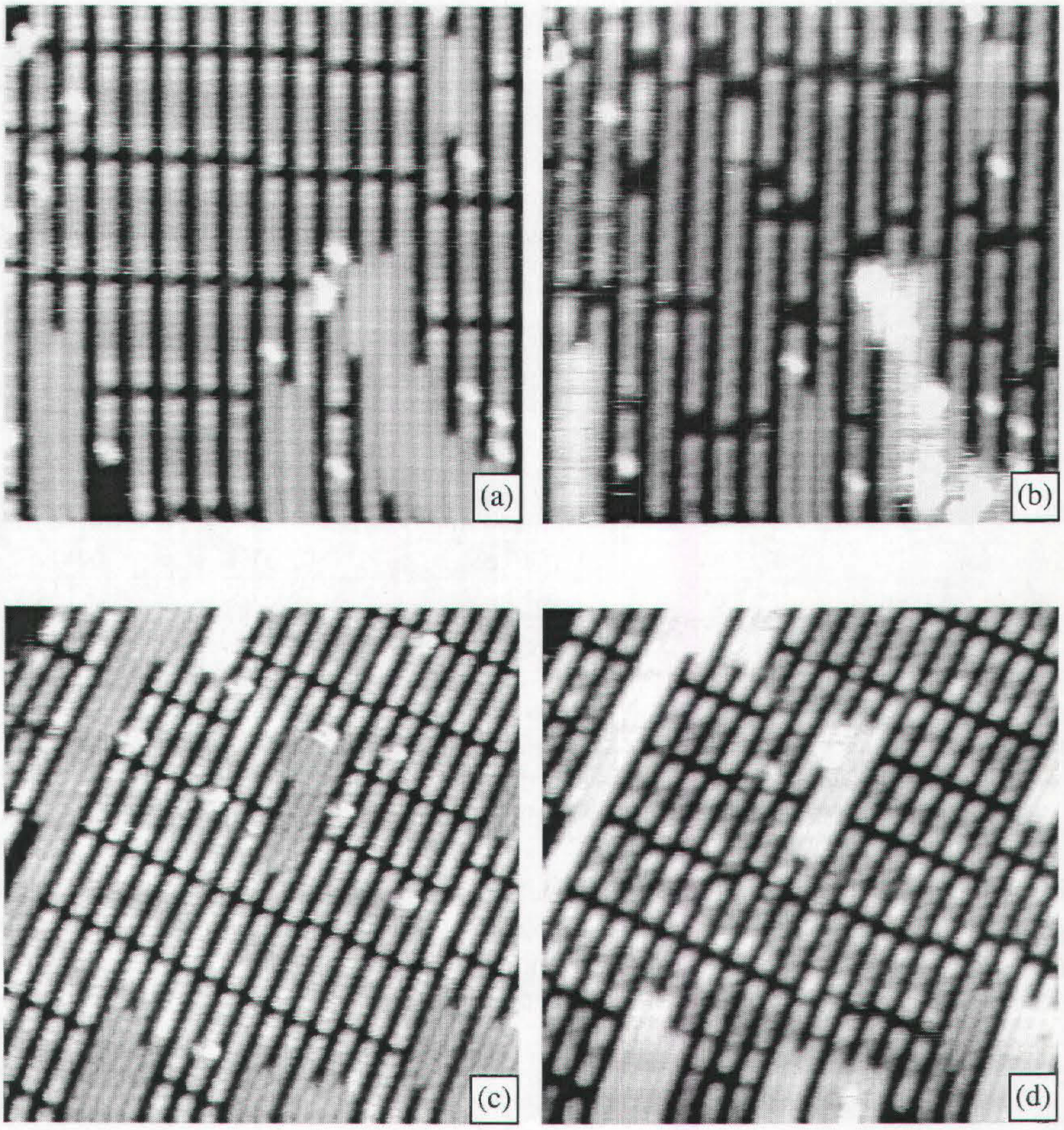

Figure 4.10: *Different order of the segment structure on the unstrained surface at different temperature due to different rhodium mobility. (a) Initial surface at 300 K (b) The same surface area after completion of the first reaction step. Size: 150×150 Å^2. (I=1 nA, V_B=+0.60 V). (c) Initial surface at 253 K. (d) Unstrained surface after the passage of the reaction front. Size: 200×200 Å^2. (I=0.76 nA, V_B=+0.41 V).*

A complete scenario for this first reaction step can therefore be delineated. Initiating at the segmentation termination, the reaction propagates in the close packed direction along a succession of segments, running through each segment from segment end to segment end and jumping across the segment separations (which are enlarged by the process) to subsequent segments.

This mechanism is supported also by DFT calculations by Li and Hammer. H_2 dissociation and OH formation have been studied on different areas of the surface: at the segmentation termination, in the middle of a segment and at the end of a segment (see Figure 4.11). (6×2) primitive cells were used in the calculations and strain and mismatch with the underneath layer were included.

It turned out that the process can easily start at the termination of the sequence while it can hardly initiate within a segmented area, as shown in the graph in the bottom part of Figure 4.11.

Theoretical results can be summarised as follows (all energies referred to the oxygen covered surface and an H_2 molecule in gas phase; TS = transition state):

	H_2 dissociation TS energy	Adsorption energy per molecule	OH formation TS energy	Released energy in OH formation
Termination	0.23 eV	-0.76 eV	0.02 eV	-0.90 eV
Middle of segment	0.67 eV	-0.14 eV	0.78 eV	-0.32 eV
End of segment	0.70 eV	-0.26 eV	0.90 eV	-0.50 eV

Li and Hammer investigated also the propagation mechanism of the reaction within a single segment. In the upper part of Figure 4.12, a single oxygen atom has been removed from the end of a segment. The binding energies of the three remaining nearest O are indicated. Oxygen labelled A, which is the one diagonally opposite to the vacancy, is the least bound. Therefore, after the removal of an oxygen atom from the end of a segment, the reaction does not involve the uncoupled atom (the one labelled B in figure) but propagates to the adjacent oxygen couple in the $[1\bar{1}0]$ direction. Next step is investigated in the lower part of Figure 4.12. Here a single O atom has been removed from the middle part of a segment. Even in this case, oxygen labelled A has the lowest binding energy, which means that again the reaction does not attack the uncoupled oxygen atom but the diagonally opposite one. Hence, once started from one end, the reaction propagates in the close packed direction, moving diagonally, as already above observed in STM images. As a consequence a zig-zag arrangement of remaining oxygen atoms results.

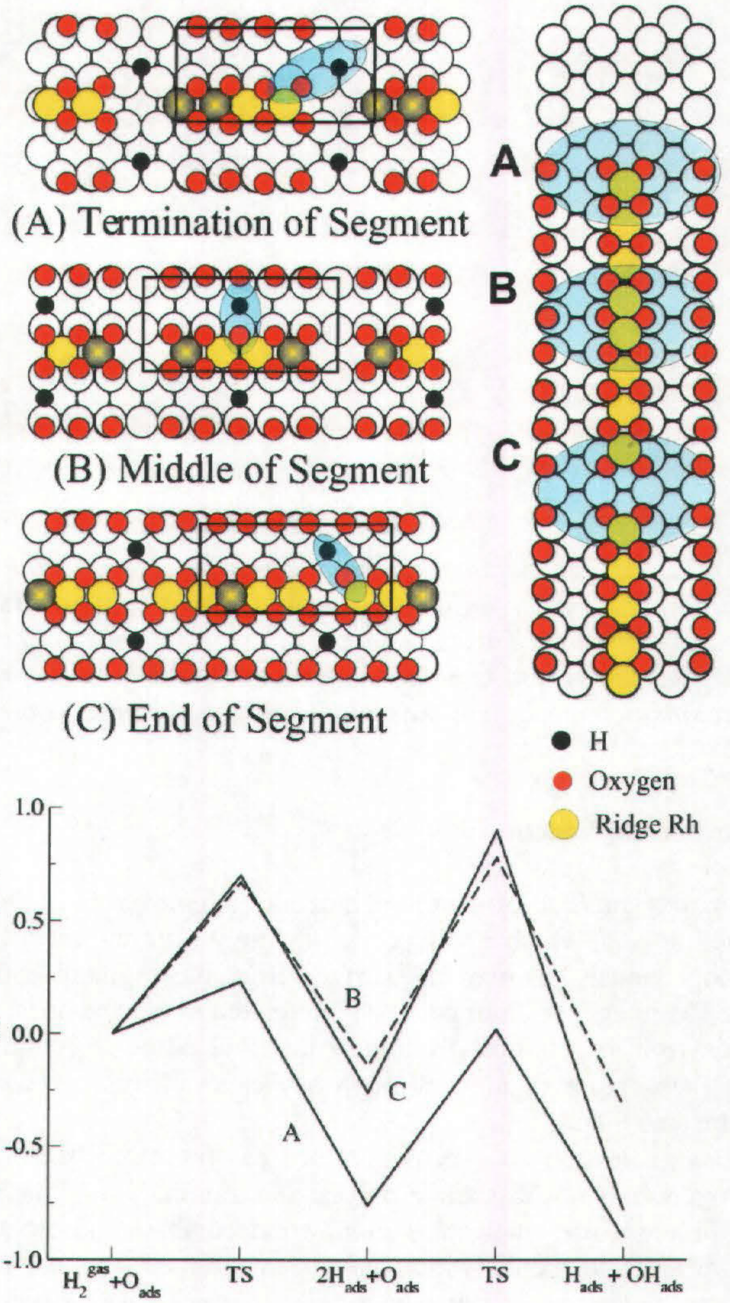

Figure 4.11: *DFT calculations on H_2 dissociation and OH formation at different surface sites. The upper part illustrates the various (6×2) primitive cells used in the calculations. Shaded atoms have been kept at a fix position while studying the reactivity.*

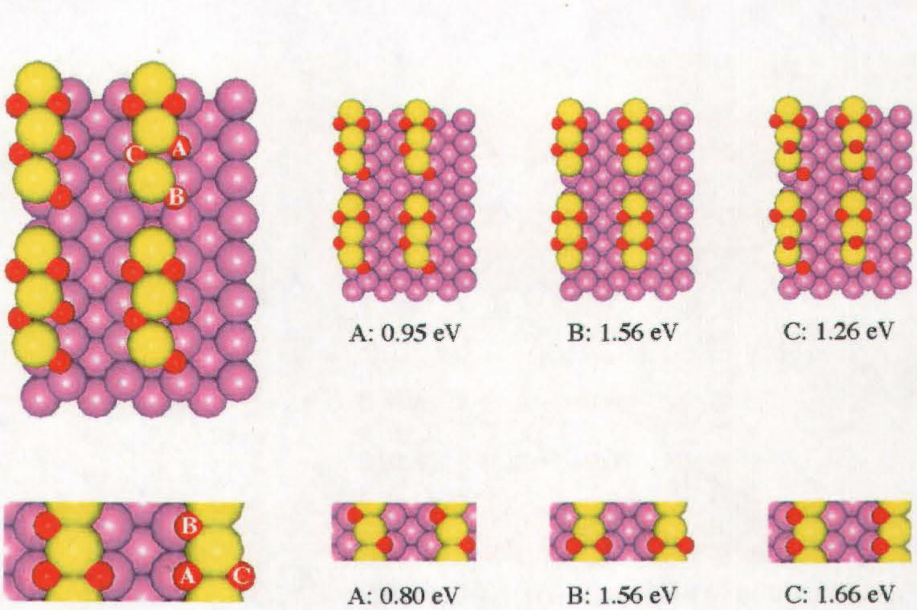

A: 0.95 eV B: 1.56 eV C: 1.26 eV

A: 0.80 eV B: 1.56 eV C: 1.66 eV

Figure 4.12: *DFT calculations on the propagation of the reaction through a segment. Models on the left represent the initial situation, with only one removed oxygen atom. Further removal of another O atom (whose binding energy is indicated) results in the shown configurations. In the upper/lower part, the situation at segment ends/middle part of a segment is presented.*

4.4.2 The Second Reaction Step

The remaining oxygen (half of the initial amount) is removed from the unstrained surface in a second reaction step, which involves a completely different mechanism. The reaction now starts homogeneously all over the surface from the segment ends on, as shown in Figure 4.13. In STM images brighter parts are interpreted as reacted ones, as already observed in a previous study on the titration reaction of the (2×2)p2mg structure [14]. The reaction proceeds along each single segment through a vacancy diffusion process from the ends towards the centre (see Figure 4.14).
The homogeneous nucleation all over the surface can be traced back to the fact that now molecular hydrogen does not dissociate only at the termination of the segmentation. DFT calculations confirmed that H_2 molecules are now indeed able to adsorb and dissociate in the separations between the segments (which have been enlarged after the strain removal in the first reaction step) and also at oxygen vacancies of the zig-zag structure, as sketched in Figure 4.15.

Figure 4.13: *Second reaction step proceeding from the segment ends all over the surface. Reacted parts appear brighter. Size: 150×150 Å^2. (I=1.00 nA, V_B=+0.60 V).*

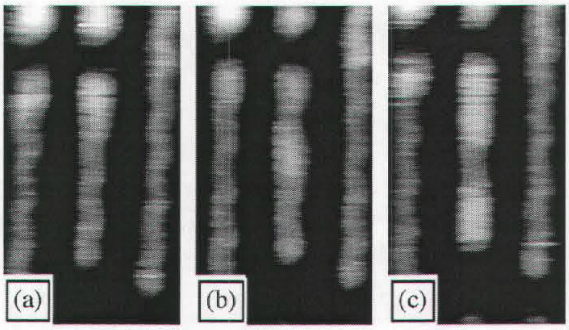

Figure 4.14: *Propagation of the second reaction step along a segment. (a) Only the ends on the indicated segment have reacted. (b) The vacancies diffused towards the center. (c) New vacancies are created at the ends. Time between images: 18 sec. Size: 25×45 Å^2. (I=1.00 nA, V_B=+0.60 V).*

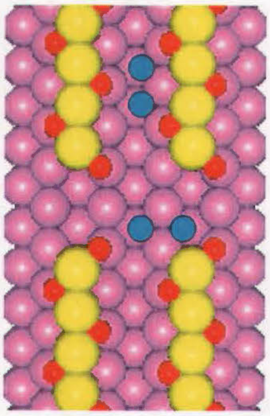

Figure 4.15: *Possible H_2 dissociation configurations in the second reaction step, as confirmed by DFT calculations. Note: the upper dissociation configuration is not possible on the (10×2)-O.*

The starting surface of this second reaction step closely resembles the (2×2)p2mg-O structure, with the difference that in the present case the close-packed Rh rows are segmented. This opens up the opportunity to study the influence of the segmentation on reactivity. The reactivity of the (2×2)p2mg-O structure has been characterised in ref. [14] in a temperature range between 380 K and 405 K. We repeated the measurements also at RT to reproduce the same reaction conditions as in this study. It turned out that the reaction is governed by the reactivity of defects, such as steps. In fact, as already mentioned in Section 3.3, at all investigated temperatures the reaction was always seen start at defects, from where it propagates via a reaction front, which involves a vacancy diffusion process. A higher reactivity of the edges of the (2×2)p2mg structure was confirmed by DFT calculations [56]. Nevertheless, at room temperature the oxygen removal is very slow. It is so slow that in previous global reactivity measurements the (2×2)p2mg was found to be unreactive at room temperature (see Figure 4.16) [48].

Conversely, the reaction on the segmented structure is much faster than on the (2×2)p2mg-O. This effect is related to the presence of the segmentation, with segment ends acting as mini-steps where the reaction can nucleate. The reaction mechanism, however, appears to be the same, with nucleation at defects and propagation through vacancies diffusion. Even the reaction front, observed on the (2×2)p2mg-O, can, in a certain sense, be found also on the segmented surface, when the reaction propagates from one end of a segment towards the centre. Thus, on each segment two local reaction fronts travel in opposite directions from the ends on.

The vacancy diffusion mechanism actually involves the movement of oxygen atoms. Oxygen is found to be very mobile at room temperature. Both direct observation on smallest scale images and height distribution in line profiles on larger scale images reveal diffusion along the close packed direction, from threefold site to threefold site, even jumping across the segment separations. Jumps between adjacent segments in the [001] direction are also possible, at least at room temperature, as evidenced by the two subsequent images in Figure 4.17.

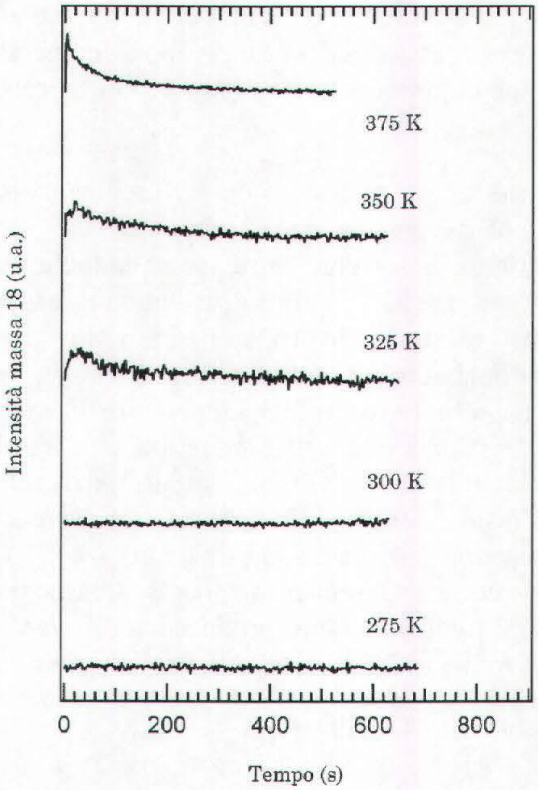

Figure 4.16: *Global reactivity measurements of water formation starting from the (2×2)p2mg-O/Rh(110) surface. Water production is plotted as a function of time. (p_{H2}=9×10^{-8} mbar on at t=0) [48].*

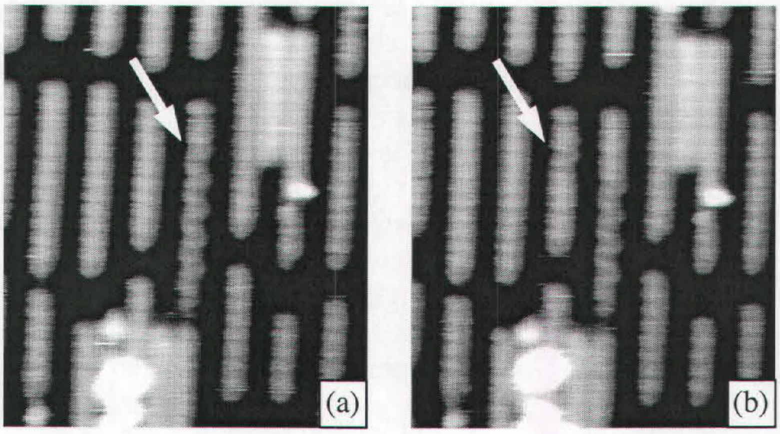

Figure 4.17: *Oxygen diffusion during the second reaction step at room temperature. The O atoms indicated by the arrow in (a) jumped to the adjacent segment on the left in (b). Size: 57×75 Å^2. Time between images: 18 sec. (I=1.02 nA, V_B=+0.63 V).*

The reaction front, and thus the first reaction step, crosses the whole imaged area (for an image size of 200x200 $Å^2$) in 4-5 images (at RT), i.e. 2-3 minutes. Conversely, completion of the second reaction step requires longer times. At room temperature about 20 minutes are needed, while at low temperature the situation is more complicated, as will be discussed in Section 4.8.2.

At room temperature the second step starts on each segment almost immediately after the removal of the first half of oxygen. In most cases one or two images, i.e. 20-40 sec, are sufficient. As the temperature is lowered, instead, an induction period is often necessary under the same hydrogen pressure and the time distribution is less narrow. This can be caused either by a lower mobility of atomic hydrogen or by a slower reaction. We repeated the experiment at constant temperature but with different hydrogen pressures and it turned out that no induction period is present even at low temperature when the pressure is increased by two orders of magnitude. Concerning the induction period, thus, the reaction at low temperature behaves as at RT when hydrogen supply is increased. Therefore, it can be inferred that hydrogen diffusion is the rate-limiting step for the reaction.
At low temperature the reaction starts in a short time only when hydrogen dissociates exactly inside the separation between two subsequent segments. A large time distribution arises from different diffusion times for hydrogen atoms produced at different distances from the ends of a segment, which are, due to their higher reactivity, the only sites where the reaction is seen to start.

4.5 The Reaction Front

As already discussed in Section 3.3, a previous STM study dealt with the formation of a front in the water formation reaction on the Pt(111) surface [34]. In that case, a ring of OH islands expands on the O pre-dosed surface leaving behind areas covered by water, which does not desorb at the investigated temperatures (below 170 K). The propagation was therefore explained as an autocatalytic process, which involves the migration of water molecules towards the unreacted areas through the OH ring. In our case, though, water desorbs immediately, and similar explanations are unlikely to hold. The formation of a reaction front can instead be rationalised by the dissociation of molecular hydrogen: on the initial surface, H_2 molecules are not able to dissociate on the terraces. On the contrary, on the unstrained, 0.5 ML O covered surface, the molecules can dissociate in the segmentations, enlarged by the strain removal, and in the troughs. The first reaction step appears therefore as a front, with the hydrogen dissociation blocked ahead of it and occurring on the unstrained areas behind it. The formation of free adsorption sites for hydrogen dissociation is thus the autocatalytic step.

The reaction front has been studied on various length scales, starting from images of large areas of the surface ($0.5 \times 0.5\ \mu m^2$) down to atomic scale images. Such a procedure ensured to follow all details both of the nucleation and of the propagation.

4.5.1 Propagation of the Wave Front Above 273 K

Figure 4.18 shows a 0.5×0.5 μm^2 area at room temperature. The topographic image (a) has been filtered (b-d) in order to highlight the front. The filtering procedure consists in the removal of topographic features (i.e. all areas of the surface are shifted to the same average height) followed by a second filter, which enhances small height differences confined in narrow areas. Finally the contrast is maximised. As a result, small brighter patches are highlighted. As will be described in the following, unreconstructed areas of the surface appear always brighter while reacting and therefore surface regions already crossed by the reaction front appear as a collection of small brighter features in the filtered image.

The topography of the surface in Figure 4.18 is characterised by the presence of three large, one layer deep holes. Small, circular, bright patches are local distortions due to subsurface argon bubbles, which cannot be completely eliminated during the preparation procedure. The reaction front originates from a few specific areas at step edges and has an anisotropic shape, elongated in the $[1\bar{1}0]$ direction. In subsequent images the various wave fronts grow until they merge (not shown), thus covering the whole surface area in about 20 minutes.

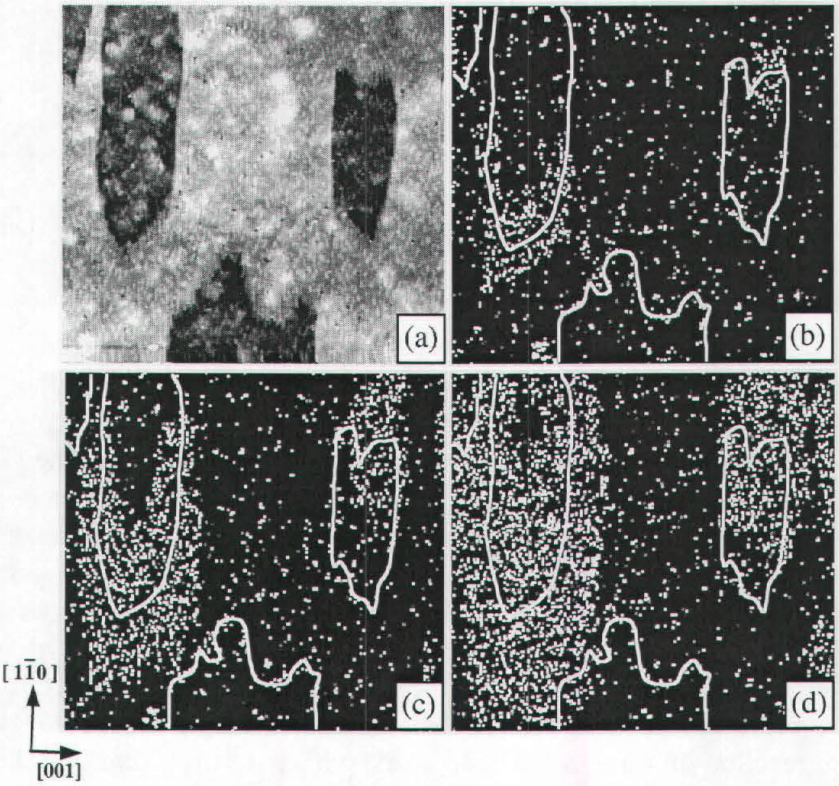

Figure 4.18: *The reaction front at RT. (a) Topographic image of the surface. (b) The image has been filtered (see text) in order to enhance the front contrast. Reacted regions appear brighter. White lines indicate monoatomic steps. (c-d): The reaction front propagates in an anisotropic way, faster along* $[1\bar{1}0]$. *Size:* $0.5\times0.5\ \mu m^2$. *(*$I=1.00$ *nA,* $V_B=+0.63$ *V).*

If the experiment is repeated at 276 K, the behaviour is slightly different. Images are much more confused, with the front nucleating also on the terraces at specific points, whose identification will be clear in the following. Even the front shape is changed: now it is almost isotropic. It takes about 35 minutes to cover the whole imaged area.
The above differences suggest that the temperature strongly influences the reaction mechanism.

The propagation proceeds regardless of topographic features. As shown in Figure 4.19, steps are crossed without changing the front shape. Local substrate distortions due to argon bubbles as well do not affect the reaction. When encountering unreconstructed areas, these are usually immediately included in the reaction, without accelerating or slowing down the front.

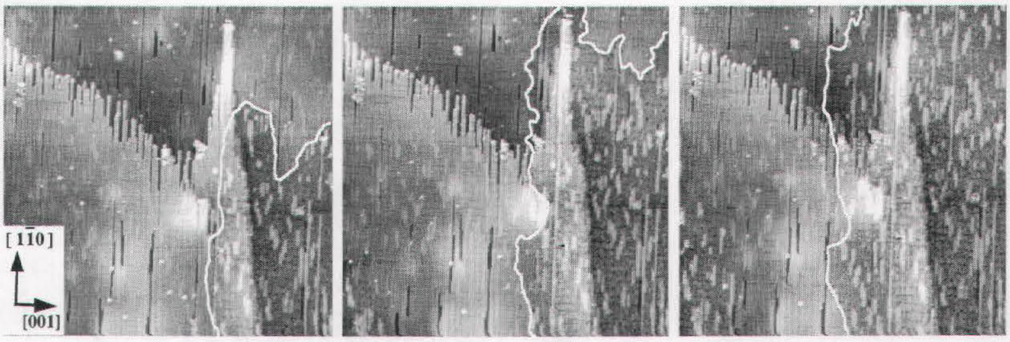

Figure 4.19: *Propagation of the reaction front across a step. Time between images: 88 sec. Size: $0.14\times0.14\ \mu m^2$. ($I=0.21$ nA, $V_B=+0.73$ V, RT).*

The reaction on unreconstructed areas, which are initially covered by the (2×1)p2mg-O structure, develops as on the pure (2×1)p2mg-O layer (see Chapter 3), even though the formation and the order of intermediate structures depend on the width of the (1×1) substrate. If the unreconstructed patch is at least six $[1\bar{1}0]$ rows wide, pairs of oxygen atoms form in all internal rows, which order in the c(2×4) structure (see Figure 4.20) before desorption as water molecules. Despite the actual width, the lateral $[1\bar{1}0]$ rows remains zig-zagged, which means that O atoms are still adsorbed on them in zig-zag threefold sites. These atoms are reacted off only in a later phase. Lateral oxygen atoms, therefore, are stabilised. On narrower unreconstructed areas there is no room for the formation of a couple structure; only trimers are observed on five $[1\bar{1}0]$ rows wide regions (see for example Figure 4.7(c)). Even more difficult is the reaction on three rows wide areas, which start reacting only later and at the lowest investigated temperatures may also not react at all.
The appearance of features (pairs, trimers or just fuzzy bright features) above the substrate during the reaction on unreconstructed regions makes the latter look brighter and can therefore be used for the contrast enhancement of the large scale images (Figure 4.18 and Figure 4.19).

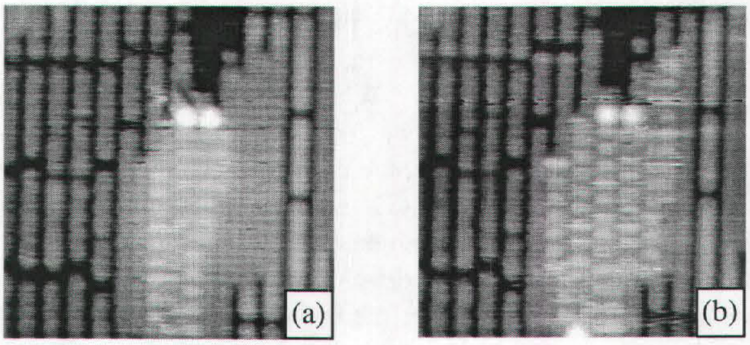

Figure 4.20: *Reaction on unreconstructed areas. (a) Pairs of oxygen atoms form in internal rows and (b) order in the c(2×4) structure. Time between images: 28 sec. Size: 130×130 Å^2. (I=0.22 nA, V_B=+0.90 V, T=276 K).*

The anisotropy and the velocity of the reaction front have been studied in detail.
First of all it has to be noticed that the shape of a wave front in an STM image is not the real shape, because the STM image is a scanned image, recorded line by line and not a snapshot of the surface. Thus, different points on a curve that evolves on the time scale of the scanning may be acquired with different time delays and a distortion of the actual shape results. Correction of this distortion allows determining accurately the front velocities (see description in ref. [57]).
Several movies were considered, on various length scales and at different temperatures. Consecutive images were compared, after correcting for a rigid shift due to the drift, which always remains also after correction during scanning. The movement of the reaction front between subsequent images was measured and corrected for distortion due to the scanning procedure.
Impressions already inferred when looking at the images were confirmed. At the lowest investigated temperatures, the propagation velocities in the [001] and in the $[1\bar{1}0]$ directions are almost equal. If the temperature is raised, the velocities in both directions are raised as well but with a higher rate in the $[1\bar{1}0]$ direction.
A propagation velocity can be expressed as:

$$v = v_0 e^{-\frac{E_A}{k_B T}}$$

where v_0 is the pre-exponential factor and and E_A the activation barrier.
Results are summarised in the following table:

	[001] direction	$[1\bar{1}0]$ direction
Pre-exponential factor	~10^5 nm/min	~ 10^8 nm/min
Activation energy	263 meV (=25 kJ/mol)	410 meV (=40 kJ/mol)

A similar propagation front was found in a previous study by Mertens and Imbihl, who investigated the $H_2 + O_2$ reaction on Rh(110) at high temperature (480÷780 K) by PEEM (PhotoElectron Emission Microscopy) [58]. When applying $T<600$ K and high hydrogen pressures, a similar anisotropy as the one we found at RT was revealed and an activation energy of 49 kJ/mol was inferred. However, the anisotropy changes when the temperature is increased or the hydrogen pressure lowered. Conversely to the change observed in our case, in the PEEM study the anisotropy first diminishes and then increases again but with faster propagation in the [001] direction. Makeev developed a realistic mathematical model, which reproduces almost quantitatively the experimental data [59]. Diffusion of hydrogen and oxygen and a strong inhibitory site-blocking effect of adsorbed O on adsorption and diffusion of hydrogen had to be introduced in order to explain the change in the anisotropy.

These findings, however, can not be directly compared with our work. First of all the initial structure was not the strained (10×2) but a surface with mixed unstrained c(2×2*n*) structures. The possibility of opening new diffusion channels for hydrogen in the [001] direction along the segmentations might be a determining factor for the propagation and actually it is at lower temperatures (see Section 4.8.1). Moreover, bistability conditions were established in the PEEM experiment, where the surface was exposed to oxygen and hydrogen simultaneously, thus the structure was continuously formed and destroyed. Finally the hydrogen pressure was two orders of magnitude higher.

Nevertheless, the order of magnitude of the activation energy found in our work is the same as the one inferred by the PEEM experiment and the anisotropy might agree with a fit for lower temperatures of the values for the anisotropy in ref. [58] as well.

4.5.2 Nucleation of the Wave Front

Starting from large-scale images, we analysed the nucleation of the reaction front.

As shown in Figure 4.18, at room temperature the reaction starts at jagged step edges. Based on this observation, we took smaller scale movies on surface areas with a step at several temperatures. Obviously not all the steps are nucleation centres but after a few unsuccessful tries we succeeded in imaging the beginning of the reaction. Figure 4.21(a) is extracted form a movie acquired at 274 K on a 500×500 Å^2. It proves that the reaction can start at step edges on the lower terrace, where a wide enough unreconstructed region is present. In fact, the arrow points to an area where fuzzy bright features appear on the unreconstructed surface below the step. The nature of these fuzzy bright features will be clear in the next section. On these unreconstructed areas also a few diffusing single rhodium atoms, originating from the strain removal on the outermost (10×2) segments on the upper terrace, are recognisable.

As already pointed out, at T<RT the front nucleates even on flat terraces. This is evidenced in Figure 4.21(b), in which the arrows indicate darker regions where small holes (or at least double missing rows) are close to unreconstructed areas. The darker appearance is due to the transformation of (10×2) segments to (2×2)p2mg patches, which appear always lower in STM images. These regions are centred in unreconstructed areas that in turn appear brighter, which is again a fingerprint of an ongoing reaction.

What is common to all nucleation centres, thus, is the presence of unreconstructed areas close to defects, where the reaction begins.

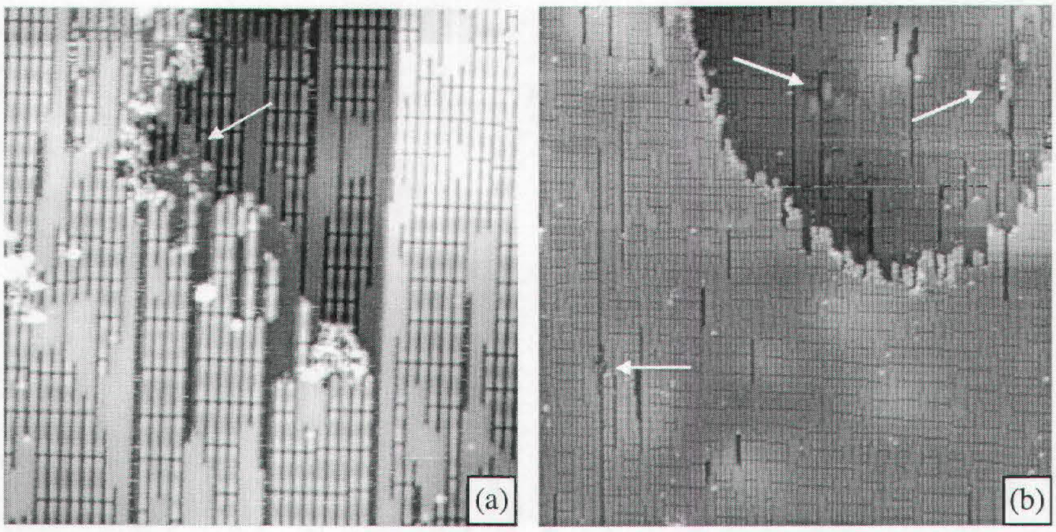

Figure 4.21: *Nucleation of the reaction front. (a) Beginning of the reaction at step edge. The arrow points to fuzzy bright features on the lower terrace, which are a fingerprint of the reaction. Size: 500×500 Å^2. (I=0.46 nA, V_B=+0.65 V, T=274 K). (b) Nucleation on flat terraces, where unreconstructed areas are closed to double missing rows. The reacted regions, marked by arrows, appear darker. Size: 0.1×0.1 µm^2. (I=0.52 nA, V_B=+0.60 V, T=278 K).*

4.6 Details of the Beginning of the Reaction

On smaller scale movies, we followed the onset of the reaction.
Figure 4.22 shows a 200×200 Å^2 region of the surface at step edge. The reaction starts on the unreconstructed area, beginning from the step. Here it develops via the formation of oxygen pairs (Figure 4.22(a)) and propagates as a wave front up to the borders of the area, exactly as on the pure (2×1)p2mg structure (see Chapter 3). Once the whole unreconstructed area is covered by the c(2×4)-O structure (Figure 4.22(b)), the reaction attacks the strained (10×2)-O surface (Figure 4.22(c)). The presence of a step does not influence the propagation, i.e. there is no preference for propagation to the upper or lower terrace. During the first reaction step on the segmented area, the reaction continues on the unreconstructed region, with the formation of the c(2×2)-OH structure (Figure 4.22(d)), before producing a clean surface. It is interesting to notice that the OH structure is much more stable in this case than on a pure (1x1) substrate (it remains on the surface for a double period of time – ~30 min vs. ~15 min at the same temperature and with the same hydrogen pressure). This difference is probably related to the different extension of the (1×1) substrate, due to the closeness of the segmented part of the terrace and due to the absence of defects in the structure: OH islands often occupy the whole unreconstructed area and therefore there is no room around them. This seems to affect their

reactivity. OH remains stable above the temperature where H_2O desorption due to disproportionation is observed in the TDS (see Section 3.5.2)

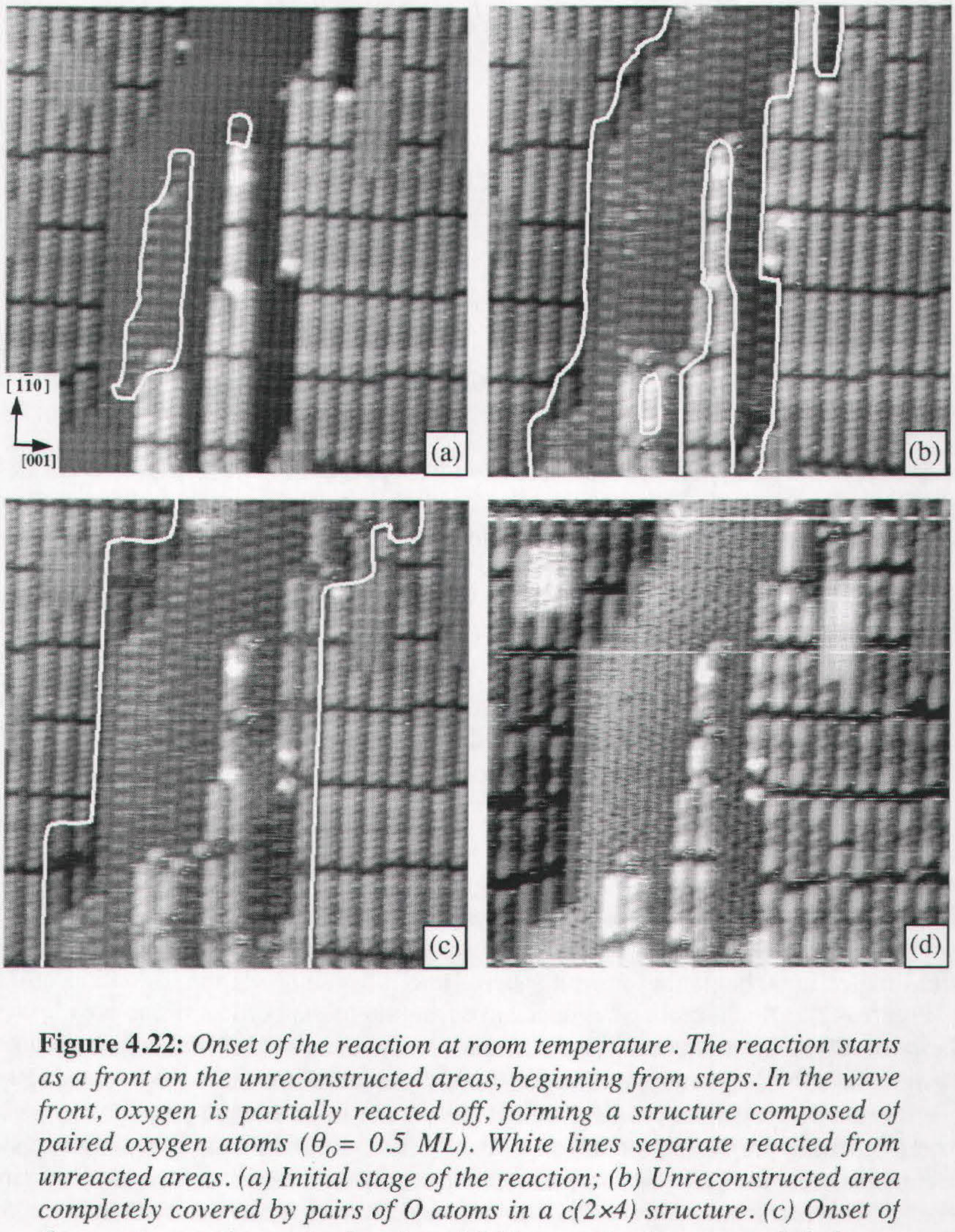

Figure 4.22: *Onset of the reaction at room temperature. The reaction starts as a front on the unreconstructed areas, beginning from steps. In the wave front, oxygen is partially reacted off, forming a structure composed of paired oxygen atoms (θ_O= 0.5 ML). White lines separate reacted from unreacted areas. (a) Initial stage of the reaction; (b) Unreconstructed area completely covered by pairs of O atoms in a c(2×4) structure. (c) Onset of the reaction on the strained surface. (d) The reaction has proceeded also on the unreconstructed area, where a c(2×2)-OH formed. Time between (a) and (b) 280 sec; (b) and (c) 140 sec; (c) and (d) 980 sec. Size: 200×200 Å^2. (I=0.90 nA, V_B=+0.25 V).*

In agreement with DFT calculations, in our measurements we never observed the reaction starting directly on segmented areas. This means that the coexistence of the two regions is necessary, i.e. a pure strained (10×2)-O surface, without unreconstructed regions, would be unreactive.

From our measurements, we can tentatively go further in the analysis of the beginning of the reaction.

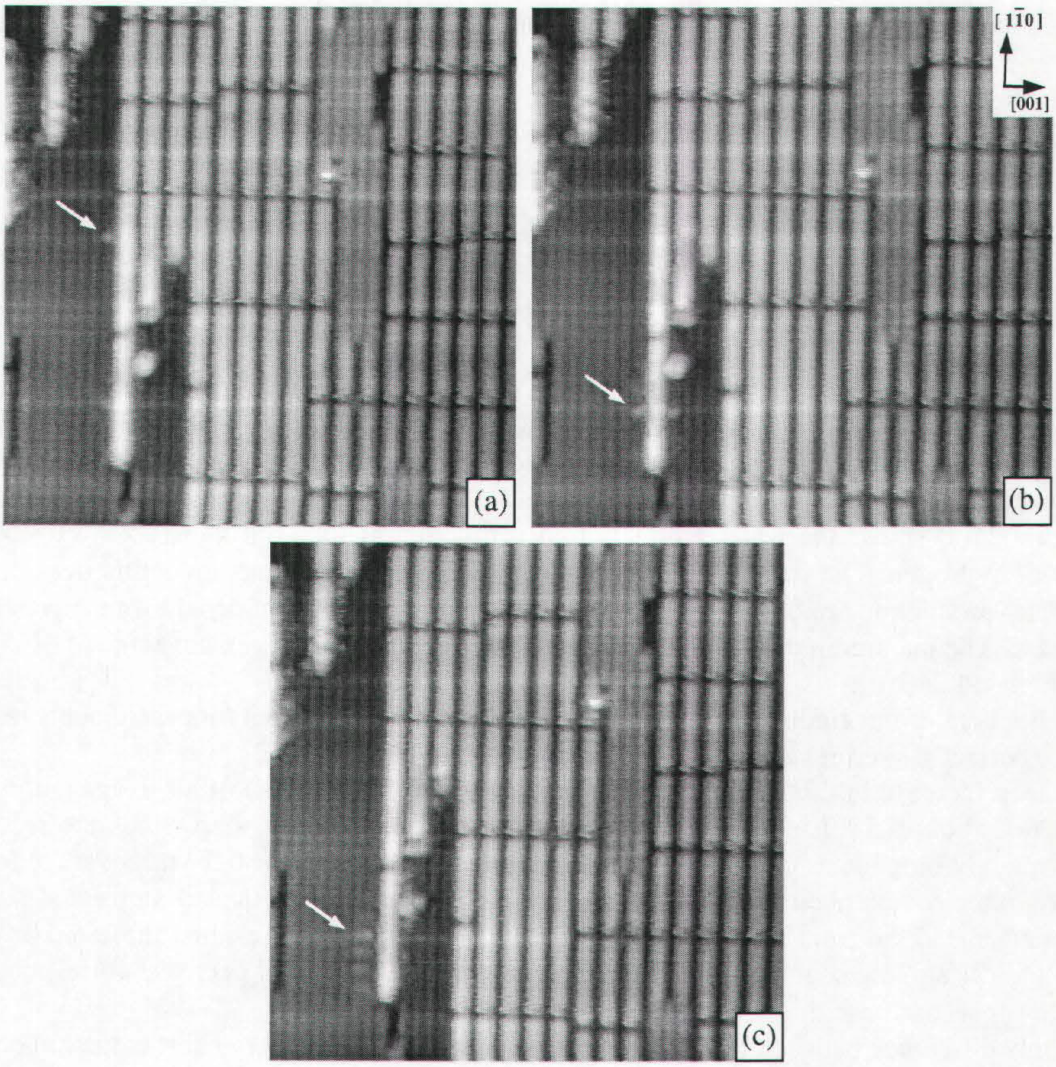

Figure 4.23: *Moving features along step edges. (a) When hydrogen exposure is started a feature immediately appears at the border of the step (see arrow). (b) The feature diffuses along the step in the* $[1\bar{1}0]$ *direction. (c) Where the moving feature disappears the reaction starts: O pairs appear. Time between (a) and (b) 140 sec; (b) and (c) 70 sec. Size: 150×180 Å*^{2}*. (I=0.86 nA,* V_B*=+0.46 V, T=263 K).*

When starting hydrogen exposure, single features appear at step edges and diffuse in the close packed direction, running along the borders of the segmented (10×2) (see Figure 4.23). The reaction starts exactly at the place where the "moving features" disappear.

We cannot infer any precise information about the chemical identity of this species but we propose that they are the first OH groups formed when atomic hydrogen (produced by dissociation at defects) binds to oxygen atoms, adsorbed in threefold sites in the (2x1)p2mg structure. OH groups diffuse along the step, probably via a proton hopping process. This mechanism, often present in proton conduction in oxides [60,61], does not involve a movement of the whole OH group, but is based on the exchange of an H^+ between adjacent oxygen atoms. When an OH group finds another OH group or another single hydrogen atom, a water molecule forms, via a disproportionation or recombination reaction respectively. The water molecule desorbs immediately, thus leaving enough free room for further hydrogen dissociation and hence the reaction can start.

4.7 Reactivity of (10×2)-O/Rh(110): Macro vs. Micro Measurements

The reactivity of the (10×2) structure has been previously studied by global reactivity measurements in ref. [48] in the 275÷375 K temperature range. The global reactivity measurements setup, which dealt with the reactivity of all oxygen structures on the Rh(110) surface, has already been described in Section 3.7.

Figure 4.24(a) shows the water production as a function of time during exposure to 9×10^{-8} mbar of hydrogen. The reaction starts immediately, with a very short induction period, and the water production rapidly increases up to a maximum, which is followed by an exponential decrease. The maximum production corresponds to a remaining oxygen coverage of ~0.5 ML (see Figure 4.24(b)).

With the help of our findings on the atomic scale, the global reactivity measurements results can be correctly interpreted.

The steep increase in the first part of the reaction, up to the removal of all oxygen atoms in excess of about 0.5 ML coverage, corresponds to the first reaction step, when the reaction front quickly propagates on the surface. A maximum production for 0.5 ML coverage left is related to the contemporary removal of the first half of oxygen from the still unreacted (10×2) segments ahead the front and the beginning of the removal of the residual threefold oxygen from the (2×2)p2mg segments behind it. The following exponential decrease corresponds to the slower second reaction step.

The only difference between macro- and micro-scale results is the very short induction period observed in the macroscopic measurements, which was conversely much longer in microscopic STM measurements. This might be explained by the higher hydrogen pressure used in global reactivity measurements.

The absence of an induction period global reactivity measurements on the (10×2) seems also in contradiction with the global reactivity measurements results for the (2x1)p2mg (see Section 3.7): in the latter spectra, in fact, the beginning of the reaction is indeed postponed but we know, from our atomic scale measurements, that the reaction on the (10×2) surface starts on the unreconstructed, (2×1)p2mg-O covered, areas. Thus this is an example of a surface structure whose reactivity is enhanced by the coexistence with another surface structure.

This effect might be explained by the reduced size of unreconstructed substrate regions on the (10×2) surface. The "moving features", tentatively assigned to OH, are confined in the vicinity of a step and the probability of finding another OH group or a hydrogen atom increases, leading to a faster beginning of the reaction.

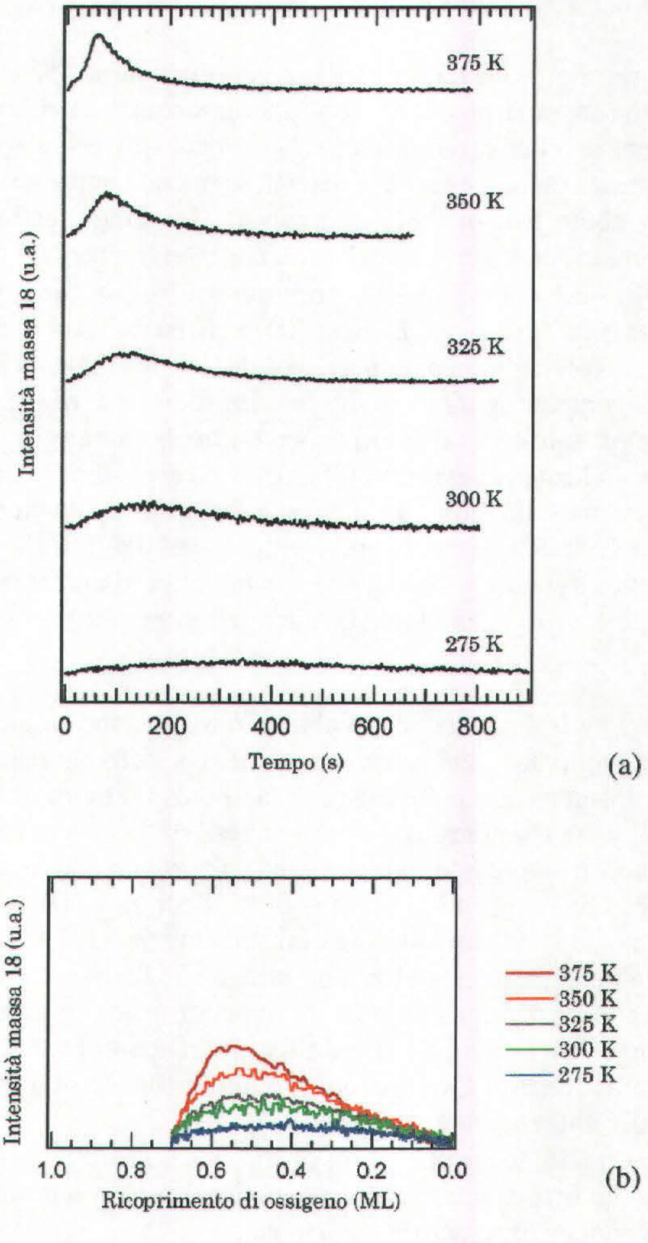

Figure 4.24: *Global reactivity measurements of water formation starting from the (10×2)-O/Rh(110) surface. (H_2 valve opened at $t=0$ with pressure of 9×10^{-8} mbar) (a) Water production as a function of time. (b) Reactivity as a function of remaining oxygen coverage [48].*

4.8 The Reaction at low temperature

The catalytic oxidation of hydrogen on the (10×2)-O/Rh(110) surface exhibits particular features at low temperatures (235÷260 K), when it is governed by the segmentation.

4.8.1 Comb-like Reaction Front

Figure 4.25 shows the propagation of the reaction front at 253 K. The front enters the imaged area from the top and proceeds along the unreconstructed hole in the centre of the upper half of the image. When it reaches a [001] channel between aligned segments, it enters the channel and the reaction moves to the adjacent segments, but is not able to run along their whole length. Only about half of them is involved. Thus the reaction travels in the [001] direction, propagating to the lower halves of the upper segments and the upper halves of the lower segments. In the mean time it continues also in the main $[1\bar{1}0]$ elongated unreconstructed area until it reaches the next [001] channel. Then it enters also this channel and travels along it, involving the upper halves of the lower segments and the lower halves of the upper segments, completing on them the first reaction step. In the sequence of images in figure, the arrow helps to follow this mechanism on the bottom right quadrant: in (a) – (b) it propagates along the indicated channel, in (c) – (d) it involves the next channel.
The reaction front assumes, therefore, a comb-like shape, with a main propagation trough and many orthogonal teeth. It behaves as if at the entrance of the [001] teeth there were gates to open: once the reaction reaches a gate, it opens that gate and enters the channel. The role of gate is played by the four oxygen atoms in distorted threefold sites at the ends of opposite segments

The question is: why is the reaction not able to run along the whole segment once it starts at one end? We don't think that this behaviour is due to a different reactivity of oxygen atoms placed in different positions along the segment (and thus on more or less distorted threefold sites), because usually the reaction stops slightly ahead of the centre and thus there would not be O atoms with a new reactivity on the unreacted part, which is basically just a mirror image of the reacted one. Our suggestion is that this effect is related to the strain. At low temperatures, its removal results in a sliding of metal atoms to the closest hollow site, because they have not enough energy to cross the long bridge site barrier. As a consequence, starting from one segment end, the propagation of the reaction leads to a decrease of the reacted-unreacted metal atoms distance until it crosses the central part of the segment. Then the strain removal leads to an increase of the rhodium-rhodium distance. A further propagation, thus, might be energetically unfavourable.
If this interpretation holds, the propagation of the reaction front at low temperature on the (10×2)-O surface is the first example of how the interplay between surface strain and surface segmentation can modulate the reactivity of a metal.

The transition from a uniform reaction front to a comb-like one is not sharp. Above 273 K only a uniform reaction front was found in all our measurements. When decreasing the temperature, the comb-like mechanism starts to compete and becomes predominant around 260 K. At 238 K only the comb-like mechanism was found. The appearance of this kind of propagation is certainly facilitated by the reduced metal transient mobility at low temperature. As already observed in Section 4.4.1, the strain removal leads to a disordered surface at room temperature and thus to a destruction of the [001] channels, while the segments remain almost aligned when the temperature is lowered.

Nevertheless, it is also possible that even a uniform reaction front at room temperature has locally a comb-like shape that is not resolved in our movies because it develops on a faster time scale. When lowering the temperature the process is slowed down and thus becomes visible.

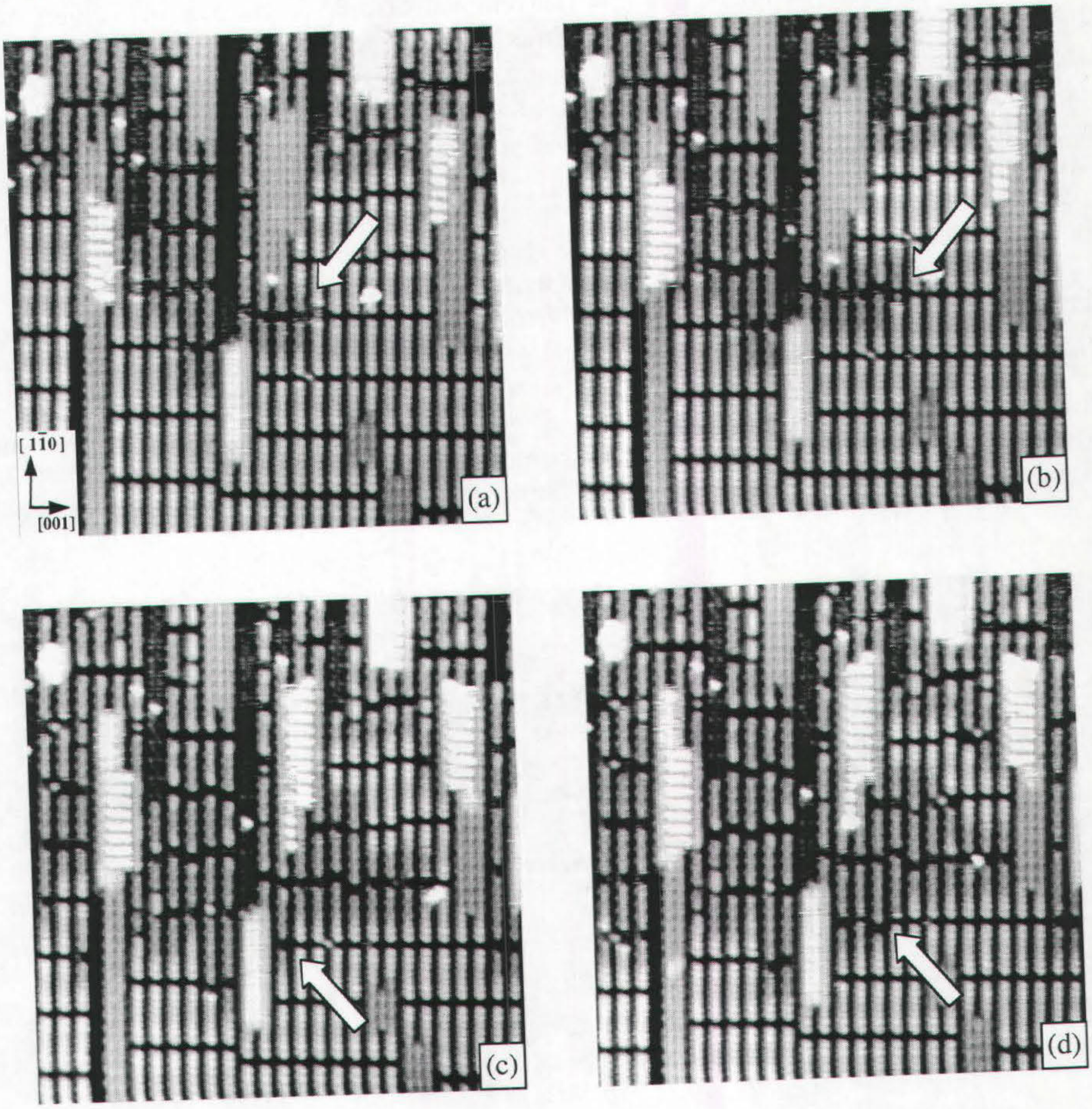

Figure 4.25: *Propagation of the reaction front at low temperature. (a) The reaction enters the [001] channel indicated by the arrow propagating to the adjacent segments up to half of their length and (b) it proceeds along the channel. (c) From the main unreconstructed patch the reaction reaches the next channel (see arrow) and (d) propagates along it completing the first step on the upper segments and initiating it on the lower segments. Time between (a) and (b) 35 sec; between (b) and (c) 3 min; between (c) and (d) 35 sec. Size: 260×260 Å^2. (I=0.60 nA, V_B=+0.60 V, T=253 K).*

4.8.2 Oxygen Nanopatterning in the Second Reaction Step

Also at higher temperatures, as already observed in Section 4.4.2, the second reaction step is strongly influenced by the presence of the segmentation.
Nevertheless, when lowering the temperature this influence leads to a unique effect.

We saw at higher temperatures that the removal of the second half of oxygen starts homogeneously on the surface behind the front from segment ends on. We highlighted that the initial surface in the second reaction step is like a segmented (2×2)p2mg-O. We also observed that the presence of the segmentation modifies the reactivity of the (2×2)p2mg, since on the segmented surface the reaction is much faster, even though the mechanism is the same.
At low temperature the picture is the same but the reaction is never completed (even after 3 hours of waiting), a certain number of oxygen atoms always remains on the segments. Moreover the number of remaining O atoms depends on the reaction temperature.
Figure 4.26 demonstrates how, at least locally, this results in a precise oxygen nanopatterning. At 253 K four O atoms remain in the central part of the segments (see (a)), at 258 K three atoms (b) and at 263 K only two oxygen atoms are still bound in the middle of each segment (c).
The number found at 253 K seems to be the maximum amount of oxygen atoms that can remain on the segments. In fact, even when further lowering the temperature, we never found a less reacted surface.

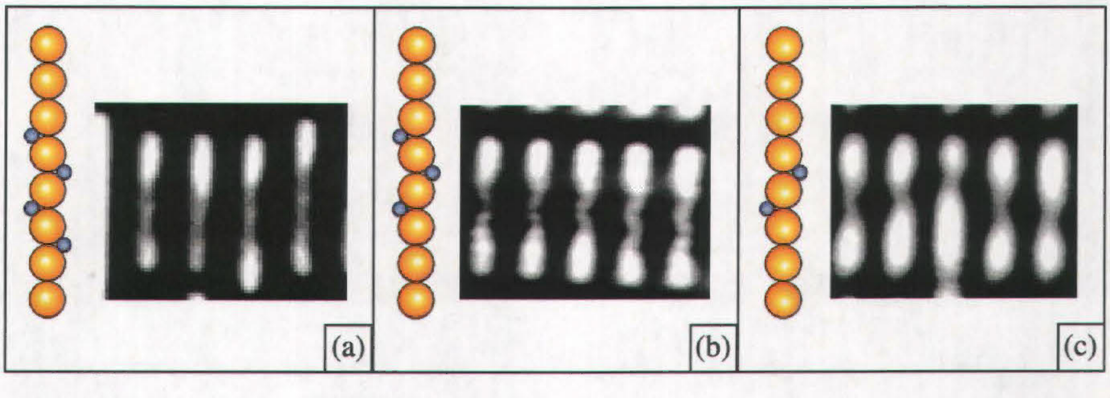

Figure 4.26: *Oxygen nanopatterning due to limited reactivity in the second reaction step. (a) When the reaction is carried out at 253 K, about four O atoms remain on each segment. (b) At 258 K about three atoms are present. (c) At 263 K only two oxygen atoms are still bound to threefold sites in the middle of each segment. Size: 48×37 Å^2.*

The order of the pattern is not precisely retained on the long range. In Figure 4.27 an image of a 400×400 Å^2 wide region of the surface at 238 K, the lowest investigated temperature, is shown. Here there are four O atoms left on most segments but more reacted and less reacted segments are present as well. As a general trend, the overall order decreases when increasing the temperature.

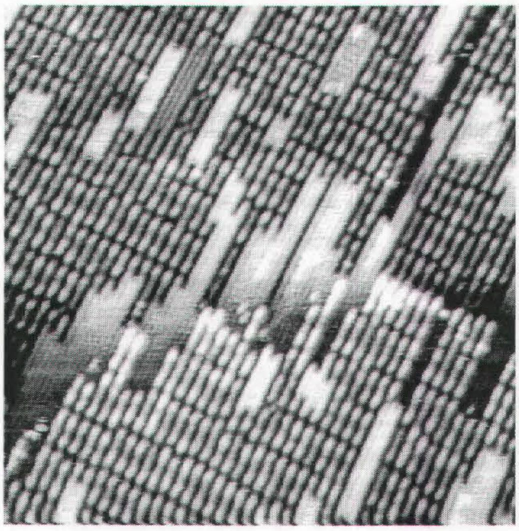

Figure 4.27: *Long range order of the O pattern at 238 K. On most segments four oxygen atoms are present. Size: 400×400 Å^2. (I=0.71 nA, V_B=+0.60 V).*

We prepared a surface where (2x2)p2mg segments of different length are simultaneously present and monitored the pattern formation. In order to obtain such a surface, we started from a well ordered (10×2). When reacting the structure at 293 K clean segments of various lengths are created. If this surface is slightly reoxidised (2 L) at low temperature (223 K) and then flashed to higher T (~293 K), the segments are covered by oxygen atoms in threefold sites, which order in a zig-zag fashion without modifying the segment structure. Therefore a surface with (2×2)p2mg segments of various lengths with only very small patches of (10×2) symmetry as defects is produced.

The surface has been exposed to 1×10^{-8} mbar of H_2 at 258 K. It turned out that the number of remaining oxygen atoms on segments with different lengths is not constant at all. Nevertheless, what is more or less constant is the length of the reacted areas on each segment end (see Figure 4.28). This means that the pattern formation is not governed by the stability of the remaining oxygen configuration but by a limitation in the propagation of the reaction from the segment ends.

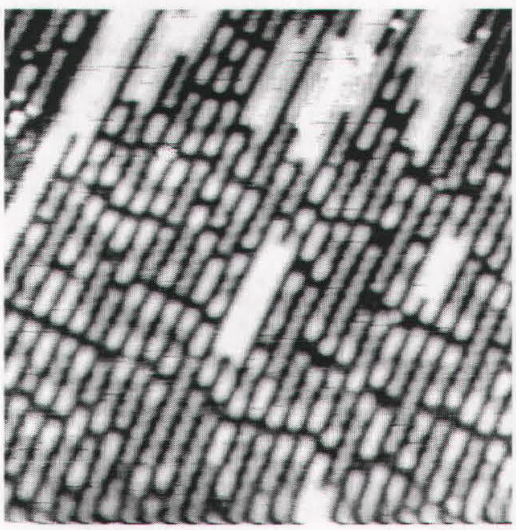

Figure 4.28: *Second reaction step on segments with different length. The length of the reacted part of each segment is similar. Size: 250×250 Å^2. ($I=1.00$ nA, $V_B=+0.60$ V, $T=258$ K).*

If an oxygen pattern is slightly heated up, the number of reacted oxygen atoms increases very slowly. The pattern becomes also less ordered, because oxygen chains can even diffuse along the segments as a whole, jumping across segment separations, thus forming dense islands, leaving wide clean surface areas. Chains of two atoms are allowed to move (at least on a single segment) at all investigated temperatures. Conversely, the longest chains are the least mobile thus the island formation effect is much more relevant when starting from T≥258 K, while at lower T the conversion into a lower coverage pattern is more probable.
However, the pattern created at a certain temperature is never automatically reverted to a lower coverage one, as if the whole reaction were carried out at a higher temperature.

The limited reactivity does not depend on hydrogen supply, since the final pattern is the same even when exposing to two orders of magnitude higher hydrogen pressures.
At all investigated temperatures the removal of zig-zag oxygen atoms initially proceeds quite quickly until the pattern is formed. Nevertheless, the reaction is never stopped, it continues even on the patterned surface but is extremely slow.
Why is the reaction slowed down?
It might be a poisoning effect due to adsorption of contaminants from the gas phase and it indeed is when applying high hydrogen pressures (1×10^{-6} mbar). In this case brighter protrusions placed in a zig-zag fashion across the ending parts of the segments (and on the unreconstructed areas) are clearly imaged (see Figure 4.29). We identify this adsorbates as CO molecules, which indeed form a (2×2)p2mg structure on a (1×2) substrate and a (2×1)p2mg structure on the unreconstructed surface [38]. Nevertheless for lower hydrogen pressures we never saw these features and thus we do not believe in a CO poisoning effect at low p.

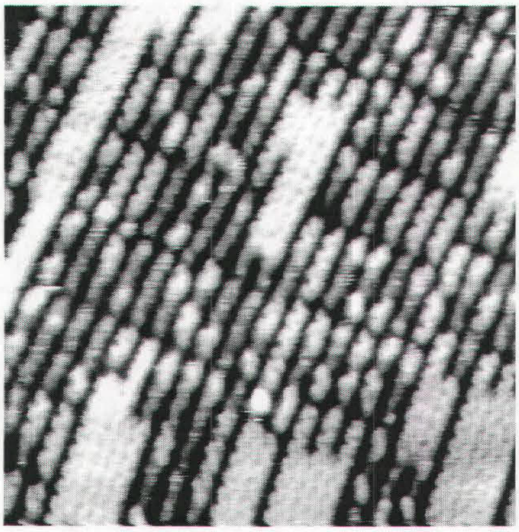

Figure 4.29: *Second reaction step at higher hydrogen pressure* ($p_{H2}=1\times10^{-6}$ *mbar). The reaction is limited by CO adsorption (brighter zig-zag protrusions) on the ending parts of the segments. Oxygen atoms in threefold sites are still present in the middle of the segments (darker zig-zag). Size:* 200×200 Å^2. ($I=0.76$ *nA*, $V_B=+0.41$ *V*).

Adsorption of other spurious species is possible (even though less probable). However oxygen diffusion, found when heating an O pattern, rules out a site-blocking effect.

A last hypothesis is related to the propagation mechanism. As already stated, the second reaction step usually involves an O vacancy diffusion mechanism for its propagation. The formation of an oxygen vacancy in the middle of a segment implies the breaking of the zig-zag sequence and the movement of a long chain of O atoms towards one end. It is reasonable that both the chain interruption and the correlated shift are sensitive to the temperature. Thus if not enough thermal energy is supplied, vacancies can not form in the internal part of the segments and the reaction can not proceed. Indeed in all our measurements at low temperature, we always saw O vacancies at the ends of the segments, never in the middle. As a consequence, only O atoms reachable by hydrogen atoms diffusing from the ends of the segment can be reacted off. This diffusion length upon the segments can be temperature dependent and this explains the different length of the reacted part at different temperatures. This mechanism justifies also the O island formation upon heating. When the pattern is heated, in fact, enough energy is supplied for the diffusion of oxygen chains but not for breaking the chain, i.e. for the formation of an O vacancy, which would result in quickly resuming the reaction.

A point that needs to be further investigated in this scenario is the reduced diffusion length for hydrogen on top of the segments, which is not expected for such a light, highly mobile species.

4.9 Conclusions

Influence of strain and segmentation on the reactivity of a metal surface have been studied at the oxide-like (10×2)-O/Rh(110) structure.
In this structure (Figure 4.30(a)), which grows on the (1×2) reconstructed substrate, the high oxygen coverage induces strain along the close packed metal rows. The interatomic distance along $[1\bar{1}0]$ is thus increased by 1/9 of the lattice constant and two rhodium atoms out of ten are ejected. This results in an ordered arrangement of segments composed by - on average - 8 rhodium atoms, with the ends aligned in the [001] direction. Oxygen atoms are bound on both sides of the segments in threefold sites which, due to the strain, become more and more distorted towards the ends of the segments. The ejected Rh atoms form small unreconstructed islands.

Catalytic oxidation of hydrogen has been investigated by taking STM movies during hydrogen exposure in the 238 K÷300 K temperature range.
The reaction starts on unreconstructed areas of the surface, which are an intrinsic byproduct of the formation of the structure. As shown by comparison with previous TPR measurements, the reactivity of the unreconstructed areas, which are covered by the (2×1)p2mg-O structure, is enhanced on the (10×2) surface. This is an example of modification of the reactivity of a structure due to the simultaneous presence on the surface of another structure.

The reaction proceeds in two steps, as shown in the overview in Figure 4.30, with completely different mechanisms. In the right part of the figure models reproduce the area in STM images on the left.
In a first stage a reaction front crosses the surface removing half of the oxygen, leaving the remaining atoms in a zig-zag fashion in threefold sites along the unstrained substrate segments (see Figure 4.30(b)). The propagation of the reaction front is anisotropic at RT (elongated in $[1\bar{1}0]$) but becomes isotropic at lower temperatures.
The strain removal in the first reaction step creates free adsorption sites for the dissociation of further H_2 molecules. This leads to the removal of the second half of oxygen in a second reaction step, which starts homogeneously all over the surface from the segment ends on (Figure 4.30(c)). This second step, much slower than the first, continues until a clean segmented (1×2) surface is produced (Figure 4.30(d)).
The initial surface for the second reaction step closely resembles the (2×2)p2mg-O structure, the only difference being the segmentation of metal rows. Comparing the reactivity of a pure (2×2)p2mg-O surface and of the (10×2), a large increase of the reactivity due to the segmentation is observed.

At low temperature (T<260 K), the effect of segmentation becomes more evident.
The reaction front propagates on unreconstructed areas, from where it enters the [001] channels created by the alignment of the segments. Because of the strain, the reaction cannot run along the whole length of each segment but stops after crossing the middle. Propagation in the parallel channel on the other end of the segments is needed for the completion of the first reaction step. Therefore a comb-like shape, due to the interplay between segmentation and strain, results for the reaction front.
A limited reactivity in the second reaction step leads to an oxygen nanopatterning with a number of remaining O atoms in the middle of each segment which can be tuned by changing

the reaction temperature. This is the first example, to our knowledge, of the formation of a nanopatterning on short 1D metal stripes by chemical reaction.

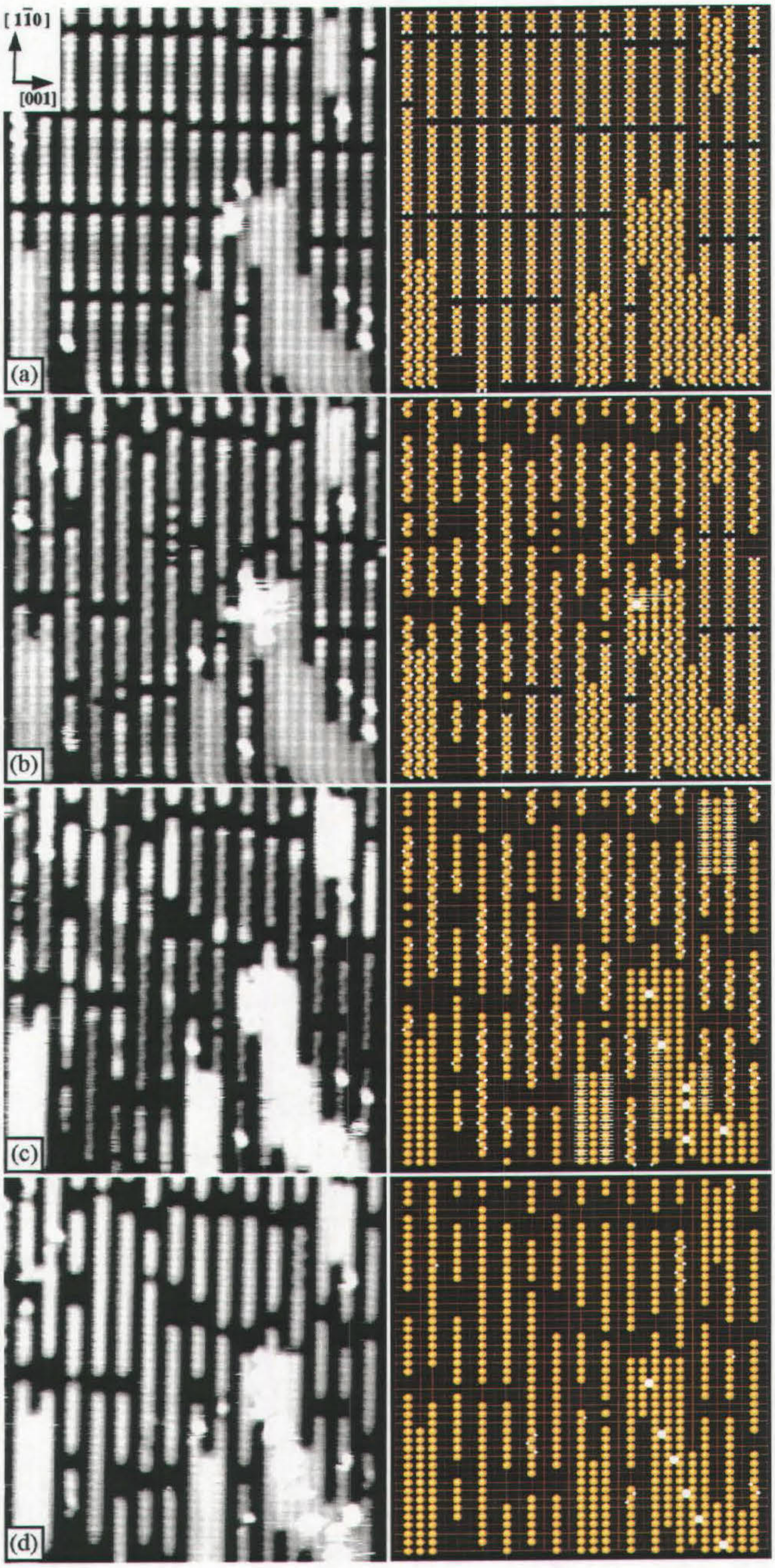

Figure 4.30: *Overview of the two step reactivity during catalytic oxidation of hydrogen on the (10×2)-O/Rh(110) surface (p_{H2} = 1×10^{-8} mbar, RT). Models on the right exactly reproduce the imaged area on the left. (a) Initial surface: strained segments of (10×2) periodicity and unreconstructed islands on a flat terrace. (b) In the first reaction step a wave front propagates over the surface (time needed to cross the imaged area: 4 images with 18 s/image), removing one O atom out of two and leaving the others in threefold sites in a zig-zag fashion. (c) Second reaction step proceeding from the segment ends via a vacancy diffusion mechanism all over the surface (reacted parts appear brighter). (d) Final clean, segmented (1×2) surface.*
Time between (a) and (b): 54 sec; between (b) and (c): 198 sec; between (c) and (d): 648 sec.
Size: 150×150 Å^2. (I=1.00 nA, V_B=+0.60 V).

Chapter 5

An Example of Supported Metal Catalyst: Nucleation and Growth of Au Nanoclusters on rutile TiO_2(110)

5.1 Introduction

A further step towards more realistic systems is the study of oxide supported metal catalysts.

In order to take up this field, up to now unexplored by our research group, I spent two months as a visiting student in the research group of Professor Flemming Besenbacher, at Aarhus University, Denmark. In Århus I participated in the study of the nucleation and growth of Au nanoclusters on TiO_2, a system that has attracted great interest in the recent years.

Oxide surfaces play a role in numerous applications. Actually the majority of industrial catalysts is supported on an oxide.

Titanium dioxide is used, for example, as a photocatalyst, for NO dissociation (when employed as a pigment in paints) or in solar cells, and for photo-assisted degradation of organic molecules.

Besides the wide range of its applications, TiO_2 is also well suited for many experimental techniques and serves as a model for other oxide and metal/oxide systems.

Gold has long been known as being catalytically far less active than other transition metals. In the last years, however, it was found that when dispersed as ultrafine particles and supported on metal oxides such as TiO_2, Au exhibits an extraordinary high activity for low-temperature catalytic combustion, partial oxidation of hydrocarbons, hydrogenation of unsaturated hydrocarbons and reduction of nitrogen oxides [62]. For example, Au clusters can promote the reaction between CO and O_2 to form CO_2 at temperatures as low as 40 K [63].

The catalytic properties of Au depend on the support, the preparation method and particularly the size of the Au clusters. The structure sensitivity of the low-temperature oxidation of CO on supported Au clusters on TiO_2(110), for example, manifests itself as a marked increase in the turnover frequency (the reaction rate per surface Au site per second) as the diameter of the Au clusters is decreased below ~3.5 nm (see Figure 5.1) [64,65,66]. Valden *et al.* proposed that this behaviour is correlated to a metal-to-nonmetal transition for clusters below this critical size, which was evidenced by STS (Scanning Tunneling Spectroscopy) measurements [64]. A further decrease in cluster diameter below ~3 nm leads to a decrease in the activity of the gold.

It is important to investigate the exact nature of metal/oxide bond not only to understand the growth mechanism of metal clusters but also to reveal the fundamental processes behind the catalytic activity of oxide-supported metal catalysts. It has recently been proved by DFT calculations for the Au/MgO system, that the oxide support may act as a structural promoter, offering low coordinated metal sites, but it can even interact with the adsorbates on the metal when these are close enough [67].

It has been speculated that surface defects may alter the electronic configuration of Au nanoparticles to enable catalytic reactions such as CO oxidation. Small Au clusters on MgO(100) have recently been shown, both experimentally and theoretically, to be active for CO oxidation only if the Au clusters nucleate at oxygen vacancies [68]. In this work the nucleation and growth of Au nanoclusters have been studied on the (110) surface of reduced rutile TiO_2, focusing particularly on the interaction with bridging oxygen vacancies, the most abundant surface defects.

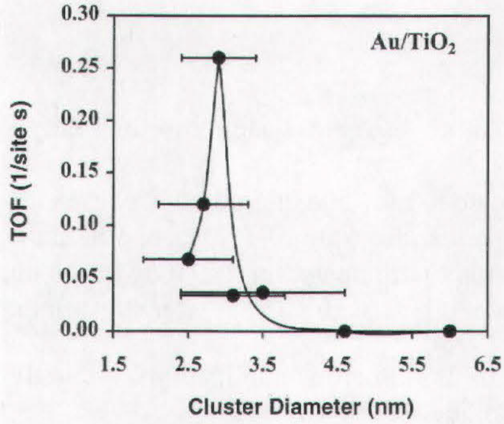

Figure 5.1: *CO oxidation turnover frequencies at 300 K as a function of the average size of the Au clusters supported on a high surface area TiO_2 support [64].*

5.2 The TiO_2(110) Surface

Titanium dioxide crystallises in three major different structures: rutile, anatase and brookite. However only rutile and anatase play any role in the applications of TiO_2 and are studied in surface science. In both structures, the basic building block consists of a titanium atom surrounded by six oxygen atoms in a more or less distorted octahedral configuration.
For rutile, the (110) surface, the one considered in this work, is the most stable crystal face.

Titanium dioxide is essentially not conductive but when reduced by high-temperature annealing in UHV, thus creating bulk oxygen vacancies or Ti interstitials, it exhibits semiconducting properties [69] and can therefore be quite easily imaged by STM.
Bulk reduction is reflected in a pronounced colour change of the crystal, which is initially transparent and becomes light and, eventually, dark blue.
Although the TiO_2(110) surface is very stable, it nevertheless modifies at high temperatures under oxidising conditions. Ti interstitials have a high diffusivity at elevated temperatures and when appearing at the surface they can react with gaseous oxygen and form additional TiO_2 structures. As shown in Figure 5.2, oxidation at moderate temperatures induces the formation of irregular networks of connected "rosettes", of (1×2) strands and of small (1×1) islands, while oxidation above 830 K leads to large, bulk terminated (1×1) terraces [70,71].

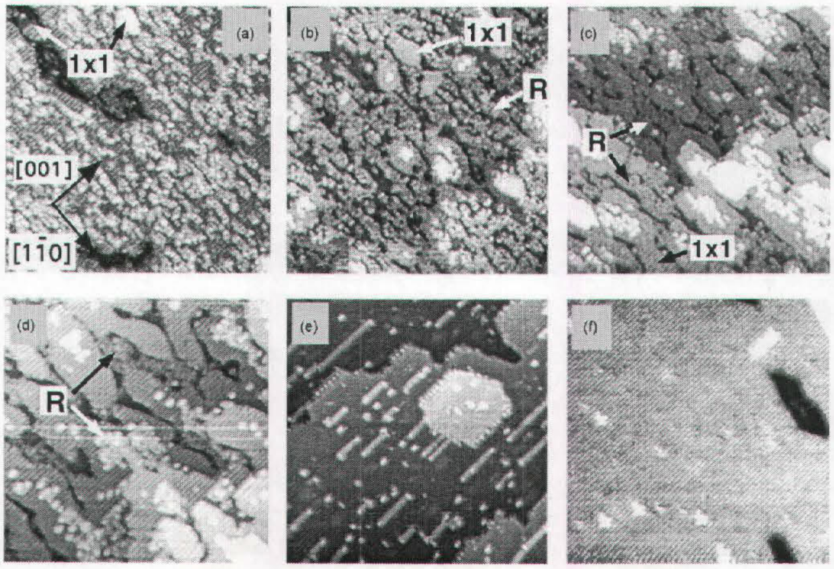

Figure 5.2: *TiO$_2$(110) surface restructuring after oxidation at different temperatures: (a) 500 K (b) 520 K; (c) 550 K; (d) 660 K; (e) 710 K; (f) 830 K [70].*

A schematic model of the surface, with protruding bridging oxygen rows, is proposed in Figure 5.3. Structural relaxations have been proved to lead to a rumpling of the surface [72]. STM images of TiO$_2$ are dominated by electronic effects [73]: mainly the Ti3d states are imaged when tunneling into the empty states even though O atoms protrudes for ~1 Å from the main surface plain [72]. As a consequence, the bridging oxygen rows appear darker, while the bright rows correspond to the 5-fold coordinated titanium atoms.

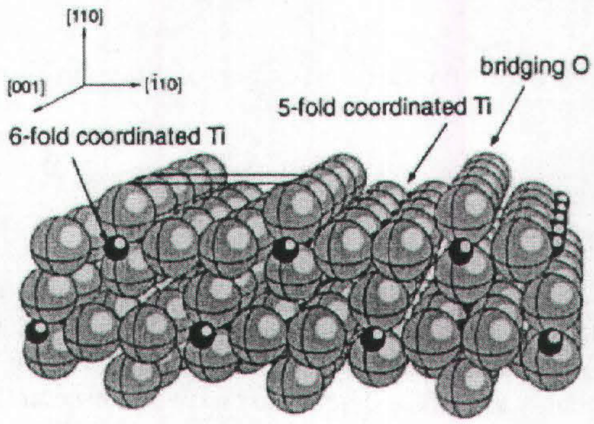

Figure 5.3: *Schematic model of bulk terminated TiO$_2$(110) surface. Grey, larger, spheres are O atoms, while dark, small, spheres represent Ti atoms [72].*

On the TiO_2 surface, point defects are easily created during the preparation of the sample. The presence of defects plays a crucial role in the surface properties [74]. The most common point defects are oxygen vacancies, which are created during the reduction of the sample. In STM images they appear as bright features, like the one marked by an arrow in Figure 5.4, on the dark rows. This kind of feature (commonly named type A defects) in STM images, however, corresponds also to hydroxyl groups. Two other kinds of point defects are often present (even though with a much lower coverage): type B, which appear as dark spots on the titanium rows and type C, characterised by bright round spots located on Ti rows [75]. The nature of both these defects is unclear.

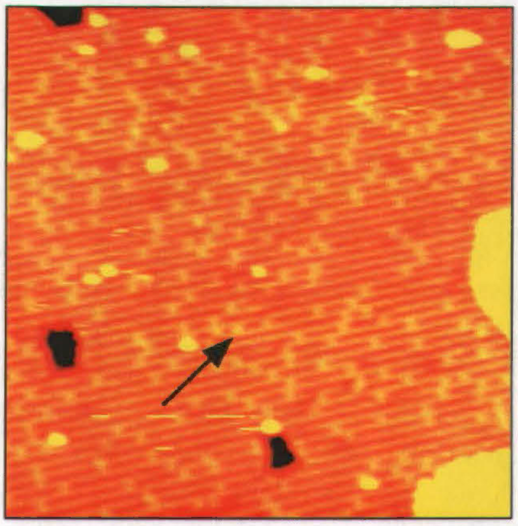

Figure 5.4: *STM image of the clean $TiO_2(110)$ surface; the arrow points to a single oxygen vacancy. Size: 300×300 Å^2.*

An exhaustive overview on the surface science of titanium dioxide can be found in ref. [76].

5.3 Au on TiO_2

The growth of gold clusters on the TiO_2 has been investigated using a variety of surface science techniques, including, for example, XPS and LEIS [77,78] and STM [79]. All these studies are reviewed in ref. [80]. As schematically indicated in Figure 5.5, in the initial stage Au clusters nucleate probably at surface defects and have 2D structures, which are frequently observed to be aligned between the oxygen rows of the surface [79]. Up to a coverage in the range of 0.1÷0.2 ML Au grows as quasi-2D clusters, one or two atomic layers in thickness. Further growth occurs via cluster thickening, with spherically shaped 3D clusters, with a large contact angle θ, that are formed at about 1 ML. The critical coverage, at which the growth switches to 3D, increases with decreasing temperature and with the defect density of the surface/sub-surface region [78]. It is thus clear that a detailed analysis of the influence of defects on the nucleation and growth of Au clusters on the TiO_2 is needed.

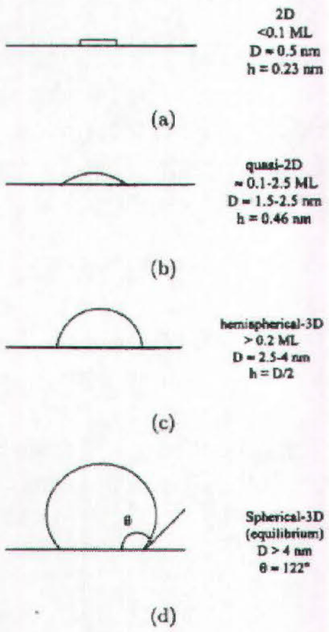

Figure 5.5: *Schematic representation of the change in cluster morphology as a function of Au coverage [80].*

5.4 Experimental

The experimental system is composed of a main UHV chamber and a high pressure cell (which hosts a high pressure STM), not used in this work [11].

The main chamber, base pressure $<10^{-10}$ torr, is equipped with several standard analysis techniques: AES, XPS, LEED and a mass spectrometer for gas analysis and TDS experiments. Nevertheless none of these instruments has been used in this work.

The UHV chamber also houses two home-built UHV STMs, one operating only at room temperature and the other at variable temperature. The latter, which is the one used in this work, can be cooled with liquid nitrogen, to reach temperatures of approximately 110 K, and heated with 75 V Zener diodes, up to 400 K.

Århus STMs are small, compact, very rigid and temperature compensated, yielding reduced sensitivity to mechanical and acoustic vibrations and temperature variations. The high eigenfrequency allows scanning down to a minimum acquisition time of 1 sec per image.

Sample preparation is facilitated by a fully automated system for cleaning by inert gas sputtering and annealing. This system consists of a differentially pumped sputter gun, a piezoelectric gas valve and a negatively biased Osram filament placed behind the sample for heating by radiation and electron bombardment. Cycles of sputtering and annealing are controlled by a home-built electronics and software package.

The TiO_2 sample was prepared by Ar^+ sputtering (30 min, 700 eV) and annealing first in oxygen pressure (5 min at 850-900 K, $p_{O2}=1\times10^{-6}$ torr) and then in UHV conditions (10-15 min at the same temperature). The idea of this treatment is that Ti interstials diffuse to the surface where they form small TiO_2 clusters. The basic result is to grow new layers of fresh material upon any defect, which leads to large fine terraces.

Au was deposited from an *e*-beam evaporator. The Au evaporation rate was quantitatively calibrated from STM measurements of Au deposited at 300 K on a Ni(111) surface to be 0.01 ML/min.

STM images were acquired at low current (<0.1 nA) in order to minimise the interaction between the clusters and the tip. In fact Au clusters bind only weakly to the stoichiometric surface and, as a consequence, they can be dramatically influenced by the scanning.

The Au/TiO_2(110) system has also been studied from the theoretical point of view, by N. Lopez and J.K. Nørskov, by means of DFT calculations and STM image simulations.

5.5 Nucleation

Figure 5.6(a) shows the clean TiO_2 surface. In the present context, the most important feature is the presence of the bright spots observed between Ti rows, like the one indicated by the square. As already stated, a similar signature can be assigned both to bridging oxygen vacancies and to bridging hydroxyl groups. The Århus-STM, however, has been proved to be able, due to its high lateral and vertical resolution, to distinguish between the two species (the latter originating from water dissociation at oxygen vacancies), which differ in their extent in the [001] direction (vacancy 6.6 Å, OH 4.8 Å), and in their apparent height (0.4 Å, 0.2 Å) [81]. In this work we can safely assign the bright spots between titanium rows to single oxygen vacancies. In Figure 5.6(a) also a few type B defects and a type C defect are present.

After gold deposition, Au clusters can be observed on the surface as brighter and larger spots (Fig. 5.6(b)-5.6(d)). The amount, the location and the size of the clusters depend on the deposition temperature. At the lowest temperature (130 K) (b), they are homogeneously distributed on the terraces and most of them contain only a few Au atoms. With increasing deposition temperature the average cluster density decreases and the average Au clusters size increases accordingly. At 210 K (c), the clusters are still distributed homogeneously on the terraces but contain on average 10 atoms at the same coverage of 0.04 ML of Au. Finally, at 300 K STM images (d) show that clusters are preferentially found at step edges and contain ~30 atoms (always at the same coverage).

The number of gold atoms per cluster is an average value calculated from the ratio between the coverage, as calibrated on the Ni(111) surface, and the average island density in the data set.

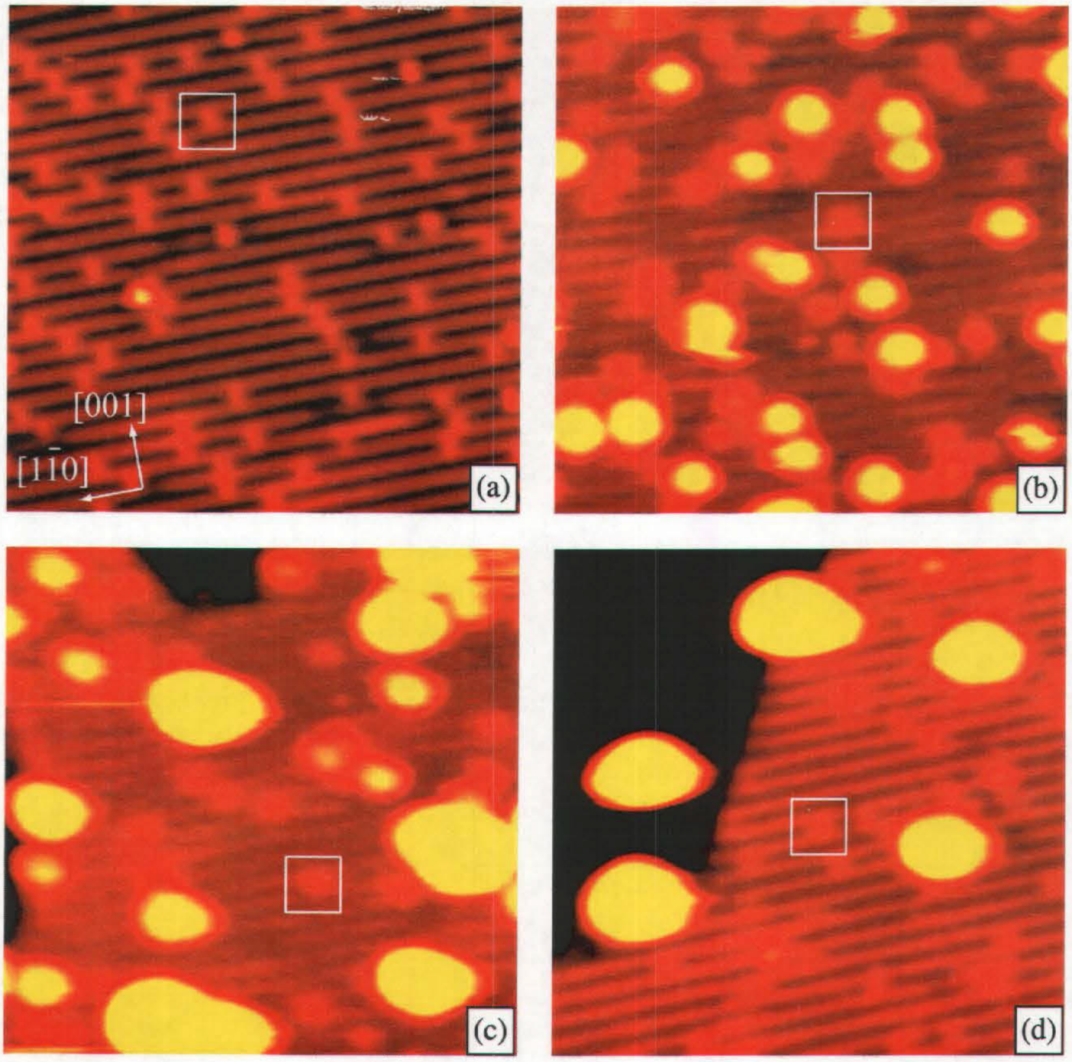

Figure 5.6: *The* $TiO_2(110)$ *surface before (a) and after 0.04 ML gold deposition at 130 K (b), 210 K (c) and 300 K (d). Vacancies are indicated by squares. Size: 150 × 150* $Å^2$.

We compared the number of oxygen vacancies before and after gold deposition with the number of clusters over many STM images (Figure 5.7). It turned out that, at all investigated temperatures, the density of vacancies decreases when Au is deposited. At the lowest temperature there is an almost 1:1 ratio between the decrease in O vacancies and the number of deposited clusters. At higher temperatures the decrease in the number of O vacancies is considerably larger, thus indicating that more than one O vacancy are trapped underneath each cluster. It is clear now that at all temperatures gold clusters bind to oxygen vacancies sites.

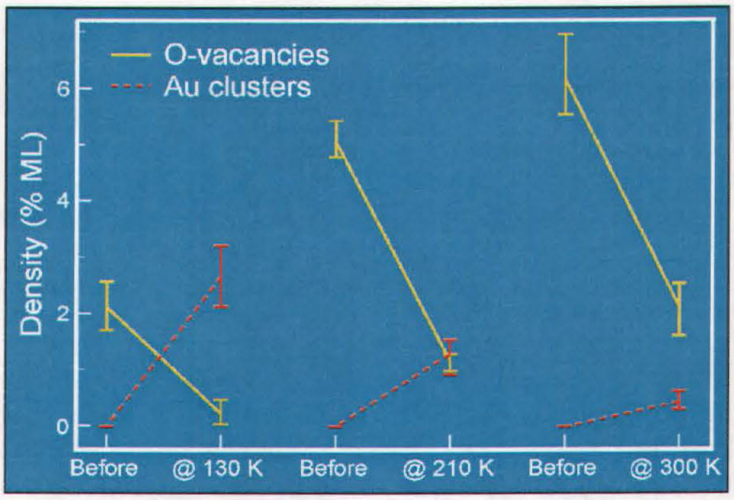

Figure 5.7: *Density of bridging oxygen vacancies and Au clusters before and after deposition of ~0.04 ML Au at different temperatures.*

By making careful statistics, it is possible to infer the number of gold atoms per cluster, the vacancy/cluster ratio and finally the number of Au atoms per vacancy for different deposition temperatures and gold coverages. As shown in the following table, the number of Au atoms per oxygen vacancy is roughly constant and equal to 3-5 in all cases.

Θ (ML)	T (K)	atoms/cluster	vac./cluster	atoms/vac.
0.005	125	2	1	2
0.005	300	7	2	3
0.02	151	5	1	5
0.04	130	5	1	5
0.04	210	9	3	3
0.04	300	28	9	3

Figure 5.8(a) presents a high resolution STM image of one of the smallest Au clusters. The protrusion is centred on a bridging oxygen row at the position where an O atom is expected. Moreover, simulated STM images reproduce exactly the smallest protrusions observed experimentally only if a single Au atom is placed at an oxygen vacancy site (Figure. 5.8(b) and 5.8(c)). DFT has been used to determine the binding site of Au on the stoichiometric and reduced surfaces. It has been found that gold is very weakly bound to the stoichiometric surface: a single Au atom binds by 1.55 eV and adsorption of a full Au monolayer is almost a thermoneutral process [82] (thus explaining the difficulty in imaging gold on the TiO_2 surface). For a single Au atom adsorption in an oxygen vacancy site is 0.45 eV more stable than on the most stable site on the stoichiometric surface and 0.80 eV more stable than adsorption on top of a fivefold coordinated titanium atom.

Thus the smallest protrusions in STM images can be unambiguously assigned to single Au atoms in O vacancy sites.

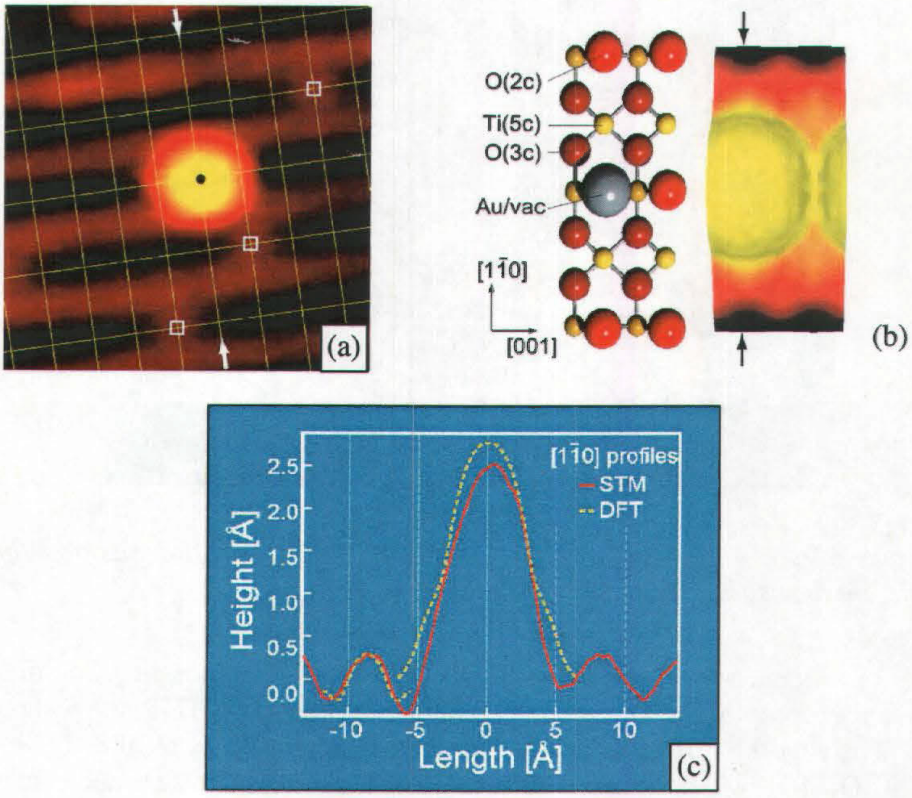

Figure 5.8: *Gold monomers: (a) STM image. The grid indicates the position of bridging O atoms, vacancies are marked with squares. (b) Simulated STM image of a single O atom trapped at a vacancy site. On the left a model of the surface unit cell used in the calculations. (c) Line profiles comparing theory and experiment.*

The gold-vacancy bond is covalent with a very small (if any) charge transfer.

5.6 Growth

The size distribution of gold clusters grown at different temperatures (plotted in Figure 5.9) gives the chance of analysing the mechanism of nucleation and growth of Au clusters in light of the strong Au-vacancy interaction. At low temperature the growth results in many small clusters, as was already evident in the image in Figure 5.6(a). When heating the surface, or depositing at RT, the clusters present a bimodal size distribution, with the presence of small and large clusters but with no evidence of medium-size ones.

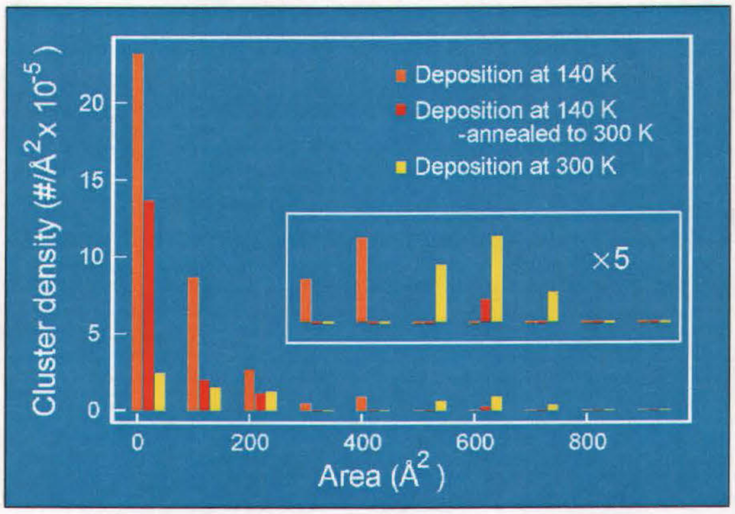

Figure 5.9: *Size distribution of Au clusters after 0.02 ML deposition for different deposition temperatures and annealing.*

The analysis of sequences of STM images indicates that there is not diffusion of single Au atom-O vacancy complexes at any investigated temperature. This suggests a growth mechanism involving the diffusion of clusters above a critical size, as already observed on amorphous Al_2O_3 [83], which collapse and form large clusters. Clusters nucleate at oxygen vacancy sites but upon further growth, a single vacancy can no longer stabilise the cluster and the cluster-vacancy complex will then diffuse. While diffusing it can encounter either another cluster or other surface defects. In the first case a larger cluster is formed that may continue to diffuse as well. If the cluster-vacancy complex encounters other oxygen vacancies, it can bind to them and will therefore stabilise on the surface. This nucleation and growth mechanism is schematically summarised in Figure 5.10. The fact that after annealing to (or when depositing at) RT the clusters are often located at step edges is not surprising, because step edges can be considered as a collection of oxygen vacancies.

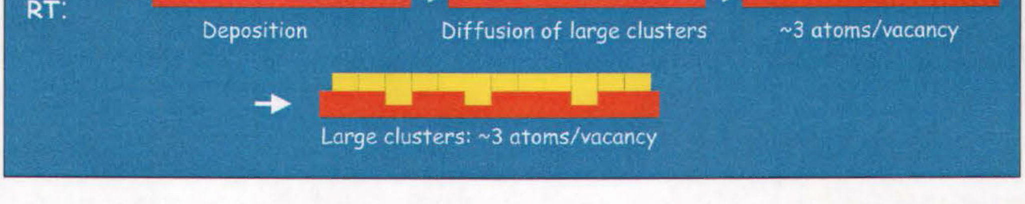

Figure 5.10: Nucleation and growth scheme at low temperature and at RT.

The critical cluster size for this growth mechanism can be estimated from the bimodal size distribution at RT: there is a minimum in the cluster population from approximately 250 Å^2 to 450 Å^2, which means clusters containing 5 to 7 Au atoms.
Conversely, clusters made of 3 to 5 atoms are stable. This finding correlates well with the average number of Au atoms per oxygen vacancy, deduced in the table in Figure. 5.8: 3 to 5 Au atoms attached to a single oxygen vacancy form a stable complex.

The stability of Au cluster-vacancy complexes has been studied also from the theoretical point of view. For small clusters the energy gain with increasing number of gold atoms attached to a single O vacancy has been calculated (see inset in Figure 5.11). There is a relative instability of a cluster containing two Au atoms compared to a single atom adsorbed on the oxygen vacancy and a diffusing Au atom, whereas a trimer is much more stable. A cluster composed of four Au atoms has an electronic configuration similar to a dimer [84], so it is expected to bind only weakly too.
For large clusters the number of gold atoms stabilised per vacancy has been estimated, within a very simplified model, by comparing a monolayer cluster (represented by a disk attached to a varying number of vacancies) to a 3D cluster (represented by a sphere) on the stoichiometric surface. In Figure 5.11 solid lines show the energy for the Au disk adsorbed on the indicated number of vacancies, while dashed lines show the limit for diffusion (transition to spherical 3D clusters). If there are no vacancies attached to the Au cluster, a 3D cluster is always the most stable configuration but if vacancies are included a 2D island up to a certain size will be more stable than a 3D cluster. The intersection between the two lines gives the maximum number of Au atoms stabilised by a certain amount of O vacancies. The situation for 5 and 10 vacancies trapped underneath the cluster are indicated: in both cases the maximum number of Au atoms per vacancy that can be stabilised in a disk-like structure is about 3, which again is in nice agreement with the previously stated conclusions.

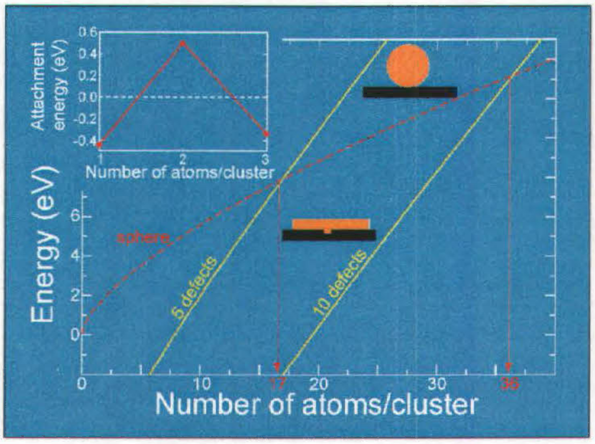

Figure 5.11: *Transition between adsorption on vacancies and diffusion (see text). In the inset: attachment energy for Au_n ($n=1 \div 3$) clusters on a single vacancy.*

5.7 Conclusions

Through an interplay between Scanning Tunneling Microscopy and DFT calculations it has been demonstrated in this work that gold clusters nucleate at oxygen vacancy sites. A single Au atom-O vacancy complex is stable on the surface at all investigated temperatures (up to room temperature). On average a single O vacancy binds three Au atoms. Larger clusters are bound to more than one vacancy, thus resulting in a high density of O vacancies in the Au-substrate interface

A new growth mechanism has been proposed. Au atoms deposited at low temperature bind to O vacancies and form homogeneously distributed Au clusters that are stable on the surface. When annealing to 300 K or depositing at this temperature, Au cluster-O vacancies complexes over a certain critical size are no more stable and diffuse on the surface until they find another cluster or other vacancies. In the former case they collapse and form larger clusters that may diffuse as well. Conversely, if diffusing clusters encounter other oxygen vacancies, they trap the new vacancies underneath them and, if the ratio Au atoms/O vacancy is in the suitable range (about 3), they can be stabilised. This growth mechanism leads to a bimodal cluster size distribution, in agreement with experimental findings. The critical size for diffusion has been estimated to be ~250 $Å^2$, which corresponds to approximately 5-7 atoms per vacancy.

Reference:

"Bonding of Gold Nano-Clusters to Oxygen Vacancies on Rutile $TiO_2(110)$"
E. Wahlström, N. Lopez, R. Schaub, P. Thorstrup, A. Rønnau, C. Africh, E. Lægsgaard, J.K. Nørskov and F. Besenbacher
Phys. Rev. Lett. **90**, 2 (2003) 026101

Chapter 6

The Fast STM Project: 1000 Times Faster

6.1 Introduction

As seen in the previous chapters, the study of dynamic phenomena (such as surface reactions) by STM is often limited by the time resolution of the instrument. Many processes of interest, in fact, develop on the time scale of hundreds of milliseconds or below, thus it is not possible to follow their details if tens of seconds are needed for the acquisition of a single image: only the final stage of the dynamic processes can be revealed.

In surface science this problem is usually sidestepped by decreasing the temperature, thus slowing down the process. This solution, however, is sometimes misleading, because a process can follow different pathways at different temperatures, when the pathways have different activation energies. Lowering the temperature changes thus dramatically the selectivity. Moreover some processes linked to a critical temperature, like nucleation, do not occur at all at low temperature.

As a consequence surface science studies are often far away from real systems, which occur at higher temperatures.

For this reason there is a strong interest in developing new setups, capable of improving the experimental time resolution.

In Scanning Tunneling Microscopy this problem has been tackled by a few research groups in the last years and acquisition times down to ~15 msec/image have been achieved [85,86].

A project for the development of a Fast STM module is presently under way also in our group, in collaboration with the Instrumentation and Detector Laboratory of ELETTRA. Whereas previous groups built ad hoc STMs with high eigenfrequencies (EF), scanning at frequencies below the first EF, our approach is to use our commercial STM at frequencies between and above EFs of the instrument.

In the following the main general features of a Fast STM will be introduced together with the main problems one has to deal with. Then our Fast STM module will be presented: its architecture will be described and first promising results shown. Finally an outlook on present and future developments and first possible applications will be given.

6.2 How Does a Fast STM Work?

The scanning speed of an STM is first of all limited by the feed-back circuit. Therefore, if fast image acquisition is desired, the feed-back has to be slowed down. This means that Fast STM images are acquired in "Constant Height" mode. As pointed out in Chapter 1, when working in "Constant Height" mode the vertical position of the tip is kept constant and variations in the tunneling current are monitored. This measuring mode requires usually rather flat surfaces in order to avoid tip crashes.

The tip is scanned in plane along a fast direction (X), with frequencies up to 10 kHz, and simultaneously along a slow direction (Y), with frequencies up to 40 Hz (Figure 6.1), by variation of the potential applied to the piezo tube. Images, typically made of ≤200 × ≤200 data points, are thus acquired with a maximum frame rate of 40 images per second (i.e. minimum acquisition time 25 msec/image).
While the slow direction movement is excited with a triangular or a saw-tooth wave, the movement in the fast direction is modulated by a sinusoidal wave. A triangular wave (or even worse a saw-tooth wave), in fact, would result in a sharp change of direction at the ends of each line and this generally excites mechanical resonances. A sinusoidal wave, though, has the disadvantage of introducing a distortion in the images, which has to be corrected by the visualisation software.
Data acquisition is synchronised with the scanning excitation, so that the tunneling current is measured at constant time intervals while scanning always in the same direction (i.e. always forward or always backward) as shown in Figure 6.2.

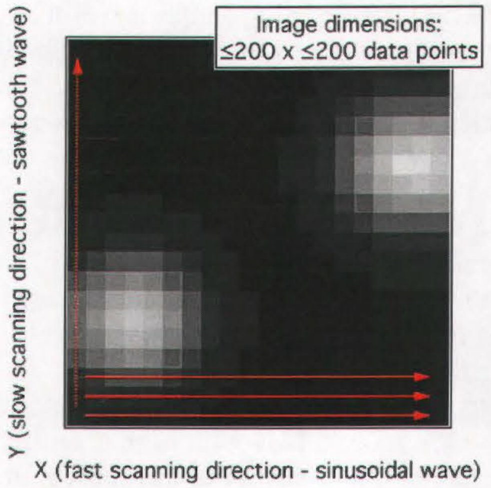

Figure 6.1: *Scheme of a Fast STM image. The tip is moved in plane along a fast direction (X) and a slow direction (Y).*

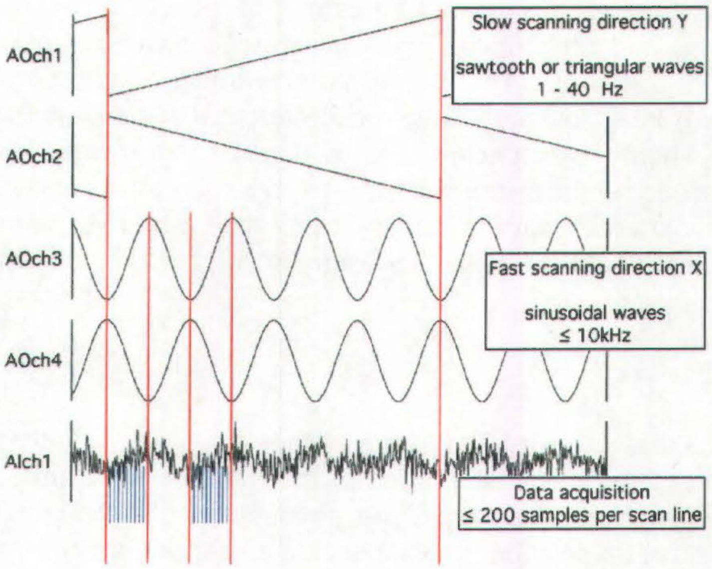

Figure 6.2: *Fast STM control scheme. The +Y/-Y quadrants of the scanner tube are excited with a saw-tooth wave, while for the +X/-X quadrants a sinusoidal wave is used. Data acquisition is synchronised with the scanning.*

The number of samplings is limited by the fast response of the preamplifier (high cut-off frequency needed) and by computer performances and a maximum data rate of ~1 Msamples/sec can be achieved.
This limitation reflects in the maximum number of acquired data points per image at a fixed image rate. On large scale images this number of data points per image may be not high enough to discern between adjacent topographic features. Moreover wide scanning areas lead to problems in the current measurement: since the tunneling current depends exponentially on the tip-sample distance, the inclination of the sample provokes that at larger image sizes the more distant parts of the surface are no more resolved. A Fast STM measurement, thus, is a compromise between lateral resolution (due to the data point per image number) and size of the imaged area. Obviously wider area images with higher lateral resolution are still accessible but at lower scanning frequency, i.e. with longer acquisition time.

One of the major problems when working with a Fast STM is related to mechanical resonances, which depend on the particular experimental setup. In each single case, therefore, a detailed study of all resonances teaches which scanning frequencies, even though accessible by the instrument, cannot be used. In STMs already built for a Fast use, this problem is limited by constructing a scanner with high eigenfrequencies and measuring below these EFs [87].

6.3 Our Fast STM Module

The Instrumentation and Detector Laboratory of ELETTRA, directed by Riccardo Tommasini, developed, in collaboration with our group, a Fast STM module which can be inserted in the original Omicron system between the control unit and the STM system.
A straightforward advantage of the modular architecture is that it does not modify the original system. One can switch between acquisition modes and still image the same area of the sample. The performance of the instrument for slow measurements is not altered.
Moreover, the modular architecture will allow using the Fast STM Control Module also in combination with other STMs and with other scanning techniques based on a local probe.

6.3.1 Architecture

The basic idea is that the Fast STM Control Module controls only the lateral position of the tip by variation of the potential applied to the four XY quadrants of the single tube scanner and acquires current data from a fast preamplifier. All the remaining tasks of the control system (vertical tip position, thermal drift, etc.) are performed by the standard STM Control Unit of our commercial Omicron VT-STM.

Potentials generated by the Fast STM Control Module are simply added to the Omicron Control Unit outputs by means of four APEX-type high voltage operational amplifiers and delivered to the piezo.

Figure 6.3 shows the architecture of the Fast STM module.

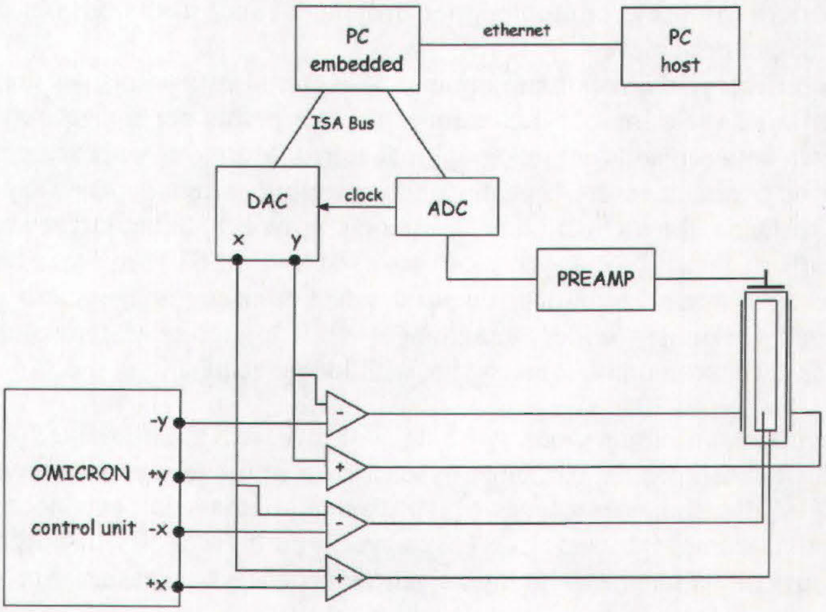

Figure 6.3: *Architecture of the Fast STM Module. Potentials generated by the Fast Control Module are added to Omicron outputs and delivered to the piezo. The tunneling current is in turn acquired (by means of a fast preamplifier) and processed by the Fast Control Module.*

An Embedded PC (controlled via Ethernet connection by a Host PC) contains a DAC (Digital to Analog Converter) board and an ADC (Analog to Digital Converter) board. The communication between the embedded PC and the two boards is based on ISA Bus technology. The DAC board generates the modulations which have to be superimposed to the potential applied to the piezo. These signals are added to Omicron outputs (±X and ±Y) by means of four APEX operational amplifiers and delivered to the piezo tube. The tunneling current is acquired by the preamplifier and processed by the ADC board, which also acts as a clock for the DAC board, i.e. for synchronisation between scanning and data acquisition.
The host PC allows transforming current data in images by means of a home-made visualisation software [88].

For a fast current acquisition it has been necessary to use a fast preamplifier. The original Omicron VT PRE E amplifier, in fact, has a cut-off frequency of only ~10 kHz.

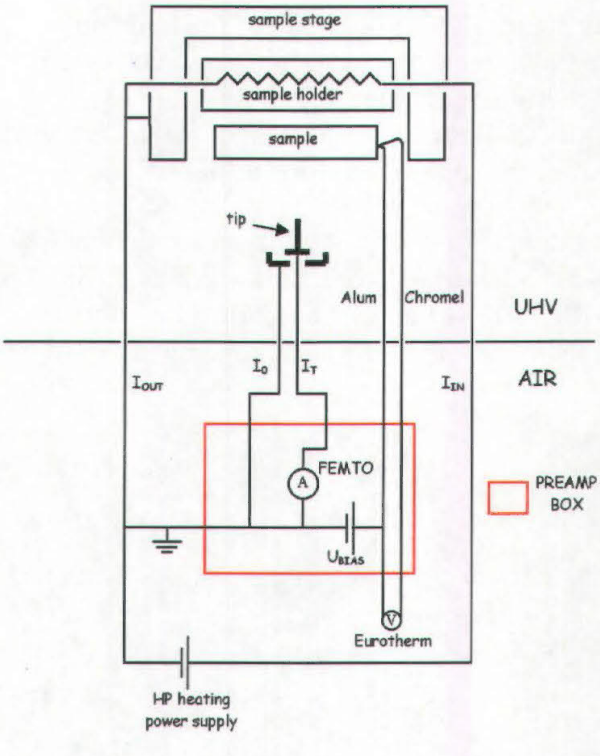

Figure 6.4: *New preamplifier box. A FEMTO preamplifier allows fast current acquisition. The bias potential is applied to a thermocouple wire and thus delivered to the sample while the tip is at ground potential.*

A FEMTO DLPCA 100 preamplifier has been chosen because of its 200 kHz cut-off frequency (at 10^8 amplification). Moreover this preamplifier allows fast switching between a "low noise" mode, which permits to take slower images with high resolution, and a "high speed" mode for Fast measurements. In this configuration, though, it is no more possible to apply the bias potential to the tip, as in the Omicron system (see Section 2.3). Therefore it was necessary to find a way to deliver the bias to the sample, which conversely is at ground potential in the Omicron setup. Our solution is to use the thermocouple contacts, which we previously introduced for reading the sample temperature during measurements (see Section 2.4.3). A preamplifier box has been constructed (see Figure 6.4), which accommodates the FEMTO, for acquisition of the tunneling current I_T as referred to the screen value I_0, and delivers the bias voltage, generated by the Omicron Control Unit, to the alumel thermocouple wire. Thermocouple outputs allow connection to an Eurotherm controller for temperature reading.

The setup with the new preamplifier and an improved cable screening allowed noise reduction up to a factor of 50 in the "low noise" mode and "high speed" measurements with absence of discrete frequencies in the range of 1÷50 kHz. It has been tested on metal surfaces at slow scanning speed (typical Omicron image rate) and it was found to be still capable of atomic resolution, without any influence on the overall Omicron performance.

6.3.2 First Fast Results

The system has been successfully tested on the rhodium surface. It has been evidenced that even though working in a frequency range were resonances are present, series of images can be acquired without loosing resolution.

A maximum frame rate of 200 Hz (i.e. 5 msec/image) for images made of 50×50 data points (on 70×210 Å^2 wide areas of the surface) has been achieved.

Figure 6.5 shows an example of a series of images acquired at 670 K with 25 msec/image with 50×70 data points on a 50×50 Å^2 wide surface area. In the upper left corner of the images the c(2×6)-O/Rh(110) structure transforms into the (2x2)p2mg structure (see Section 3.2 for description of both structures) upon hydrogen exposure.

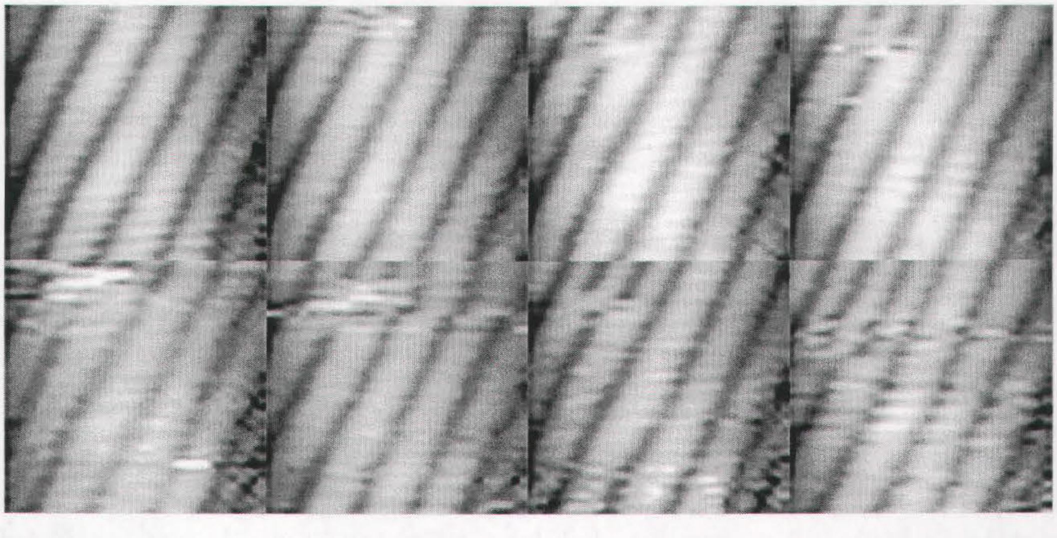

Figure 6.5: *Fast STM series of images of the deconstruction of the c(2×6)-O/Rh(110) surface (see upper left corner) at 670 K upon hydrogen exposure ($p_{H2}=1\times10^{-8}$ mbar). Size: 50×50 Å^2; 50×70 data points. Acquisition time: 25 msec/image.*

6.4 Outlook

As evidenced in the previous paragraph, with the Fast STM Module it is already possible to acquire series of STM images with up to 200 Hz frame rate.
A detailed study of the effect of mechanical resonances on STM images [89] is permitting to precisely determine which scanning frequencies can be applied without any distortion in the images.

The system will then be used in a real experiment.
The studies presented in the previous chapters already suggest two possible test systems:

- The water formation reaction on the (2×1)p2mg-O/Rh(110) surface.
  The reaction (see Chapter 3) propagates as a wave front on the initial surface quickly removing half oxygen atoms and leaving behind the others in a c(2×4) structure. Then the reaction proceeds via the formation of stable OH islands, which grow at the expense of the c(2×4)-O and finally contract due to the formation and the desorption of water molecules from their borders.
  The reaction mechanism in the second part of the reaction seems thus already quite clear. But what happens during the first part of the reaction? How do OH groups behave?
  Fast STM movies will allow to follow the first part of the reaction and hopefully to image OH also in this step.
  Moreover it will be possible to study the reaction also at higher temperatures, where it is much faster and thus presently not accessible. An increase in the reaction temperature might result in a different reaction mechanism, because OH islands can no more be stable on the surface above the desorption temperature.
- The water formation reaction on the (10×2)-O/Rh(110) surface.
  The reaction (see Chapter 4) proceeds in two distinct steps. In a first step a reaction front propagates on the surface removing half of the initial oxygen coverage concomitantly to the strain, while the second half of oxygen is reacted off in a second reaction step with a completely different mechanism.
  Measurements at low temperature evidenced a particular propagation mechanism for the reaction front, which assumes a comb-like shape, that was not found at room temperature. Does the reaction front propagate with the same mechanism also at RT but on a faster time scale?

In the future we plan to implement in the Fast STM Module also an option for "atom tracking", which is a technique allowing to lock the tip on top of a feature and follow its movement on the surface [90]. This further improvement will permit to study diffusion and rotational processes.

Chapter 7

Summary

Three selected examples of the use of Scanning Tunneling Microscopy in the study of model catalysts for oxidation reactions have been reported.

It has been demonstrated how this technique allows elucidating at the atomic scale the details of structures and reaction mechanisms.

A route from a very simplified model catalyst through more complicated systems permitted to make a step towards more realistic conditions. A further step on this way will be the Fast STM module, an add-on system presented in the last chapter, which will allow investigations at a three orders of magnitude faster time scale, making accessible temperatures where the phenomena of interest evolve extremely fast.

The first, simplest, model catalyst presented in this work was the unreconstructed (110) surface of rhodium. The catalytic oxidation reaction of hydrogen on the (2×1)p2mg-O covered surface has been studied by taking STM movies (with acquisition time down to ~20 sec per image) during hydrogen exposure.

It has been possible to determine the fine reaction mechanism, with the formation of intermediate reaction products.

The reaction was found to nucleate at defects and propagate to the whole surface as a wave front. Behind the front, half of the initial oxygen atoms are still present, adsorbed in short bridge sites and rearranged in a c(2×4) structure, which homogeneously covers the surface. At this point steady-state OH islands, with c(2x2) symmetry, form, which grow at the expense of the c(2×4)-O structure until covering half of the surface. OH islands then contract, due to water formation and desorption from their borders.

In the second example, the catalytic oxidation of hydrogen has been investigated again but this time starting from the (10×2)-O structure, which is a metastable oxide-like structure characterised by the presence of strain and segmentation.

The same metal surface, Rh(110), thus, behaves as a more or less complicated system according to the initial structure formed by adsorbates and gives the possibility of selectively studying the influence of modifications of the first layer of a metal surface on its reactivity. This makes this second example of catalyst a first step towards more realistic systems.

The water formation reaction on the (10×2)-O/Rh(110) surface was found to be a two step reaction: in the first step only half of the initial oxygen coverage is removed by a reaction front, which propagates on the surface leaving behind oxygen atoms in threefold sites in a zig-zag fashion. The concomitant removal of the strain (due to the high local O coverage) opens the opportunity for a completely different mechanism for the removal of the second half of oxygen in a slower second reaction step, which starts homogeneously all over the surface and proceeds from segment ends on.

Both reaction steps, as well as the beginning of the reaction, have been characterised in detail, highlighting the role of strain and segmentation on reactivity.

At low temperature the influence of segmentation and its interplay with strain was found to be even clearer. Segmentation and strain have been proved to lead to a particular propagation mechanism for the reaction front, with a comb-like shape. It has finally been demonstrated that segmentation can be exploited for the creation of a precise oxygen nanopatterning on 1D metal stripes, with a tunable number of O atoms.

The last example was a supported metal catalyst. Most industrial catalysts are supported on an oxide, thus this third system is a concrete step towards real catalysis.
The nucleation and growth of gold nanoclusters on rutile $TiO_2(110)$ have been studied in collaboration with the research group of professor Flemming Besenbacher in Århus. Due to the high resolution and stability of the Århus STM, it has been possible to correlate the formation of gold clusters with the presence of oxygen vacancies, which are the most abundant point defects of this surface. On average, a single O vacancy binds three gold atoms, while more vacancies are trapped underneath larger clusters.
A new growth mechanism has been proposed. Gold deposition at low temperature results in the formation of stable clusters at oxygen vacancies, homogeneously distributed on the surface. Conversely, when depositing at room temperature, or annealing to this temperature after deposition at low T, Au cluster/O vacancy complexes above a critical size diffuse on the surface until they meet another Au/vacancy complex, which leads to coalescence, or until they meet other oxygen vacancies, which are in turn trapped underneath the cluster. When an average Au atoms/O vacancies ratio of three is achieved, Au/vacancy complexes are stabilised on the surface. This growth mechanism leads to a bimodal size distribution which was indeed evidenced in the STM images.

Bibliography

[1] G. Comelli, V.R. Dhanak, M. Kiskinova, K.C. Prince and R. Rosei, Surf. Sci. Rep. **32**, 165 (1998)

[2] B. Hammer and J.K. Nørskov, Adv. Cat. **45**, 71 (2000)

[3] J. Tersoff in *Scanning Tunneling Microscopy and Spectroscopy* (VCH Publishing, 1993)

[4] C. Chen, *Introduction to Scanning Tunneling Microscopy* (Oxford University Press, 1993)

[5] J. Tersoff and DR. Hamann, Phys. Rev. Lett. **50**, 1998 (1983)

[6] J. Bardeen, Phys. Rev. Lett. **6**. 57 (1961)

[7] L. Ruan, F. Besenbacher, I. Stensgaard and E. Lægsgaard, Phys. Rev. Lett. **70**, 4079 (1993)

[8] N.D. Lang, Phys. Rev. Lett. **56**, 1164 (1986)

[9] I.S. Tilinin, M.K. Rose, J.C. Dunphy, M. Salmeron and M.A. Van Hove, Surf. Sci. **418**, 511 (1998)

[10] G. Doyen, D. Drakova, E. Kopatzi and R.J. Behm, J. Vac. Sci. Technol. A **6**, 327 (1988)

[11] E. Lægsgaard, L. Österlund, P. Thostrup, P.B. Rasmussen, I. Stensgaarg and F. Besenbacher, Rev. Sci. Instrum. **72**, 3537 (2001)

[12] F.M. Liebsle, P.W. Murray, S.M. Francis, G. Thornton and M. Bowker, Nature **363**, 706 (1993)

[13] C. Castellarin Cudia, Saw Wai Hla, G. Comelli, Z. Sljivancanin, B. Hammer, A. Baraldi, K.C. Prince and R. Rosei, Phys. Rev. Lett. **87**, 196104 (2001)

[14] C. Africh, F. Esch, G. Comelli and R. Rosei, J. Chem. Phys. **116**, 7200 (2002)

[15] J.W. Döbereiner, Schwigg. J. **39**, 1 (1823)

[16] J.J. Berzelius, Jber. Chem. **15**, 237 (1837)

[17] G. Comelli, V.R. Dhanak, M. Kiskinova, G. Paolucci, K.C. Prince and R. Rosei, Surf. Sci. **269/270**, 360 (1992)

[18] C. Comicioli, V.R. Dhanak, G. Comelli, C. Astaldi, K.C. Prince, R. Rosei, A. Atrei and E. Zanazzi, Chem. Phys. Lett. **214**, 438 (1993)

[19] V.R. Dhanak, K.C. Prince, R. Rosei, P.W. Murray, F.M. Leibsle, M. Bowker and G. Thornton, Phys. Rev. B **49**, 5585 (1994)

[20] P.W. Murray, F.M. Leibsle, Y. Li, Q. Guo, M. Bowker, G. Thornton, V.R. Dhanak, K.C. Prince and R. Rosei, Phys. Rev. B **47**, 12976 (1993)

[21] E. Vesseli, C. Africh, A. Baraldi, G. Comelli, F. Esch and R. Rosei, J. Chem. Phys. **114**, 4221 (2001)

[22] G. Comelli, V.R. Dhanak, M. Kiskinova, N. Pangher, G. Paolucci, K.C. Prince and R. Rosei, Surf. Sci. **260**, 7 (1992)

[23] M. Gierer, H. Over, G. Ertl, H. Wohlgemuth, E. Schwarz and K. Christmann, Surf. Sci. Lett. **297**, L73 (1993)

[24] J.D. Batteas, A. Barbieri, E.K. Starkey, M.A. Van Hove and G.A. Somorjai, Surf. Sci. **339**, 142 (1995)

[25] D. Alfè, P. Rudolf, M. Kiskinova and R. Rosei, Chem. Phys. Lett. **211**, 220 (1993)

[26] G. Comelli, A. Baraldi, S. Lizzit, D. Cocco, G. Paolucci, R. Rosei and M. Kiskinova, Chem. Phys. Lett. **261**, 253 (1996)

[27] S.W. Hla, P. Lacovig, G. Comelli, A. Baraldi, M. Kiskinova and R. Rosei, Phys. Rev. B **60**, 7800 (1999)
[28] F. Bondino, G. Comelli, A. Baraldi and R. Rosei, Phys. Rev. B, **66**, 0754022 (2002)
[29] J.E. Whitten and R. Gomer, Surf. Sci. **409**, 16 (1998)
[30] T. Mitsui, M.K. Rose, E. Fomin, D.F. Ogletree and M. Salmeron, Surf. Sci. **511**, 259 (2002)
[31] M. Schick, J. Xie, W.J. Mitchell and W.H. Weinberg, J. Chem. Phys. **104**, 7713 (1996)
[32] D. Kolovos-Vellianitis, T.Kammler and J. Küppers, Surf. Sci. **482-485**, 166 (2001)
[33] S. Völkening, K. Bedürftig, K. Jacobi, J. Wintterlin and G. Ertl, Phys. Rev. Lett. **83**, 2672 (1999)
[34] C. Sachs, M. Hildebrand, S. Völkening, J. Wintterlin and G. Ertl, Science **293**, 1635 (2001)
[35] C. Sachs, M. Hildebrand, S. Völkening, J. Wintterlin and G. Ertl, J. Chem. Phys. **116**, 5759 (2002)
[36] L. Gregoratti, A. Baraldi, V.R. Dhanak, G. Comelli, M. Kiskinova and R. Rosei, Surf. Sci. **340**, 205 (1995)
[37] C. Africh, F. Esch, G. Comelli and R. Rosei, J. Chem. Phys. **115**, 477 (2001)
[38] A. Baraldi, V.R. Dhanak, G. Comelli, K.C. Prince and R. Rosei, Surf. Sci. **293**, 246 (1993)
[39] P.A. Thiel and T.E. Madey, Surf. Sci. Rep. **7**, 211 (1987)
[40] J. Jupille, J. Fusy and P. Pareja, Surf. Sci. **91**, 187 (1980)
[41] K. Bange, D.E. Grider, T.E. Madey and J.K. Sass, Surf. Sci. **137**, 38 (1984)
[42] E. Stuve, S.N. Jorgensen and R.J. Madix, Surf. Sci. **146**, 179 (1984)
[43] M. Canepa, P. Cantini, L. Mattera, M. Salvietti and S. Terreni, Surf. Sci. **322**, 271 (1995)
[44] M. Canepa, P. Cantini, E. Narducci, M. Salvietti, S. Terreni and L. Mattera, Surf. Sci. **343**, 176 (1995)
[45] K.D. Gibson, M. Viste and S.J. Sibener, J. Chem. Phys **112**, 9582 (2000)
[46] K. Bedürftig, S. Völkening, Y. Wang, J. Wintterlin, K. Jacobi and G. Ertl, J. Chem. Phys. **111**, 11147 (1999)
[47] T. Mitsui, M.K. Rose, E. Fomin, D.F. Ogletree and M. Salmeron, Science **297**, 1850 (2002)
[48] E. Vesselli, Laurea Thesis (1999)
[49] H. Over, Y.D. Kim, A.P. Seitsonen, S. Wendt, E. Lundgren, M. Schmid, P. Varga, A. Morgante and G. Ertl, Science **287**, 1474 (2000)
[50] M. Mavrikakis, B. Hammer and J.K. Nørskov, Phys. Rev. Lett. **81**, 2819 (1998)
[51] M. Gsell, P. Jakob and D. Menzel, Science **280**, 717 (1998)
[52] V. Pallassana and M. Neurock, J. Cat. **191**, 301 (2000)
[53] P. Jakob, M. Gsell and D. Menzel, J. Chem. Phys. **114**, 10075 (2001)
[54] Y. Xu and M. Mavrikakis, Surf. Sci. **494**, 131 (2001)
[55] S. Sakong and A. Groß, Surf. Sci. **525**, 107 (2003)
[56] W.X. Li and B. Hammer, private communication
[57] F. Esch, unpublished
[58] F. Mertens, R. Imbihl, Chem. Phys. Lett. **242**, 221 (1995)
[59] A. Makeev, R. Imbihl, J. Chem. Phys. **113**, 3854 (2000)
[60] Q. Zhang, S. Tang and R.M. Wallace, Appl. Surf. Sci. **172**, 41 (2001)
[61] M.E. Franke and U. Simon, Sol. St. Ion. **118**, 311 (1999)
[62] M. Haruta, Catal. Today **36**, 153 (1997)

[63] H. Huber, D. McIntosh and G.A. Ozin, Inorg. Chem. **16**, 975 (1977)
[64] M. Valden, X. Lai and D.W. Goodman, Science **281**, 1647 (1998)
[65] M. Haruta, S. Tsubota, T. Kobayashi, H. Kageyama, M.J. Genet and B. Delmon, J. Catal. **144**, 175 (1993)
[66] G.R. Bamwenda, S. Tsubota, T. Nakamura and M. Haruta, Catal. Lett. **44**, 83 (1997)
[67] L.M. Molina and B. Hammer, Phys. Rev. Lett. **90**, 206102 (2003)
[68] A. Sanchez, S. Abbet, U. Heiz, W.D. Schneider, H. Häkkinen, R.N. Barnett, and U. Landman, J. Phys. Chem. A **103**, 9573 (1999)
[69] D.C. Cronemeyer, Phys. Rev. **87**, 876 (1952)
[70] M. Li, W. Hebenstreit, L. Gross, U. Diebold, M.A. Henderson, D.R. Jennison, P.A. Schultz and M.P. Sears, Surf. Sci. **437**, 173 (1999)
[71] M. Li, W. Hebenstreit and U. Diebold, Phys. Rev. B **61**, 4926 (2000)
[72] G. Charlton, P.B. Howes, C.L. Nicklin, P. Staedman, J.S.G. Taylor, C.A. Muryn, S.P. Harte, J. Mercer, R. McGrath, T.S. Turne and G. Thornton, Phys. Rev. Lett. **78**, 495 (1997)
[73] U. Diebold, J.F. Anderson, K.O. Ng and D. Vanderbilt, Phys. Rev. Lett. **77**, 1322 (1996)
[74] V.E. Heinrich, P.A. Cox, *The Surface Science of Metal Oxides* (Cambridge University Press, Cambridge, 1994)
[75] U. Diebold, J. Lehman, T. Mahmoud, M. Kuhn, G. Leonardelli, W. Hebenstreit, M. Schmid and P. Varga, Surf. Sci. **411**, 137 (1998)
[76] U. Diebold, Surf. Sci. Rep. **48**, 53 (2003)
[77] L. Zhang, R. Persaud and T.E. Madey, Phys. Rev. B **56**, 10549 (1997)
[78] S.C. Parker, A.W. Grant, V.A. Bondzie and C.T. Campbell, Surf. Sci. **441**, 35 (1998)
[79] X. Lai, T.P.S. Clair, M. Valden and D.W. Goodman, Prog. Surf. Sci. **59**, 25 (1998)
[80] F. Cosandey and T.E. Madey, Surf. Rev. Lett. **8**, 73 (2001)
[81] R. Schaub, P.Thostrup, N. Lopez, E. Lægsgaard, I. Stensgaard, J.K. Nørskov and F. Besenbacher, Phys. Rev. Lett. **87**, 266104 (2001)
[82] N. Lopez and J.K. Nørskov, Surf. Sci. **515**, 175 (2002)
[83] J. Carrey, J.L. Maurice, F. Petroff and A. Vaurès, Phys. Rev. Lett **86**, 4600 (2001)
[84] H. Häkkinen and U. Landman, Phys. Rev. B **62**, R2287 (2000)

Acknowledgements

At the end of my PhD thesis work, I want to acknowledge everyone who shared the work during these years with me.

In particular, I want to thank my supervisor Prof. Giovanni Comelli, who always trusted in me and was always present for scientific and technical discussions. I was also lucky to find in him a very humane person and this makes it easier and much more pleasant to work so many hours. He is not only a boss; he is also someone you can rely on. Then I want to mention Dr. Friedrich Esch. Friedrich and I have formed a "tested" STM team for several years; we learnt how to merge our personal attitudes, thus taking the maximum advantage for the group, and we learnt how to reciprocally tolerate our defects! He is a very good scientist and he is impressive in his ability to find very clever solutions for every kind of experimental problem. This constantly gave me the possibility of learning new tricks of this job.

I don't want to forget Prof. Renzo Rosei, the "head" of surface science in Trieste and the creator of this research group. He is a mine of scientific knowledge and he is always ready to answer any question. It is a wonderful advantage to have the opportunity to talk to him. Moreover, he is an incredibly communicative person and it is a pleasure listening to his descriptions of our work to people who don't know anything about this world.

Finally I want to thank all the undergraduate students who worked with me during these years, Stefano Marchini, Martina Corso and, even though only for a short time, Alessio Spessot. I hope I have been able to teach them the basics of this work and transmit most of my experience. I wish them all a very bright career and I know that they are already on this way!

I remember with delight and a little bit of nostalgia the period I spent in Århus. I feel very grateful to Prof. Flemming Besenbacher, who gave me the possibility of joining his research group. I could see how an excellent STM group works and I hope to have "stolen" something from their skill. I thank all the Århus staff, in particular the TiO_2 *subgroup, Dr. Renald Schaub and especially Dr. Erik Wahlström, who spent all the time with me in the lab, teaching me something completely new with a lot of patience and willingness.*

Concerning everyday life here in Trieste, I want to mention all the TASC people and in particular the technicians Stefano, Vanja and Sandro. Not only they were always very kind to help me in solving problems, but they also became friends and always made me relax at least at lunchtime!

I finally thank everyone who is close to me for the human support.